5/31/74

FERMILAB PROPOSAL No. 310

Scientific Spokesman:

D. Cline
Department of Physics
University of Wisconsin
Madison, Wisconsin 53706

FTS/Comm: 608 262-5878

Further Study of High Energy Neutrino Interactions at NAL

A. Benvenuti, D. Cline, A. Entenberg, W. T. Ford, R. Imlay
T. Y. Ling, A. K. Mann, F. Messing, D. D. Reeder, C. Rubbia,
R. Stefanski, L. Sulak, P. Wanderer and H. H. Williams

Harvard-Pennsylvania-Wisconsin-FERMILAB

A. PHYSICS GOALS

(a) INTRODUCTION

As a result of recent neutrino experiments and related technological progress in the past few years, it is possible to formulate a proposal for a neutrino detector to be used at NAL, which we believe will be capable of exploring the richness of that field better than present detectors. The complexity of high energy inelastic neutrino events - with and without final state muons - demands increased detector sophistication to unravel the full content of each event. This is particularly true of neutrino events at the highest energies, the highest four-vector momentum transfers, Q^2, and the highest inelasticity, $E_H = E_\nu - E_\mu$. We discuss in this proposal a plan that will allow continuous extrapolation of detector sophistication from the present detector to one of significantly improved capability with respect to both the quality and quantity of information obtained from neutrino interactions.

There are three components, in general, of a high energy neutrino-induced event: muonic, hadronic and electromagnetic. (There may also be additional neutrinos in the final state.) For each event it is necessary in the measurement process to separate these components and determine their salient properties.

The muonic component has the clearest signature and has received much attention in recent experiment. With the discovery of muonless events and the emphasis on events with large $y = E_H/E_\nu$, however, it is necessary to refine and extend the muon detection efficiency, especially for muons of low momentum emitted at the

largest angles. Typically, muon detection efficiencies for incident neutrinos have been 85% or less. We think it is necessary to obtain an efficiency in excess of 95% for much of the useful mass of the next target-detector.

Existing detectors (other than bubble chambers) sample the total hadronic and electromagnetic energy in an event. They do not discriminate between the hadronic and electromagnetic components, nor do they measure the directions of flow (the momenta of the centroids) of these components. A successful detector should distinguish the electromagnetic cascade from the hadronic cascade, and measure the energy and direction of flow of each cascade. In this way, the conservation of energy and linear momentum can be applied to each event, including muonless events.

Using a target-detector, such as we describe below, of large mass, a large acceptance muon spectrometer, and the capability of separating the hadronic and electromagnetic cascades of an event, neutrino reactions can be explored in appreciably greater depth and with greater breadth than heretofore.

There are four more points to be made with respect to the next phase of neutrino physics at NAL, as we envision it. First, the use of a variety of neutrino and antineutrino beams is a powerful tool in providing additional redundancy of the measurements made even with the most sophisticated detector. Second, the present high accelerator energy and high proton beam intensity, make it possible to carry out certain neutrino experiments with good statistical significance in relatively short periods of time. In the

next phase of neutrino physics at NAL, a successful detector should have the flexibility to allow testing and preliminary dating-taking for other, possibly more difficult, more speculative neutrino experiments during the course of the less demanding experiments. The availability of large mass large area detector components of different capabilities that can easily be arranged and rearranged in different configurations is a necessary attribute of the next neutrino detector. They make possible efficient and successful transitions from one facet of an experiment to another. Third, such a detector makes possible future large scale redirection and development of the experimental effort, based on techniques and components already proved by experiment. Finally, an arsenal of neutrino beams and of flexible, multipurpose detector components that utilize advanced technology appears to us to be the most effective method of probing this essentially new region of physics with reasonable assurance that new and unsuspected phenomena will not be overlooked.

(b) INTERESTING PHENOMENA IN THE PRESENT DATA

All of the program outlines in this proposal follows directly from the neutrino data that have been acquired up to now. There are three aspects of those data that deserve special mention.

I. The neutrino- and antineutrino-induced deep inelastic interactions without muons, which have been observed at low energy ($\langle E_\nu \rangle \approx 3$ GeV) in the CERN Gargamelle experiment and at high energy ($\langle E_\nu \rangle \approx 40$ GeV) at NAL, appear to have special significance. They may perhaps be manifestation of an intimate relationship between

the weak and the electromagnetic interactions. But the form of this relationship, if it exists at all, is not clear. For example, the connection between the two forces may arise as conjectured in the Weinberg-Salem gauge model, in which neutral weak currents make a natural appearance, and the V-A character of the weak interaction is preserved in neutral weak current processes. Another possibility is that the coupling leading to the effective neutral weak current may not be V-A, but rather pure V or pure A, with the result that the neutral weak processes would be parity conserving, as are electromagnetic processes. These possibilities are summarized with the data in Fig. 1. Other explanations are also possible.

It is clear that, whatever the ultimate explanation, continued study of neutrino- and antineutrino-induced deep inelastic events without final state muons has the potentiality of bringing us a deeper understanding of two of the fundamental forces in nature. To make further progess in that direction requires experiments that can uncover the matrix element of the deep inelastic muonless interaction. This is more difficult for muonless events than for events with muons, because the only final state observables in the muonless case are those of the resultant hadronic-electromagnetic cascade.

Nevertheless, the hadronic-electromagnetic cascade can be studied, we believe, in sufficient detail to separate the two components, and to make direct comparisons of salient distributions in neutral and charged processes. This is one of the primary future goals of our experiment. We describe in a later section the means for accomplishing it.

II. A second particularly interesting aspect of the present data lies in a possible anomaly in deep inelastic antineutrino scattering, which has recently been discussed by us at several conferences. This result is suggested by the measured distributions in the scaling variables x, y and v obtained from the reactions $\nu_\mu(\bar{\nu}_\mu)$ + nucleon → $\mu^-(\mu^+)$ + hadrons at high energy. The y-distribution for antineutrinos with $E_{\bar{\nu}} < 30$ GeV is consistent with the simplest expected form, $dn/dy \sim (1 - y)^2$, but the corresponding distribution for the energy region $30 < E_\nu < 180$ GeV departs severely from that form as shown in Fig. 2. If this discrepancy is genuine, it is indicative of a significant effective deviation from scale invariance or charge symmetry or both.

Again, whatever the ultimate explanation of these events, they emphasize the importance of carefully exploring deep inelastic processes at very large values of y, and at very large values of x as well. This is another primary goal of our experiment.

To accomplish that goal requires a much superior detection efficiency for wide-angle, low-energy muons from deep inelastic neutrino processes than exists now. A detection efficiency that falls rapidly with increasing y, in conjunction with even a good resolution function $\Delta y/y$, seriously limits the sensitivity and credibility of any search for structure in the y-distribution. Accordingly, we have designed a wide-angle muon magnetic spectrometer, utilizing large area drift chambers, to provide a very high muon detection efficiency for events originating in a large fraction of the total target-detctor mass. Details of the design are discussed below.

III. It is also possible to search directly in an exclusive fashion for new phenomena that lead to more than one muon in the final state. We have so far observed events with two muons at the level of a few tenths of a percent with appreciable energy in the hadronic-electromagnetic components. One such event is shown in Fig. 3. It is necessary to search for and study more of these events, especially over a wide range of muon energies, which will be facilitated by the new apparatus.

(c) PHYSICS GOALS OF THE EXPERIMENT

The experimental detector proposal here is specifically designed to study two high energy neutrino reactions which were not directly mentioned in the proposal for experiment E1A. These reactions are

$$\nu_\mu + N \rightarrow \nu_\mu + X \tag{1}$$

$$\bar{\nu}_\mu + N \rightarrow \bar{\nu}_\mu + X \tag{2}$$

and

$$\nu_\mu + N \rightarrow \mu^- + X \text{ near } y \sim 1 \tag{3}$$

$$\bar{\nu}_\mu + N \rightarrow \mu^+ + X \text{ near } y \sim 1 \tag{4}$$

The detector will also be compatible with the remaining approved experiments for E1A such as the measurement of the cross section for the process

$$\nu_\mu + Z \rightarrow \mu^+\mu^-\nu_\mu Z, \tag{5}$$

and the search for W production up to large masses and other non-local effects etc. Even though the detector is optimized to study

reactions 1 through 5 other neutrino reactions will be observable and can be studied.

I. Detailed Study of the Muonless Channel

The observation of muonless events at CERN and NAL has led to some optimism concerning the possible unification of weak and electromagnetic interactions, provided these muonless events are due to neutral weak currents. However, other possible interpretations of the muonless events exist. For example, Jouvet has suggested that the electromagnetic interaction of the neutrino might be large enough to explain the effect. Furthermore, the production of new particles could be partially responsible for the muonless events. New penetrating particles accompanying the neutrino beam could also be a source of this phenomena. Clearly a detailed study of the muonless events is required to separate these possibilities. In this study it is essential that the backgrounds that arise from charged current events be reduced to a very low level.

If the muonless events are due to neutral currents then it is clearly important to study Bjorken x and y distributions in order to establish the matrix element for these processes and to test scaling, in short, to carry out the same study that is underway for the charged current channel at NAL. We note that the absence of $\Delta S = 1$ neutral currents implies a breakdown in the traditional weak interaction universality for neutral currents. It may also be that the neutral currents have other significant differences from the charged currents which could only be revealed by a detailed study of the distribution functions.

The experimental study of neutral currents is made difficult because of the impossibility of measuring the outgoing neutrino angle and the practical difficulty of measuring the outgoing neutrinos energy. A different approach to the problem is required. It is necessary to concentrate on the measurable component of the neutral current collision, the hadronic energy E_H and the direction of flight of the hadrons, ϕ_H and θ_H as shown in Fig. 4. This requires that the direction of hadronic energy flow be measurable in the detector.

The measurement of θ_H and E_H allows us to use a new scaling variable u

$$u \simeq \frac{E_H}{2m_p}\theta_H^2 = x(1 - y)$$

and to express the distribution functions in terms of this scaling function. For example, the most general distribution function that obeys scaling and the (V, A) interactions of neutral current is given by

$$\frac{d^2\sigma^{\nu}}{dxdy} = f_L + (1 - y)^2 f_R + 2(1 - y)f_s$$

$$\frac{d\sigma^{\bar{\nu}}}{dxdy} = f_R + (1 - y)^2 f_L + 2(1 - y)f_s$$

where the f's are functions of x only. The distribution in u is given as

$$\frac{1}{N}\frac{dN^{\nu}}{du} = \frac{\int_u^1 \frac{1}{x}[f_L + (u/x)^2 f_R + (2u/x)f_s]dx}{\int_0^1 [f_L + \frac{1}{3}f_R + f_s]dx}$$

$$\frac{1}{N}\frac{dN^{\bar{\nu}}}{du} = \frac{\int_u^1 \frac{1}{x}[f_L + (u/x)^2 f_R + (2u/x)f_s]dx}{\int_0^1 [f_R + \frac{1}{3}f_L + f_s]dx}$$

The u distributions for the simple case of the parton model ($f_R = f_s = 0$, $f_L = F_2(x)$) and a broad band neutrino-antineutrino beam are shown in Figs. 5a and b and compared in 6. We can also derive the corresponding θ_H distributions as shown in Figs. 7 and 8. We note that the θ_H distributions alone, carry a great deal of information and that the hadrons frequently emerge at large angles making the measurement of θ_H easier. We also note that the E_H distribution can be directly related to the y distribution.

The study of the muonless events proposed here requires the use of the sign selected beam or double horn beam in order to separate ν_μ and $\bar{\nu}_\mu$ interactions.

The distribution in x can be obtained through the distribution in u (by the measurement of E_H, θ_H), and the y distribution is obtained through the measurement of E_H and knowledge of the neutrino spectrum. Also an indirect study of locality in the interaction can be carried out that would provide information about the W° mass. In other words, substantially the same program can be carried out for the neutral currents as for the charged currents.

The measurement of θ_H requires measurement of the energy flow direction. In order to carry this out it is necessary to track the hadronic-electromagnetic shower through the calorimeter. Sensible measurements of the hadronic direction can only be carried out if the energy density is tracked and not the particle number density since the abundant low energy particles in the shower smear

out the directional information. In order to measure the energy flow in our detector it is necessary and convenient to track the electromagnetic energy flow since the hadronic component of the shower is constantly feeding into the electromagnetic components. This tracking requires a separation and sampling of the electromagnetic and hadronic components of the shower at different distances from the vertex of the event. This is accomplished by using a three element system, liquid scintillation calorimeter cell, wide gap spark chambers and a Pb plate array that serves as a hodoscope and calorimeter simultaneously. The basic cell arrangement and a schematic neutral current event are shown in Fig. 9. In order to calibrate the energy flow device, the charged current events are used with θ_H predicted from the measurement of P_μ, θ_μ and E_H (or E_ν for a dichromatic beam) as shown in Fig. 10.

II. Threshold Effects at High y

An extremely sensitive place to search for scaling breakdown is in the y-distribution at high-y. The neutrino energy range of 20-200 GeV must be covered in one experiment if a complete understanding is to be achieved. Furthermore, new particle production could cause threshold effects in this range that distort the x and y distributions as shown schematically in Fig. 11. Finally, the cross section for high-y events in the antineutrino case will be very small and, therefore, a large aperture device is required to obtain enough events to make a precision sweep in neutrino energy.

The kinematic boundaries for θ_μ and p_μ are shown in Fig. 12 for various neutrino energies. We note that at large angles a maximum muon momentum occurs which is approximately independent of the

neutrino energy. Large θ_μ implies large y as can be observed from the simple formula

$$\theta_\mu^2 = \frac{2v}{[1 - y]}(m_p/E_\nu)$$

In Fig. 13 is shown the expected mean muon momentum as a function of angles. At the larger angles a mean momentum of a few GeV is expected and this in turn determines the nature of the magnetic spectrometer required to study these events.

III. Unavoidable Dividend Experiments

Other neutrino events may be recognizable in this detector. Two such processes are

$$\nu_e + N \rightarrow e + X$$

and

$$\nu_\mu + e^- \rightarrow \nu_\mu + e^-$$

The event signature for these processes is schematically illustrated in Figs. 14 and 15, respectively.

A direct and unavoidable dividend from an apparatus designed to accomplish the goals described above is the capability of studying events induced by ν_e and $\bar{\nu}_e$. This follows from the requirements that the electromagnetic and hadronic components of a neutrino-induced event be separable, and that the muonic component be detected with very high efficiency. The measurements of the deep inelastic structure functions and of $\sigma_{tot}^{\nu_e}$ and $\sigma_{tot}^{\bar{\nu}_e}$ vs. E_{ν_e} - even when carried out with an incident beam intensity of (2-4) $\times 10^{-2}$ of the $\nu_\mu(\nu_\mu)$ intensity - will allow an early exploration of $\nu_e(\bar{\nu}_e)$ + nucleon interactions at high energies, and another approach to the

e-μ universality problem through the direct comparison of ν_e and ν_μ interactions with hadrons. An enriched ν_e beam is discussed in Appendix 4.

An important goal in the study of muonless event is a definitive search for neutral current processes in pure leptonic reactions such as $\nu_\mu + e^- \rightarrow \nu_\mu + e^-$, at the lowest level predicted by the Weinberg-Salem gauge model, and suggested by the three possible events of that type in the CERN-Gargamelle experiment. This is a very difficult experiment since the cross section is lower than that for neutrino-neucleon scattering in the ratio m_e/m_p, and only the final state electron is observable. However, the thin-plate lead and liquid scintillator ionization calorimeter modules that are necessary to study the energy and momentum flow in the deep inelastic muonless events will also serve as an identifier of single chambers to specify the angle, have the promise at least of providing a relatively unique signature for $\nu_\mu + e^- \rightarrow \nu_\mu + e^-$, and sufficient rate to make the process detectable.

(d) OUTLINE OF THE NEW DETECTOR

To realize the neutrino physics program described above, we propose the experimental apparatus shown in Fig. 16. It consists of four major components: (i) a large acceptance muon momentum spectrometer with large area, high resolution drift chambers; (ii) an iron plate calorimeter-absorber to provide good containment of hadronic cascades; (iii) a multi-purpose ionization calorimeter comprised of modular elements of (a) pure liquid scintillator and (b) lead plate-liquid scintillator, in combination with wide gap

optical spark chambers interspersed as indicated; and (iv) a variety of large area liquid scintillator counters that serve as anticounters, trigger counters and very large angle muon detectors (muon-catchers).

(i) The large acceptance muon momentum spectrometer

The basis for design of the new magnet system is the common characteristic of the kinematic upper limits of the p_μ-θ_μ plots for various values of E_ν, assuming scale invariance as an approximate guide. These are shown for E_ν between 35 and 200 GeV in Fig. 13, where it is seen that for $\theta_\mu \gtrsim 300$ mrad, $p_\mu \lesssim 20$ GeV for any value of E_ν. Thus for $\theta_\mu \gtrsim 300$ mrad, it is possible to make a reasonably accurate measurement of p_μ and of the sign of the muon charge with a relatively short magnetic field region. Above $\theta_\mu \approx 500$ mrad, ranging out of the muons begins to be significant, which in turn also suggests short regions of iron magnet with chambers between to determine the muon momentum be a range measurement. As θ_μ grows smaller, a longer length of magnet is required to measure the larger p_μ, which accounts for the shape of the muon spectrometer in Fig. 16.

The present muon spectrometer magnets are each 4 ft. thick and 12 ft. in diameter. We propose to add an additional section 4 ft. long and 20 ft. in diameter, and two sections each 2 ft. thick with 30 ft. diameters as shown in Fig. 16.

The entire magnetic spectrometer will be equipped with large area drift chambers. A detailed description of our development work on and operating experience with large area (12' × 12') drift chambers is given in Appendix 1, which also includes the detailed

arrangement of drift chambers in the new apparatus.

(ii) The iron-plate ionization calorimeter-absorber

This component of the apparatus is intended to provide good containment of the hadronic-electromagnetic cascades that originate further upstream in the target-detector. The iron plates provide a convenient, compact way of introducing about 6 nuclear absorption lengths at the end of the target detector. In this calorimeter-absorber the residual energy of a cascade can be measured with acceptable accuracy, as several recent studies of iron-plate calorimeters have shown. To save space, and thereby improve the muon detection efficiency of the magnetic spectrometer, we have considered the possibility of inserting the calorimeter-absorber in the spectrometer, as shown in Fig. 16. An alternative design, which might be easier to implement, simply moves the iron calorimeter-absorber in front of the spectrometer, at a small loss in acceptance as shown in a later section of this proposal.

(iii) Multipurpose lead-plate, liquid scintillator ionization calorimeter (target-detector).

The target-detector of the new apparatus is made up of three component parts. (1) Calorimeter modules of thin lead plates with liquid scintillator between them to form a unit containing 14 radiation lengths (L_{rad}) and 0.8 collision lengths (L_{coll}), of total mass about 8 metric tons. The lead plates are coated with teflon to provide total internal reflection and thereby good light collection. This technique was developed by us and has been used successfully by us and others in calorimeter construction. (2) Calorimeter modules of pure liquid scintillator identical to those used

previously in E1A. (3) Wide gap optical spark chambers identical to those now in E1A.

The basic idea behind the lead plates, as opposed to iron plates or pure liquid scintillator, is illustrated in Fig. 17, which compares the energy deposition curves for electrons and pions in a lead plate calorimeter. It is clear from Fig. 17 that the hadronic and electromagnetic can to a large extent be separated in such a calorimeter. Because the electromagnetic component is essentially terminated in such a short length of material, we have referred to the lead-plate modules in Fig. 16 as γ-catchers. A more detailed discussion of the energy flow direction measurement is given in Appendix 2.

With "building blocks" of the three types initially arranged as in Fig. 16 the target-detector has the capability necessary for the program described earlier. It is important that the components of the target-detector be easily moved and replaced. We envision various, continuous modifications of the target-detector, one of which might be, for example, a configuration without any pure liquid scintillator modules in which there would be a 350 metric ton target-detector of lead and spark chambers. With that arrangement, the rates for trilepton production and for inelastic events with large E_ν and Q^2 would be enhanced (see Table IV below).

(iv) <u>The large area, relatively thin liquid scintillator counters</u>

The large area, relatively thin liquid sintillator counters that have been used in E1A so far have proved valuable as anti-counters and wide-angle muon counters. We propose to extend their

use as wide-angle muon identifiers (muon-catchers) as indicated in In Fig. 16. Note that this is intended to supplement the wide-angle magnetic spectrometer where the sign of the charge and the momentum of the muon are measured. The purpose of the muon-catchers is simply to record the presence of a wide-angle muon so that the total detection efficiency over most of the target-detector is raised above 95%.

(e) EVENT RATES

There are shown in Tables I-IV the event rates calculated for the neutrino processes discussed above. These rates are based on the rates for inelastic scattering observed in E1A during the past year, appropriately scaled for other interactions. Other assumptions used in the calculations are indicated. Table 1 gives the total event rates for a variety of reactions using different incident neutrino and antineutrino beams for 10^{17} protons on target. Table II gives the event rates for various neutrino energy regions for a number of incident beams. Table III gives the event rates as functions of Q^2 and E_H for two different beams. Table IV gives event rates for the 350 metric ton target-detector.

B. MUON DETECTION EFFICIENCIES AND EXPERIMENTAL RESOLUTION

The main goals of the physics place two general constraints on the design of the revised detector.

1. The muonless event sample should be clean and the parameters E_H and θ_H measured with the best resolution that can be practically achieved over a large target volume.

2. The sign of the charge, momentum and angle of very large angle muons must be measured.

In order to reduce the background in the neutral current sample arising from charged current events a large solid angle muon spectrometer is required and this same spectrometer can be used to study wide angle muons. A large spectrometer is needed to keep the good aspect ratio obtained in the present detector for high energy neutrinos, as the length of the target calorimeter is increased. In addition it is required for the study of neutrino and antineutrino interactions in the H_2 target, since the calorimeter must directly follow the H_2 target keeping the muon spectrometer at a large distance.

The measurement of the energy flow direction of the hadronic shower is made possible by the localization of the energy density of the electromagnetic component in the shower in a Pb plate array. It is not sufficient to measure the directions of the particles in the shower since the information content is greatly reduced by the presence of many low energy particles especially electrons and positrons. We have carried out Monte Carlo calculations for the propagation of the hadronic shower and find that the electromagnetic component does indeed carry adequate information from which to obtain θ_H provided the energy flow of the electromagnetic shower is measured. These calculations indicate that the direction of electromagnetic energy flow tracks that of the parent hadrons within an uncertainty in the transverse momentum of the parent hadrons of approximately 0.3 GeV/c. This results from the limited transverse

momentum of the secondaries in the initial hadronic shower and the limited transverse momentum change for the subsequent hadronic or electromagnetic cascades. We assume that the particle distributions follow the same multiplicity law at a given E_H as those for hadronic collision processes. Measurements of the mean charged multiplicity as a function of E_H made from E1A data that is in hand, support this assumption and are shown in Fig. 18. Additional information on θ_H can also be obtained by meausring the mean directions of the charged hadrons. This is accomplished in spark chambers that are placed directly behind the gamma catchers.

I. Efficiency and the Distortion of Distributions

In order to measure a sensitive rapidly changing distribution such as dN/dy for antineutrinos, care must be taken that the detector does not cause a serious distortion. Such a distortion can arise either from systematic shifts in the variable due to calibration problems or due to smearing from bad resolution. The problem is compounded if a rapid variation is introduced due to a rapidly falling efficiency function for the particular variable. As a rough figure of merit we may divide the efficiency ε_M by the resolution function $\delta M/M$ for a measured variable M. In the case that this ratio decreases rapidly as M is changed, serious distortions can be induced into the distribution function dN/dM. Ideally, this ratio would be constant or perhaps increase in a region of lower efficiency. This argument illustrates the importance of maintaining high detection efficiency out to large y if the shape of dN/dy is to be measured and compared at different neutrino energies. How-

ever, it is essential to retain good resolution at high y in order to study the x or v distribution in this region.

At large y and large angle the muon momentum is generally below 10 GeV as can be seen from Fig. 13. In this region a significant fraction of the energy of the muon will be lost by ionization in the calorimeter and therefore can be well measured. The remaining muon momentum is low and therefore a thin magnetic spectrometer is adequate to determine the sign of the charge and to measure this remnant momentum. A resolution of the magnet of $\delta P_\mu/P_\mu \sim 0.2$. With half or more of the energy lost by ionization gives an overall resolution of $\delta P_\mu/P_\mu \lesssim 0.1$, which is similar to the resolution of the present long E1A magnet.

II. Efficiency of the Muon Detector

The results of a calculation of the efficiency for muon detection in the new detector as a function of E_ν, x and y are reported in Figs. 19-26. These calculations are made for various target lengths and two muon detectors as shown in Fig. 19. Also reported in Fig. 27 is the efficiency for the H_2 target. We note that in most cases the efficiency is excellent even at large y. The x and y efficiencies for the H_2 target are sufficiently good to make the study of x and y distributions on H_2 feasible.

In Fig. 20 we compare the angular distribution of muons from deep inelastic neutrino scattering with the acceptance provided by the detector immediately downstream of the first four-foot-thick magnet module. The acceptance for events within the downstream 24

feet of target is $\sim$ unity over the angle range containing 95% of the events, and is $\sim$ 99% over all the full distribution. In this limit the main source of missed muons is the ranging out of those with very low energy. Most of these are also at large angles; we estimate that they will have sufficient range to be separated from the hadrons whenever p_μ is greater than $\sim$1.5 GeV. Integrating over the energy spectrum we find ε_μ = .98 for neutrinos from the quad triplet or dichromatic beam, and .94 from the double horn beam. (Antineutrinos give a higher efficiency, to the extent that they obey $d\sigma/dy \propto (1 - y)^2$ at lower energies.)

To maintain high muon veto efficiency over the full length of the target-detector, additional liquid-scintillator muon counters are placed along the sides, top and bottom of the calorimeter as shown in Fig. 16.

III. Measurement Error in u for the Muonless Channel

We can express the error in u in terms of error in θ_H and E_H as

$$(\delta u/u)^2 = 4(\delta\theta_H/\theta_H)^2 + (\delta E_H/E_H)^2$$

The value of x can also be obtained for the muonless channel using the formula $x = u/(1 - y)$ for a dichromatic beam. The error $(\delta\theta_H/\theta_H)$ will be determined by the intrinsic fluctuation in the angular distribution of the electromagnetic component of the shower and the granularity of the hodoscope used to measure the energy density in each γ catcher. Our best estimate at present is that the center of the energy flow can be located to a few cm in one

direction by measuring the relative pulse heights at the two ends of the counter (see Appendix 2). We therefore expect $\delta\theta_H$ to be in the vicinity of 20 mr. An empirical calibration will be made with the charged current events.

Note that the resolution will improve with increasing θ_H so that at large θ_H $\delta\theta_H/\theta_H \sim 0.1$ and the error in E_H will become comparable to that for θ_H. We anticipate that $(\delta u/u) \sim 0.2$ can be obtained allowing useful measurements of the u distribution for muonless events.

IV. Errors in x at Large θ_μ

The resolution for x and y for the charged current events is given by

$$(\delta x/x)^2 = 4(\delta\theta_\mu/\theta_\mu)^2 + [2 - y]^2(\delta P_\mu/P_\mu)^2 + (1 - y)^2(\delta E_H/E_H)^2$$

and

$$(\delta y/y)^2 = (1 - y)^2[(\delta E_H/E_H)^2 + (\delta P_\mu/P_\mu)^2]$$

For events observed in the large angle spectrometer $y \sim 1$ and the measurement error in x and y becomes approximately independent of the hadron energy resolution. This facilitates the search for threshold effects at large y and for any x. Furthermore, at large θ_μ the error $(\delta\theta_\mu/\theta_\mu) << (\delta P_\mu/P_\mu)$ and thus

$$(\delta x/x)^2 \sim (\delta P_\mu/P_\mu)^2;$$

the muon momentum error sets the error in x. Note that at small angles the error in x comes almost equally from all three sources. By using the muon momentum measurements that include ionization we expect $(\delta P_\mu/P_\mu) \sim 0.1$ which is comparable to the error in muon

momentum obtained from the small angle spectrometer. This error is small enough to allow a detailed study of the x distribution at large y and to test scaling there.

TABLE I

PROCESSES	CROSS SECTION (CM^2)	TARGET MASS (Metric Tons)	EVENT RATE PER 10^{17} PROTONS					
			300 GEV 1 HORN	400 Gev 1 HORN	400 GeV 2 HORN	400 GeV QUAD TRIPLET (P_o=125)	400 GeV QUAD TRIPLET (P_o=200)	400 GeV DICHROM (P_o=200)
$\nu_\mu + N \to \mu^- +$ hadrons	$0.6 \times 10^{-38} E_\nu/N$	162	17,162	29,500	46,470	13,078	6,817	3,061
$\bar{\nu}_\mu + N \to \mu^+ +$ hadrons	$0.2 \times 10^{-38} E_{\bar{\nu}}/N$	Pb + Liq.	3,885	6,678	10,520	1,763	919	430
$\nu_\mu + N \to \nu_\mu +$ hadrons	$\sim 0.6 \times 10^{-39} E_\nu/N$	162	1,716	2,950	4,647	1,308	682	306
$\bar{\nu}_\mu + N \to \bar{\nu}_\mu +$ hadrons	$\sim 0.6 \times 10^{-39} E_{\bar{\nu}}/N$	Pb + Liq.	389	668	3,156	176	92	129
$\nu_\mu + e^- \to \nu_\mu + e^-$	$1.4 \times 10^{-42} E_\nu/e^-$	54	0.67	1.15	1.81	0.51	0.27	0.12
$\bar{\nu}_\mu + e^- \to \bar{\nu}_\mu + e^-$	$4.0 \times 10^{-42} E_{\bar{\nu}}/e^-$	Liq.	1.29	2.23	3.51	0.57	0.30	0.15
$\nu_\mu + Pb \to \nu_\mu + \mu^+ + \mu^- + Pb$	$5 \times 10^{-41} E_\nu/Pb$	108 Pb	0.46	0.79	1.24	0.35	0.18	0.08
$\nu_\mu + Pb \to \nu_e + e^+ + \mu^- + Pb$	$7 \times 10^{-41} E_\nu/Pb$		0.64	1.10	1.73	0.49	0.25	0.12
$\nu_\mu + Pb \to \nu_\mu + e^+ + e^- + Pb$	$2 \times 10^{-41} E_\nu/Pb$		0.2	0.4	0.6	0.14	0.07	0.03
$\nu_e + N \to e^- +$ hadrons	$0.6 \times 10^{-38} E_\nu/N$	162	172	295	465	131	68	31
$\bar{\nu}_e + N \to e^+ +$ hadrons	$0.2 \times 10^{-38} E_\nu/N$	Pb + Liq.	8.6	14.8	23.4	6.6	3.4	1.5
$\nu_e + e^- \to \nu_e + e^-$	$54. \times 10^{-42} E_\nu/e^-$	54 Liq.	0.03	0.05	0.08	0.02	0.01	0.005

1. Fiducial region in x, y is taken to be 2.8×2.8 m^2

2. Cross-sections for processes allowed only by neutral current are calculations based on Weinberg Model, $\sin^2 \theta_W = 0.5$

TABLE II

E_{PROTON}	BEAM	$\nu, \bar{\nu}$	EVENT RATE PER 10^{17} PROTONS PER NEUTRINO ENERGY BIN (GeV)					
			0-50	50-100	100-150	150-200	200-400	0-400
300	DOUBLE HORN	ν	16380	2125	927	188	--	19620
300	DOUBLE HORN	$\bar{\nu}$	4110	255	31	1	--	4400
400	DOUBLE HORN	ν	35900	8300	2700	1200	400	46500
400	DOUBLE HORN	$\bar{\nu}$	8780	1440	210	34	4	10470
400	QUAD TRIPLET (P_o=200)	ν	1770	2950	660	960	440	6780
400	QUAD TRIPLET (P_o=200)	$\bar{\nu}$	350	490	44	23	4	910
400	SIGN-SELECTED (P_o=200)	ν	780	1655	90	385	140	3550
400	SIGN-SELECTED (P_o=200)	$\bar{\nu}$	135	265	12.5	8.5	1.5	425
400	BARE TARGET	ν	2737	1897	681	361	171	5850
400	BARE TARGET	$\bar{\nu}$	923	278	39	6	--	1245

EVENT RATES FOR $\nu_\mu(\bar{\nu}_\mu) + N \rightarrow \mu^{\mp} +$ HADRONS

IN 162-TON TARGET

TABLE III

EVENT RATES VS. Q^2, E_H FOR NEUTRINOS EVENTS
PER 10^{17} 400-GeV PROTONS (162-TON TARGET)

VARIABLE RANGE	DOUBLE HORN	QUAD TRIPLET (P_o=200)
$0 < Q^2 < 20$ GeV^2	41770	4540
$20 < Q^2 < 50$	6000	1720
$50 < Q^2 < 100$	1140	658
$100 < Q^2 < 200$	170	222
$200 < Q^2 > 200$	10	18
$0 < E_H < 50$ GeV	41920	4620
$50 < E_H < 100$	3520	1380
$100 < E_H < 150$	860	500
$150 < E_H < 200$	150	230
$E_H > 200$	50	50
ALL Q^2, E_H	46500	6780

TABLE IV

PROCESSES	CROSS-SECTION (CM^2)	TARGET MASS (Metric Tons)	EVENT RATE PER 10^{17} PROTONS					
			300 GeV 1 HORN	400 GeV 1 HORN	400 GeV 2 HORN	400 GeV QUAD TRIPLET (P_o=125)	400 GeV QUAD TRIPLET (P_o=200)	400 GeV DICHROM (P_o=200)
$\nu_\mu + N \rightarrow \mu^- +$ hadrons	$0.6 \times 10^{-38} E_\nu/N$	350	37,078	63,500	100,398	28,255	14,728	6,615
$\bar{\nu}_\mu + N \rightarrow \mu^+ +$ hadrons	$0.2 \times 10^{-38} E_{\bar{\nu}}/N$		8,393	14,427	22,728	3,809	1,985	928
$\nu_\mu + N \rightarrow \nu_\mu +$ hadrons	$\sim 0.6 \times 10^{-39} E_\nu/N$	350	3,707	6,373	10,040	2,826	1,473	661
$\bar{\nu}_\mu + N \rightarrow \bar{\nu}_\mu +$ hadrons	$\sim 0.6 \times 10^{-39} E_{\bar{\nu}}/N$		840	1,443	6,819	380	199	279
$\nu_\mu + e^- \rightarrow \nu_\mu + e^-$	$1.4 \times 10^{-42} E_\nu/e^-$	350	4.34	7.45	11.73	3.30	1.75	0.75
$\bar{\nu}_\mu + e^- \rightarrow \bar{\nu}_\mu + e^-$	$4.0 \times 10^{-42} E_{\bar{\nu}}/e^-$		8.36	14.45	22.75	3.69	1.94	0.94
$\nu_\mu + Pb \rightarrow \nu_\mu + \mu^+ + \mu^- + Pb$	$5 \times 10^{-41} E_\nu/Pb$		1.49	2.56	4.02	1.13	.58	0.26
$\nu_\mu + Pb \rightarrow \nu_e + e^+ + \mu^- + Pb$	$7 \times 10^{-41} E_\nu/Pb$	350	2.07	3.56	5.61	1.59	.81	0.37
$\nu_\mu + Pb \rightarrow \nu_\mu + e^+ + e^- + Pb$	$2 \times 10^{-41} E_\nu/Pb$		0.58	1.0	1.68	0.45	0.22	0.10
$\nu_e + N \rightarrow e^- +$ hadrons	$0.6 \times 10^{-38} E_\nu/N$	350	372	637	1,005	283	147	62
$\bar{\nu}_e + N \rightarrow e^+ +$ hadrons	$0.2 \times 10^{-38} E_\nu/N$		18.6	32	50.5	14.3	7.3	3.2
$\nu_e + e^- \rightarrow \nu_e + e^-$	$5.4 \times 10^{-42} E_\nu/e^-$	350	.19	.32	.52	.13	.06	0.03

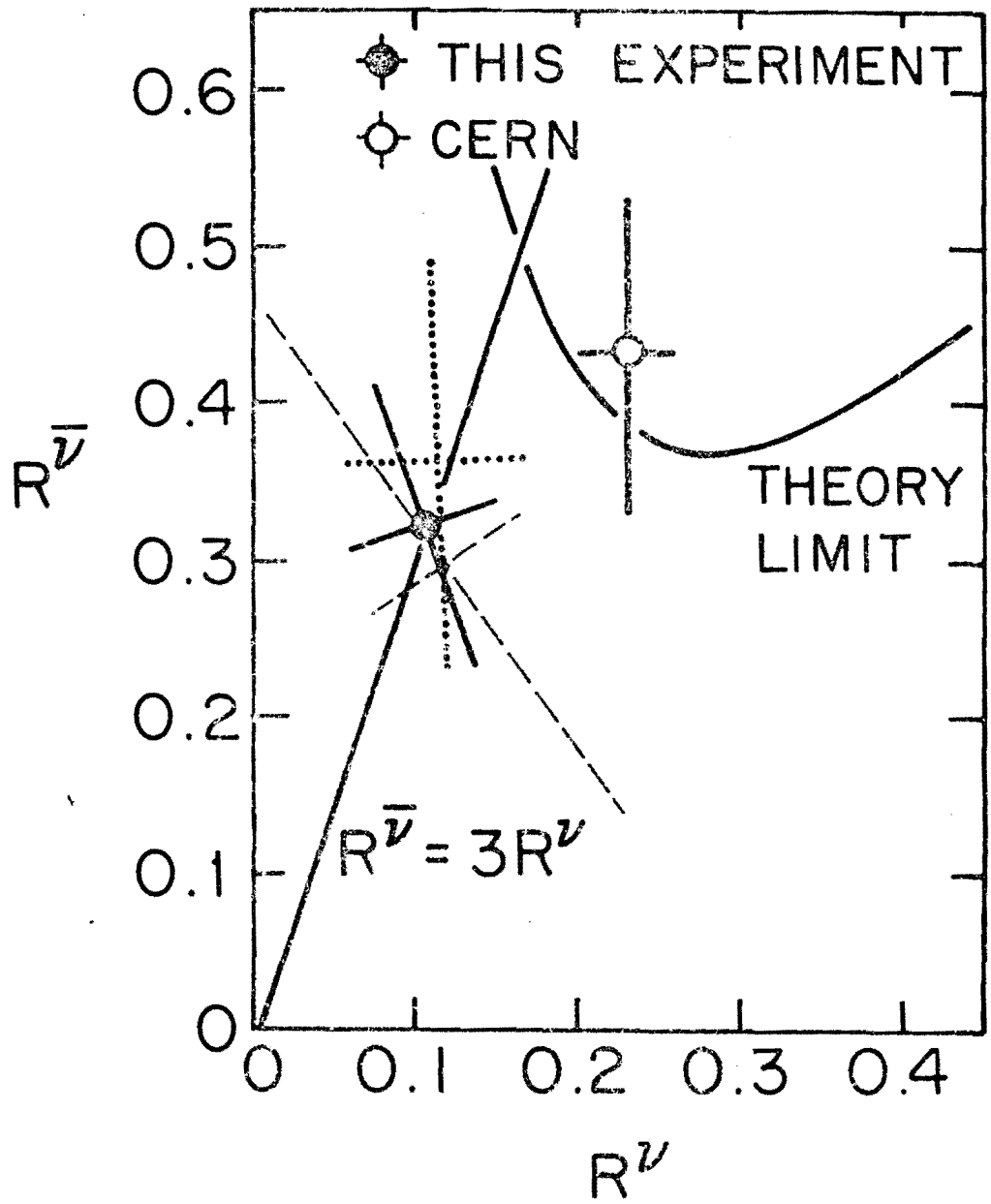
THIS EXPERIMENT
CERN
THEORY LIMIT
$R^{\bar{\nu}} = 3R^{\nu}$
$R^{\bar{\nu}}$
R^{ν}
0
0.1
0.2
0.3
0.4
0.5
0.6

FIG 1

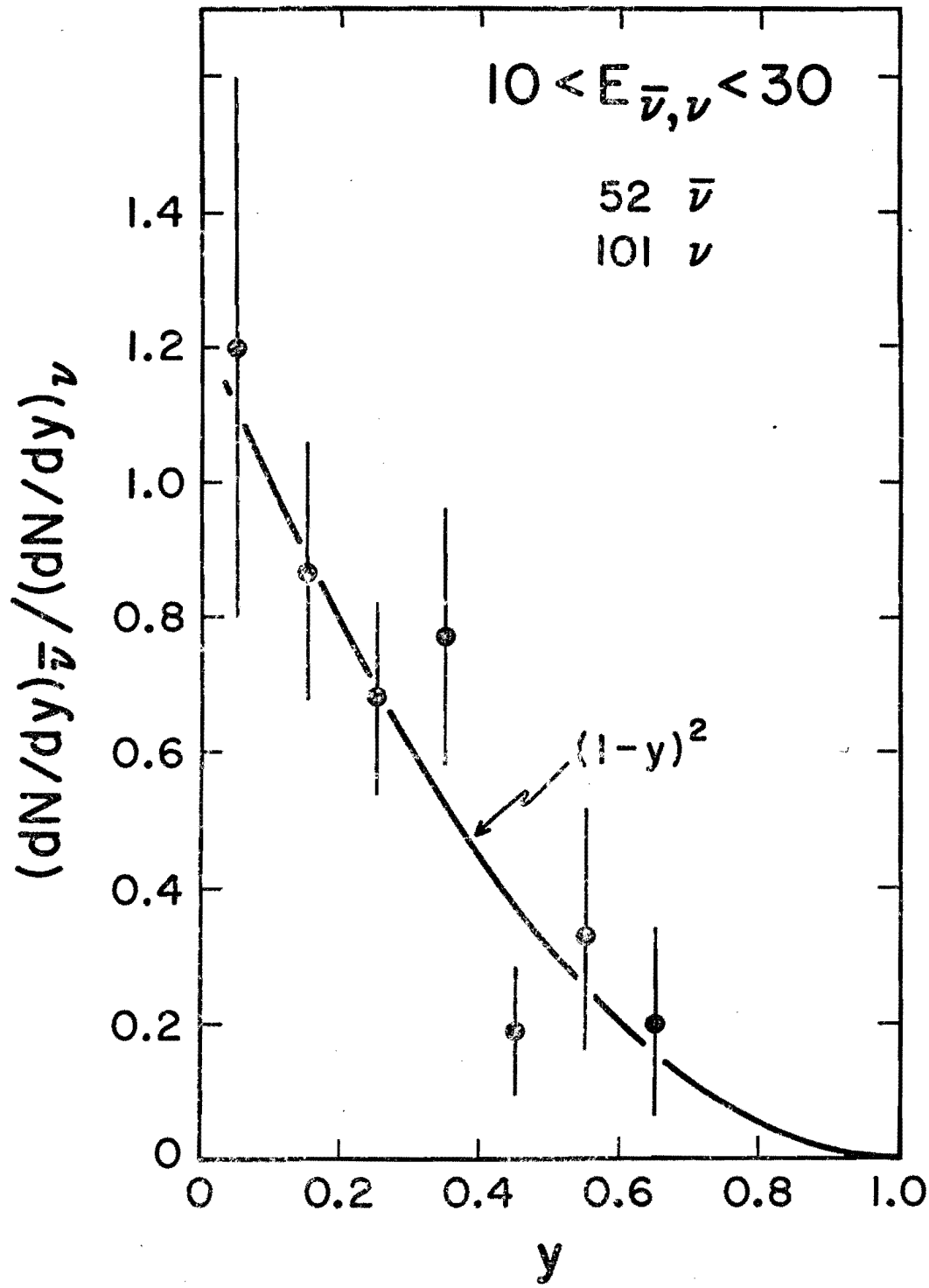
$10 < E_{\bar{\nu},\nu} < 30$
52 $\bar{\nu}$
101 ν
$(1-y)^2$
$(dN/dy)_{\bar{\nu}} / (dN/dy)_{\nu}$
y
0
0.2
0.4
0.6
0.8
1.0
1.2
1.4

Fig. 2a

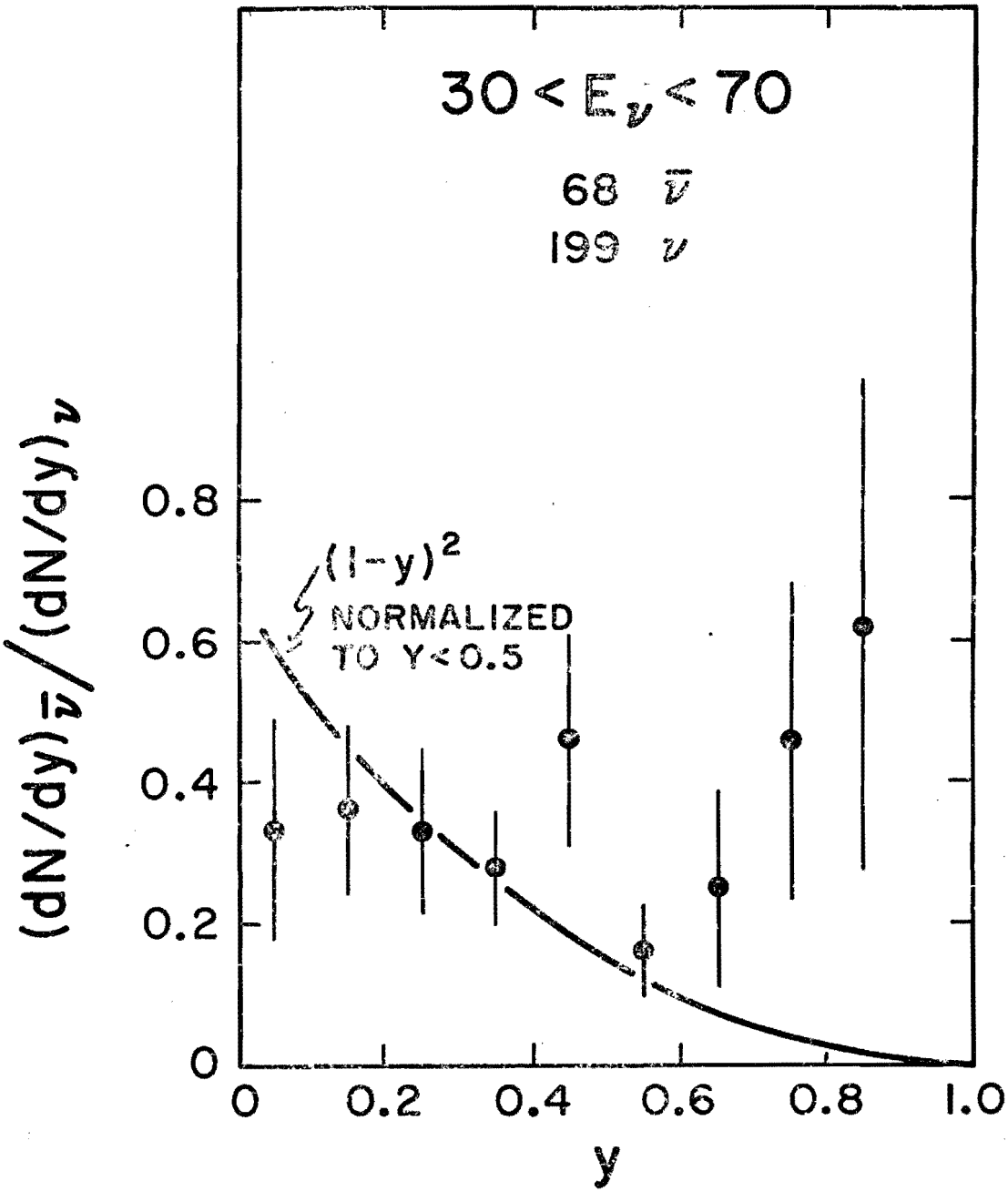
30 < E_ν < 70
68 ν̄
199 ν
(1-y)²
NORMALIZED
TO Y<0.5
(dN/dy)ν̄/(dN/dy)ν
0
0.2
0.4
0.6
0.8
1.0
y

Fig 2b

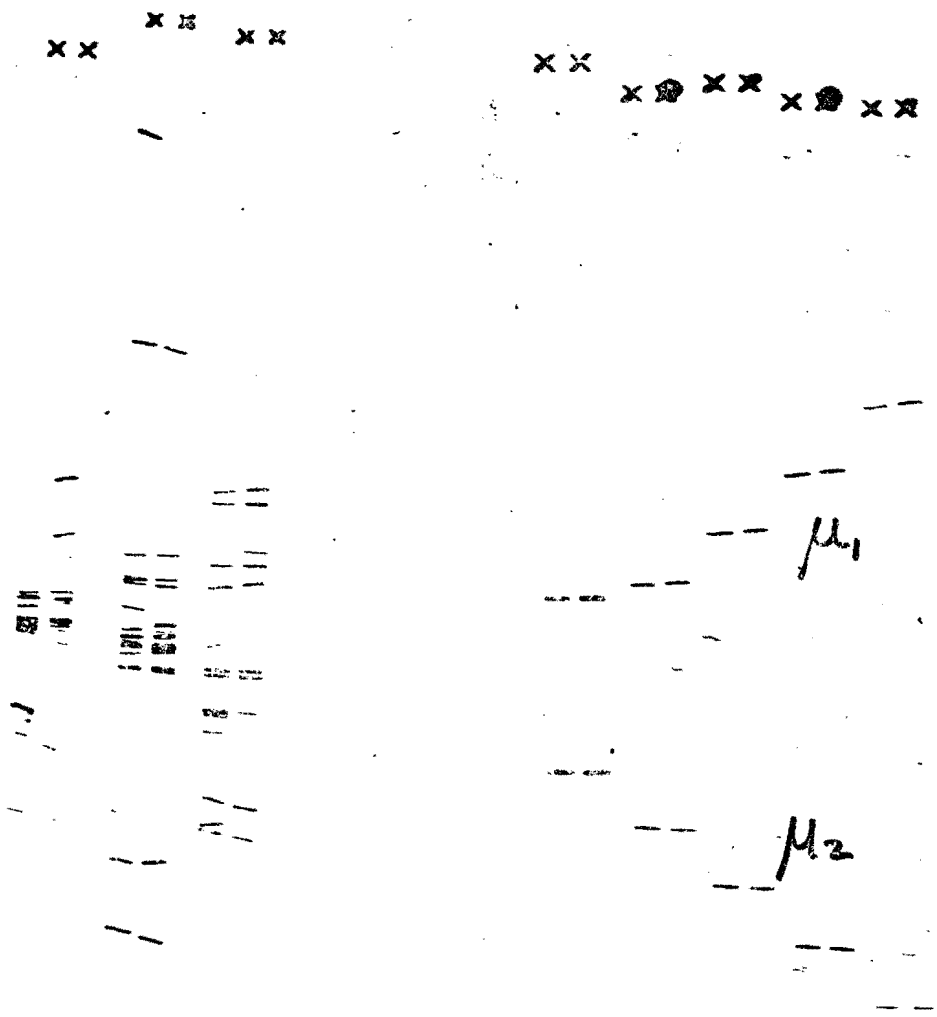

FIG 3

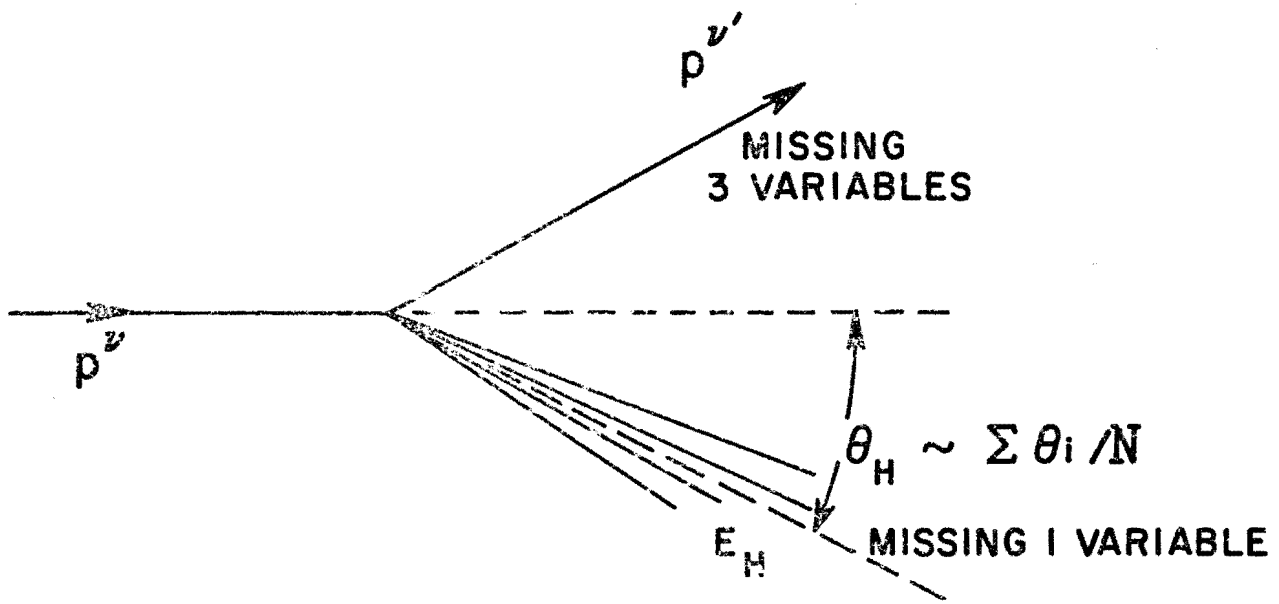

CASE I. HORN OR QUADTRIPLET BEAMS : - I CONSTRAINT ON FIT

CASE 2. DICHROMATIC BEAM WITH NARROW PEAKS : 0 CONSTRAINT
2 FOLD AMBIGUITY

FIG. 4

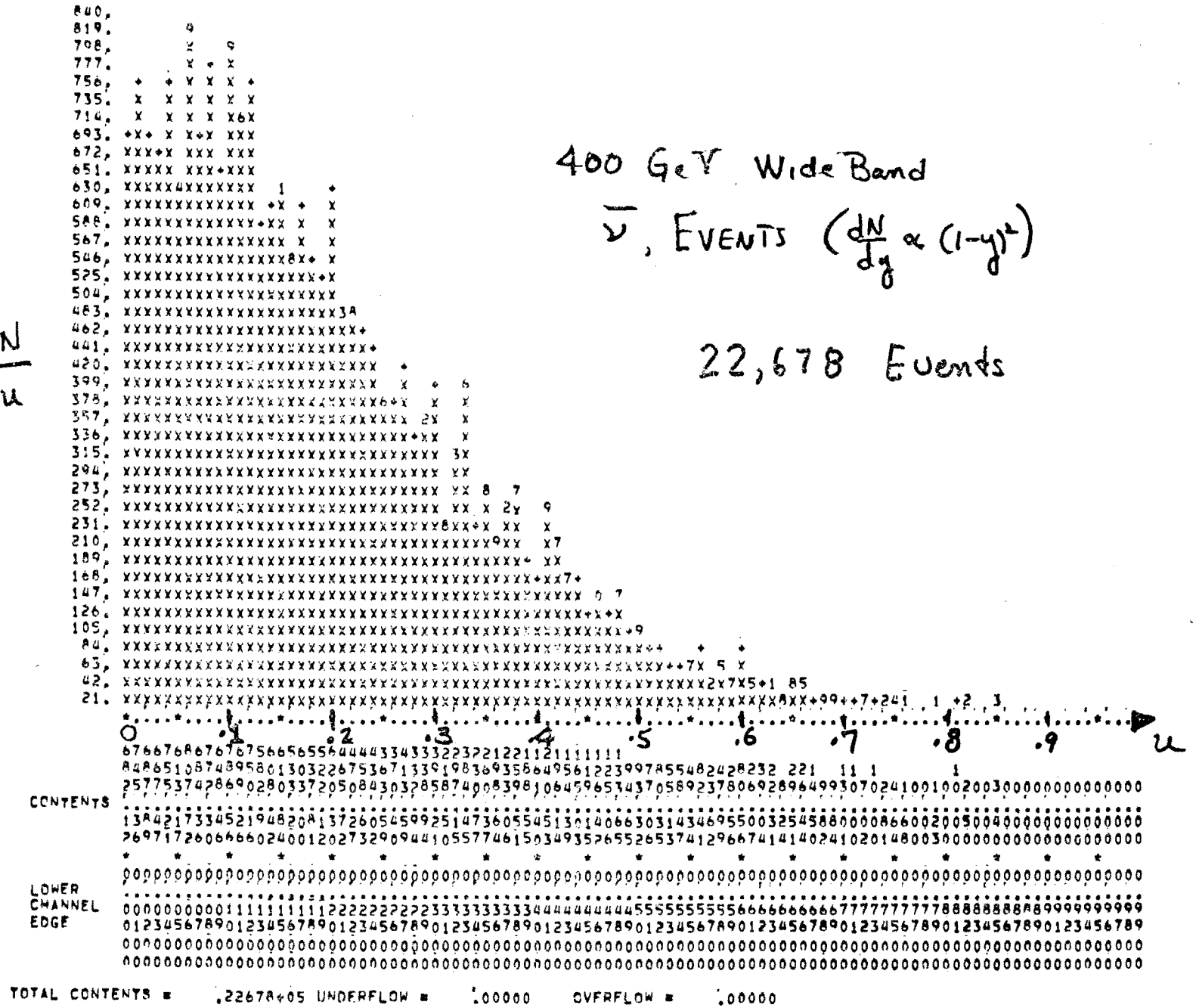
400 GeV Wide Band
$\bar{\nu}$, Events $\left(\frac{dN}{dy} \propto (1-y)^2\right)$
22,678 Events
$\frac{dN}{du}$
u
CONTENTS
LOWER CHANNEL EDGE
TOTAL CONTENTS = .22678+05 UNDERFLOW = .00000 OVERFLOW = .00000

FIG. 5a

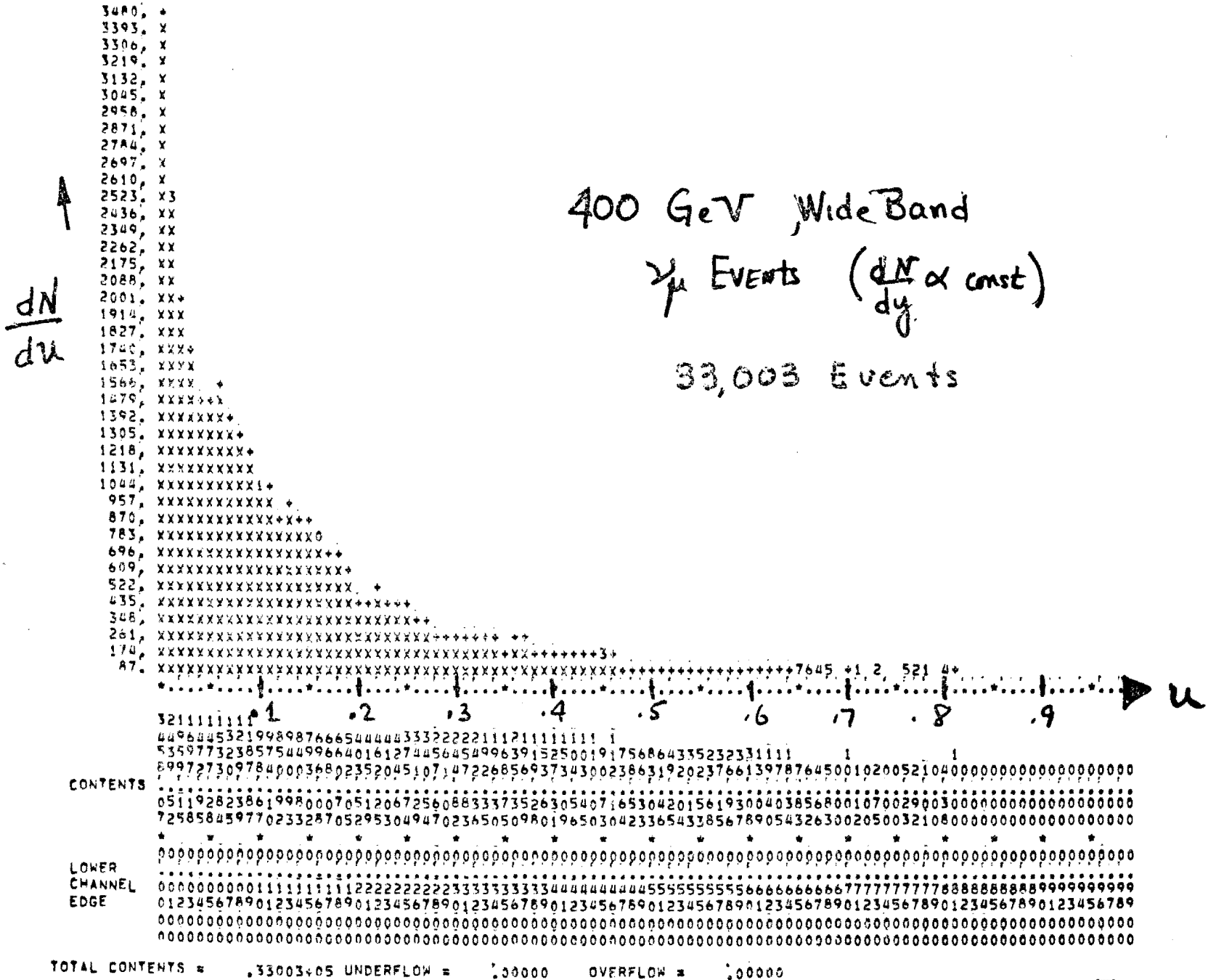
400 GeV, Wide Band
ν_μ Events ($\frac{dN}{dy} \propto$ const)
33,003 Events
$\frac{dN}{du}$
u
CONTENTS
LOWER CHANNEL EDGE
TOTAL CONTENTS = .33003+05 UNDERFLOW = .00000 OVERFLOW = .00000

FIG. 5b

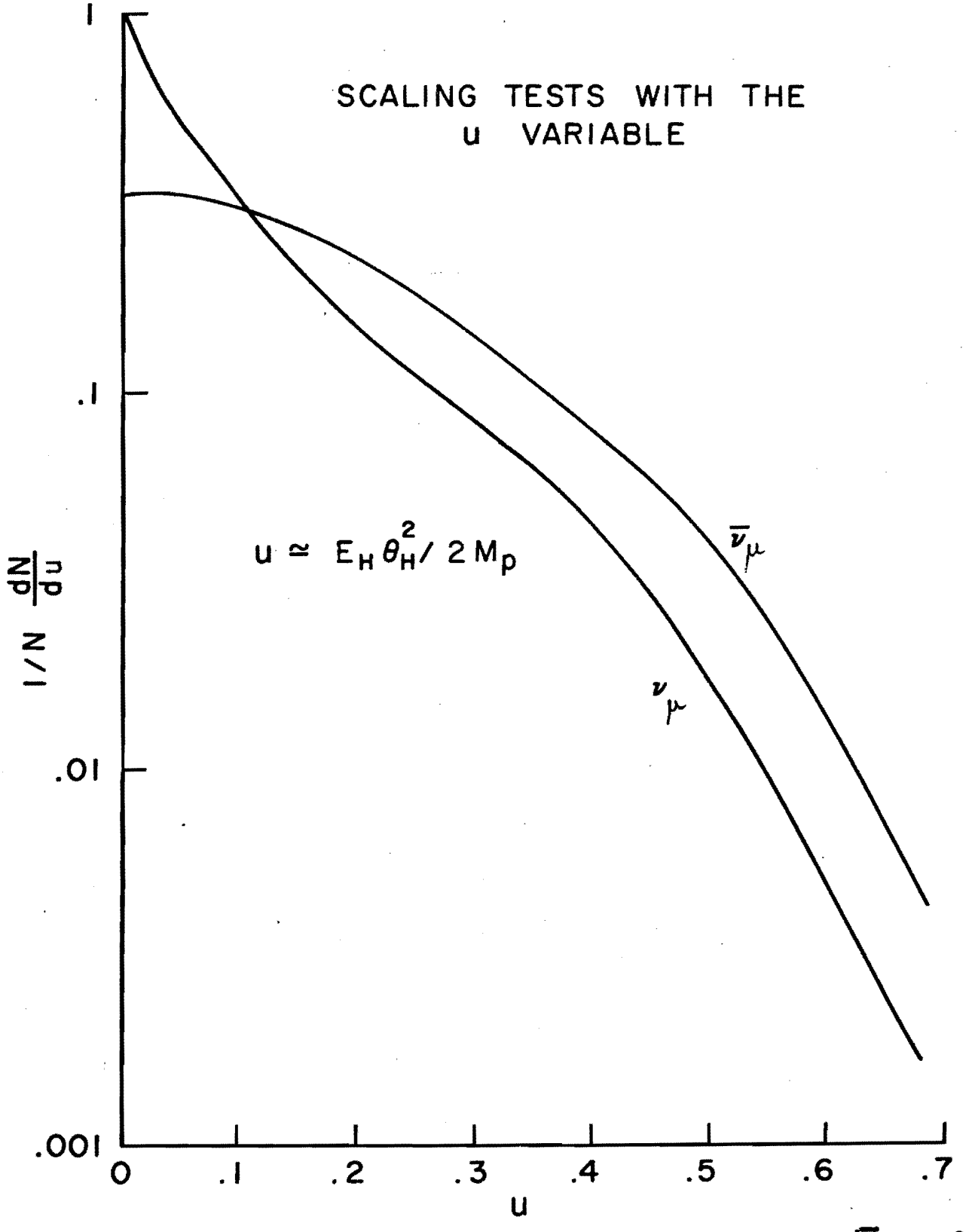
SCALING TESTS WITH THE
u VARIABLE
$u \simeq E_H \theta_H^2 / 2 M_p$
$\bar{\nu}_\mu$
ν_μ
1/N dN/du
1
.1
.01
.001
0
.1
.2
.3
.4
.5
.6
.7
u

FIG. 6

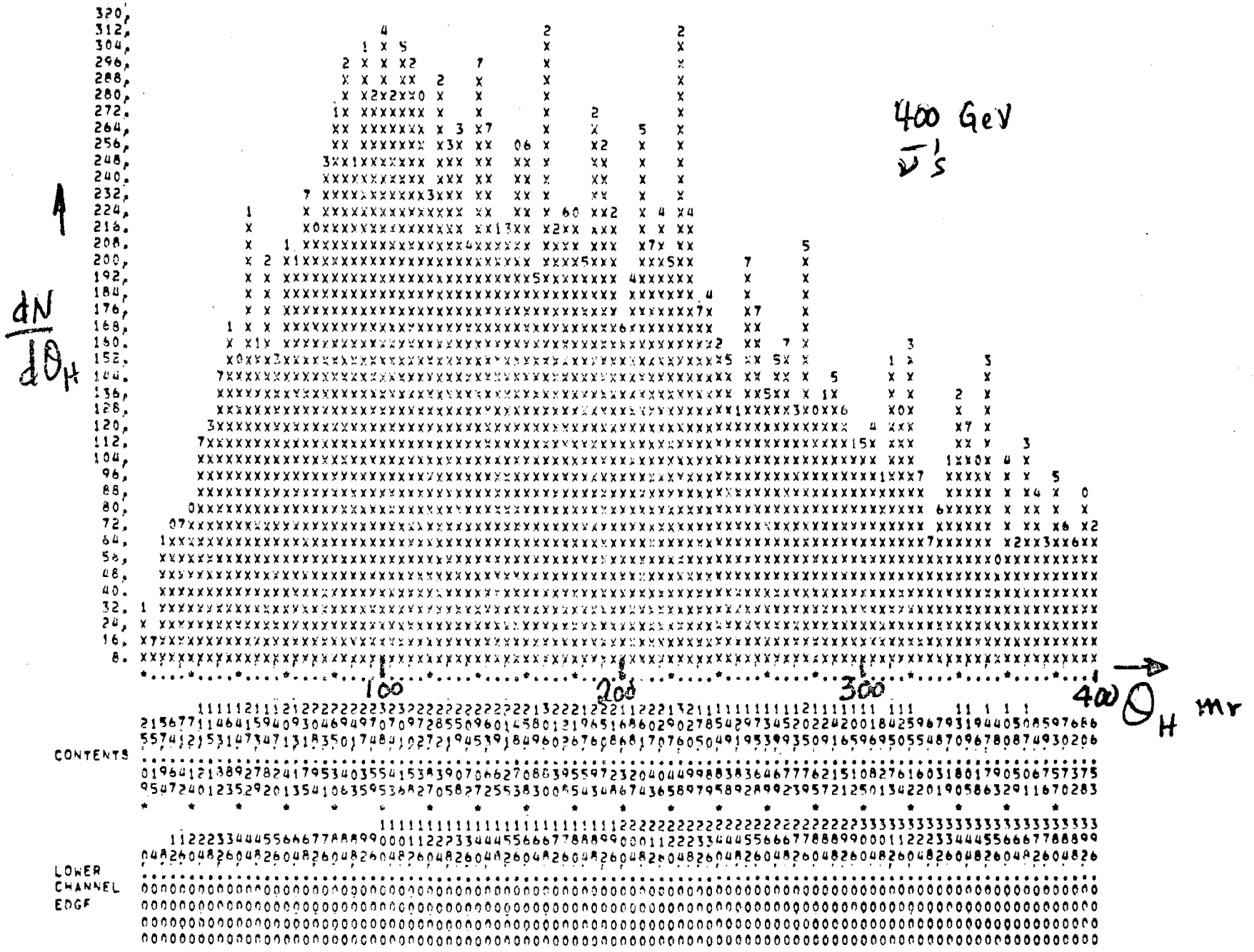
400 GeV
$\bar{\nu}$ s
$\frac{dN}{d\theta_H}$
100
200
300
400
θ_H mr
CONTENTS
LOWER CHANNEL EDGE
TOTAL CONTENTS = .17099+05 UNDERFLOW = .00000 OVERFLOW = .55797+04

FIG. 7

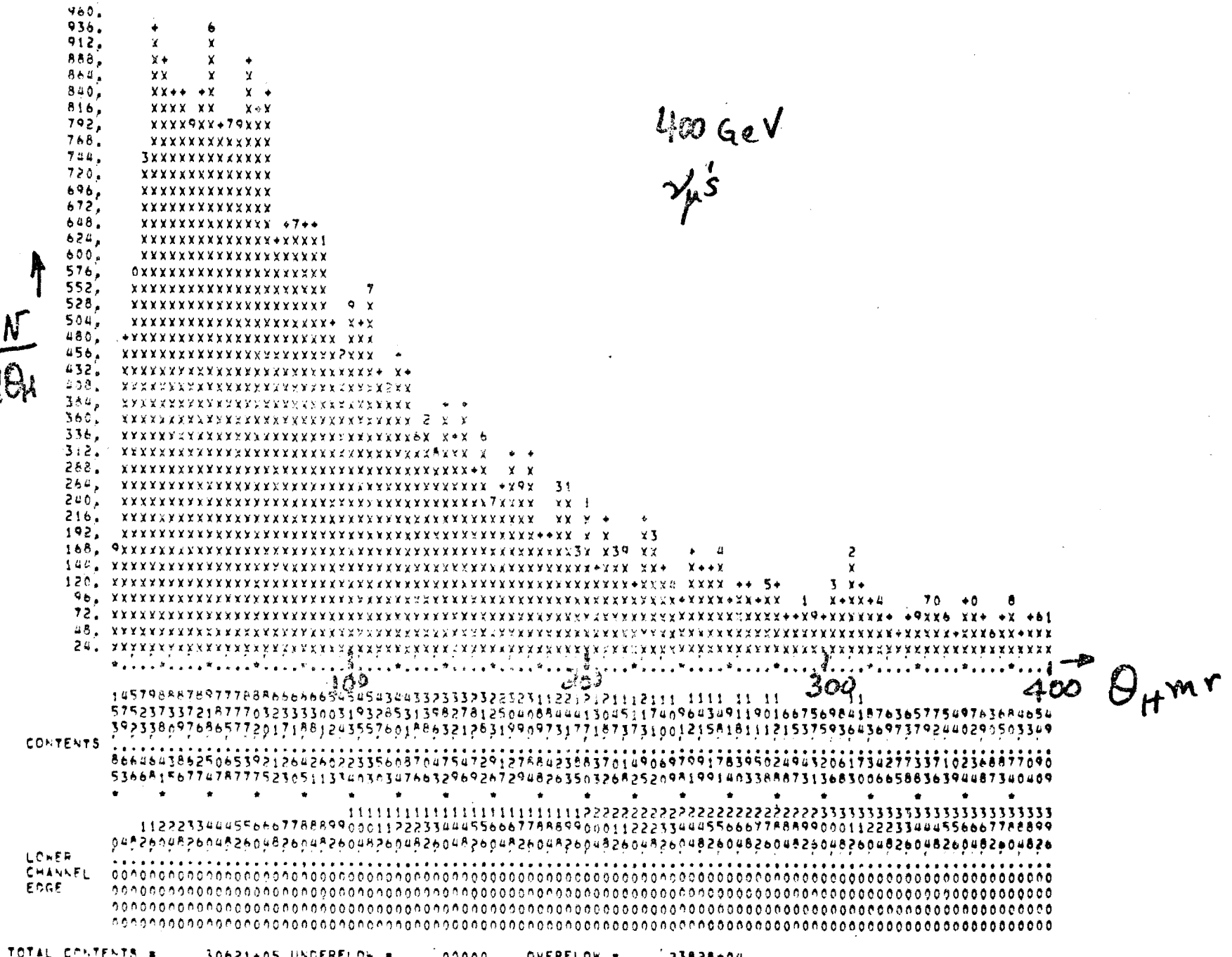
400 GeV
ν_μ's
$\frac{dN}{d\theta_H}$
θ_{H} mr
CONTENTS
LOWER CHANNEL EDGE
TOTAL CONTENTS = .30621+05 UNDERFLOW = .00000 OVERFLOW = .23828+04

FIG 8

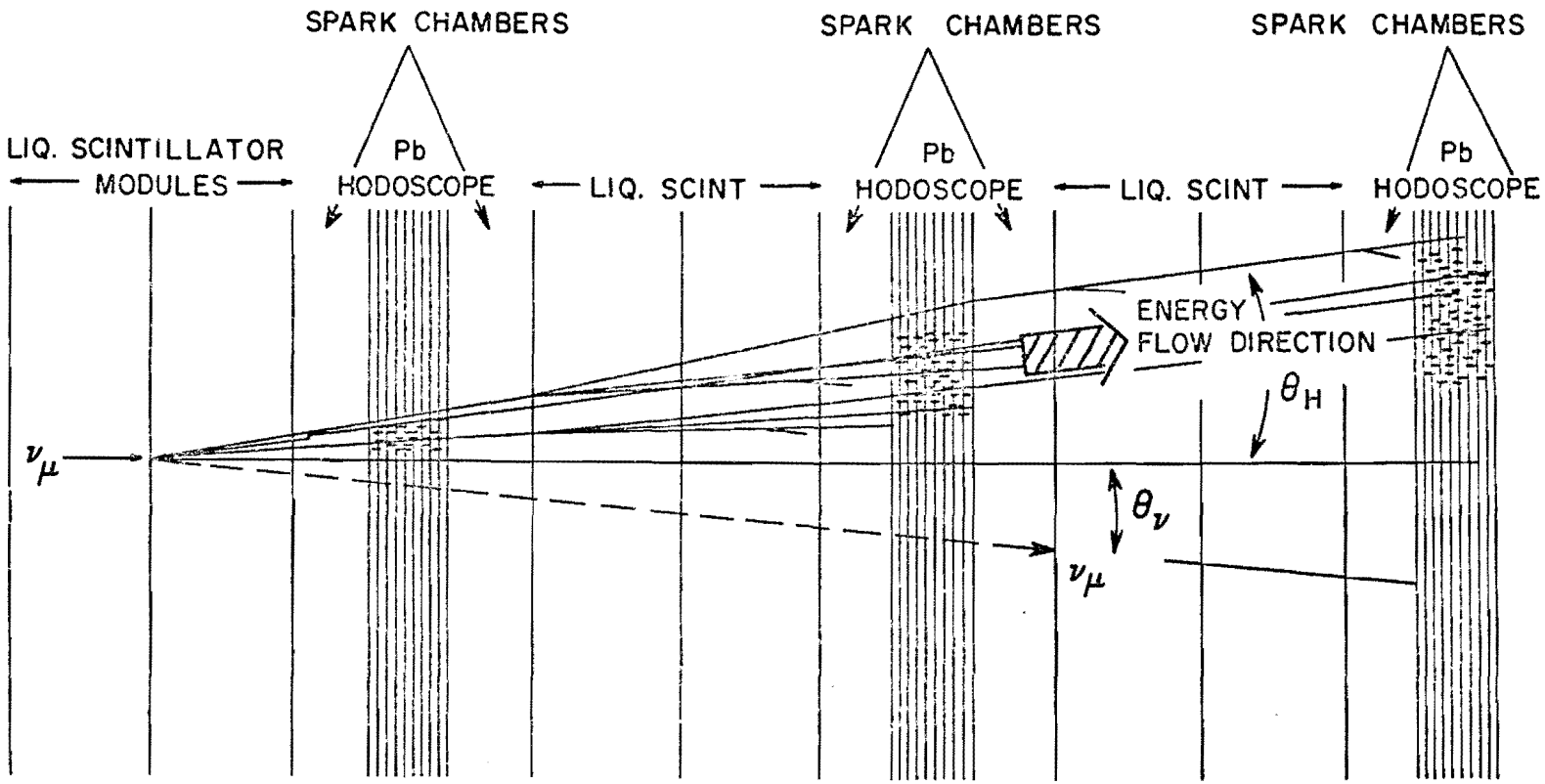

MEASURE θ_H, E_H; FORM SCALING VARIABLE $u \sim E_H \theta_H^2 / 2Mp$.

SCHEMATIC DIAGRAM OF AN EVENT OF TYPE

$\nu_\mu + N \longrightarrow \nu_\mu + X$

Fig 9

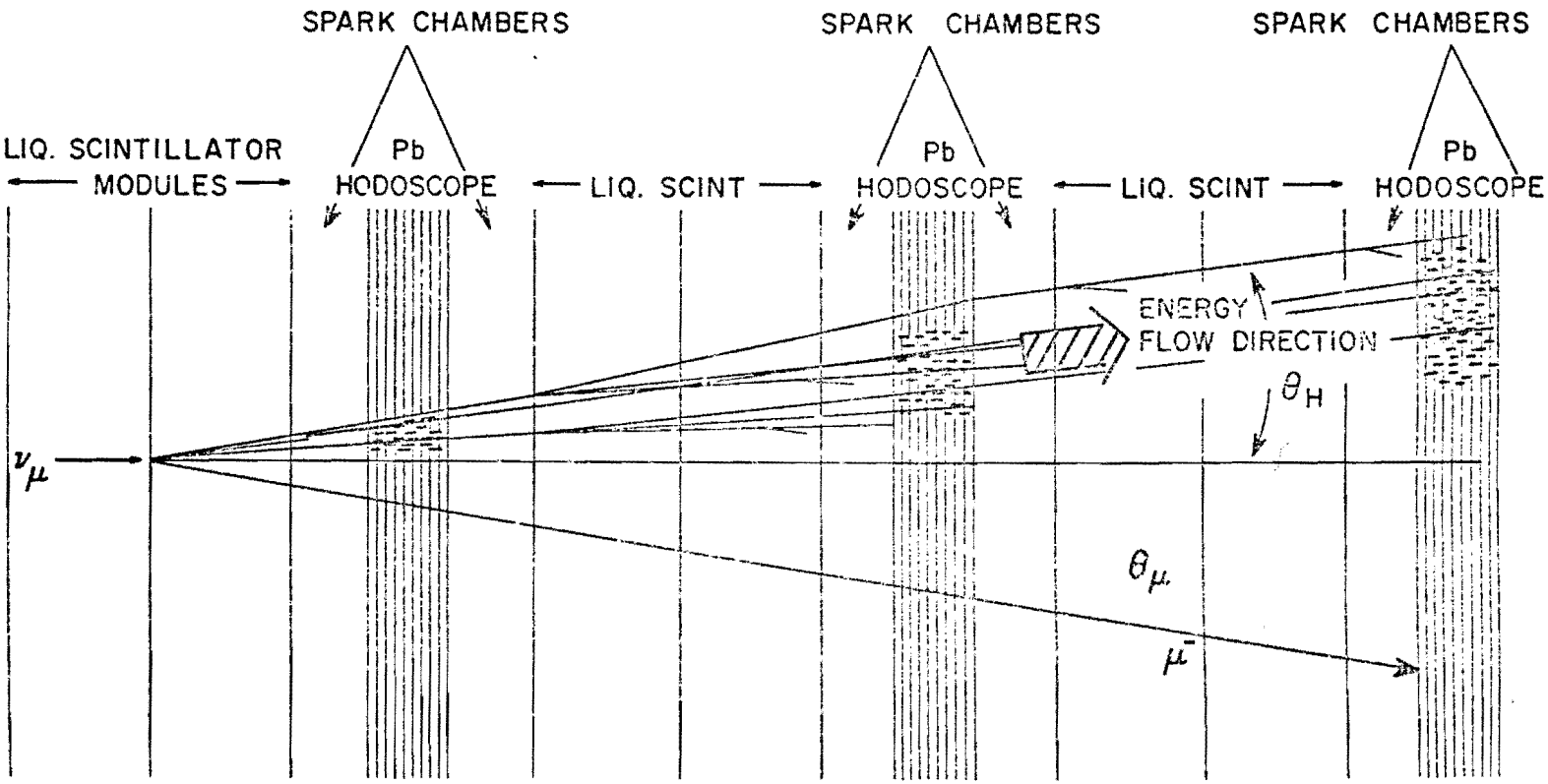

CALIBRATION OF THE ENERGY FLOW DEVICE

USING $\nu_\mu + N \longrightarrow \mu^- + X$

FIG 10

DISTORTION OF THE (x,y) PLOT BY NEW HADRON PRODUCTION

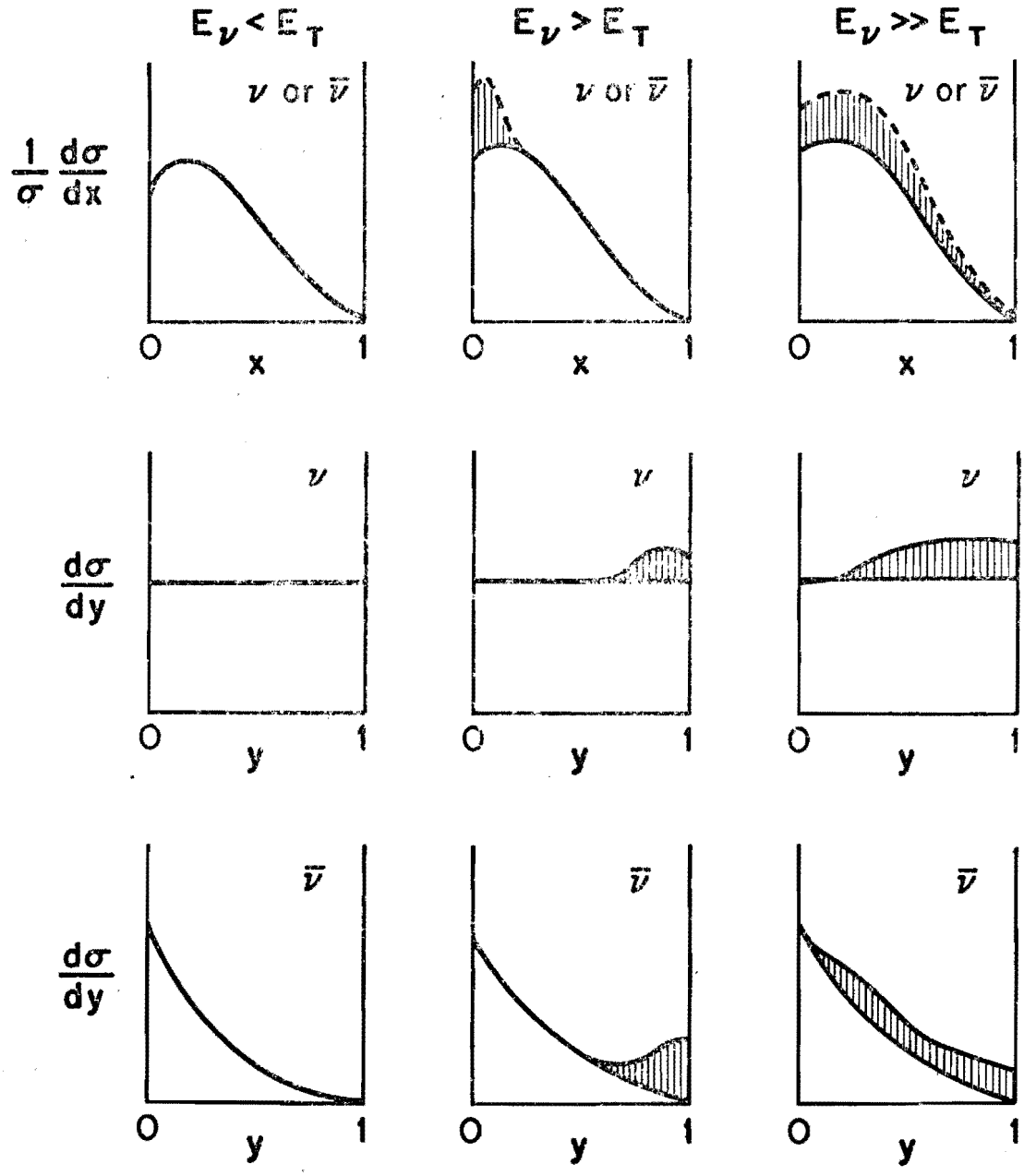

FIG. 11

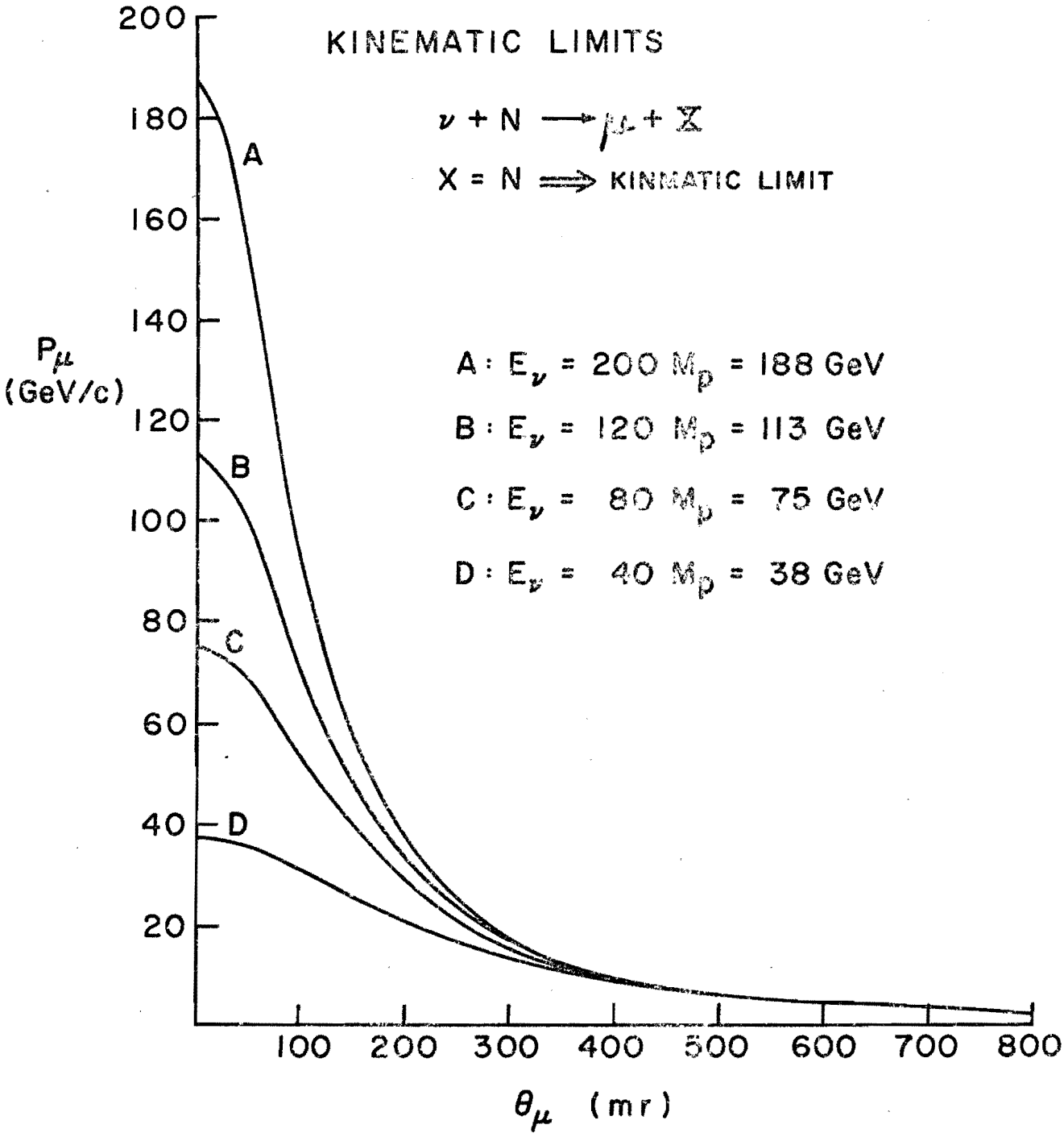
KINEMATIC LIMITS
$\nu + N \longrightarrow \mu + X$
X = N ⟹ KINMATIC LIMIT
A : E_ν = 200 M_p = 188 GeV
B : E_ν = 120 M_p = 113 GeV
C : E_ν = 80 M_p = 75 GeV
D : E_ν = 40 M_p = 38 GeV
P_μ (GeV/c)
200
180
160
140
120
100
80
60
40
20
A
B
C
D
100
200
300
400
500
600
700
800
θ_μ (mr)

Fig 12

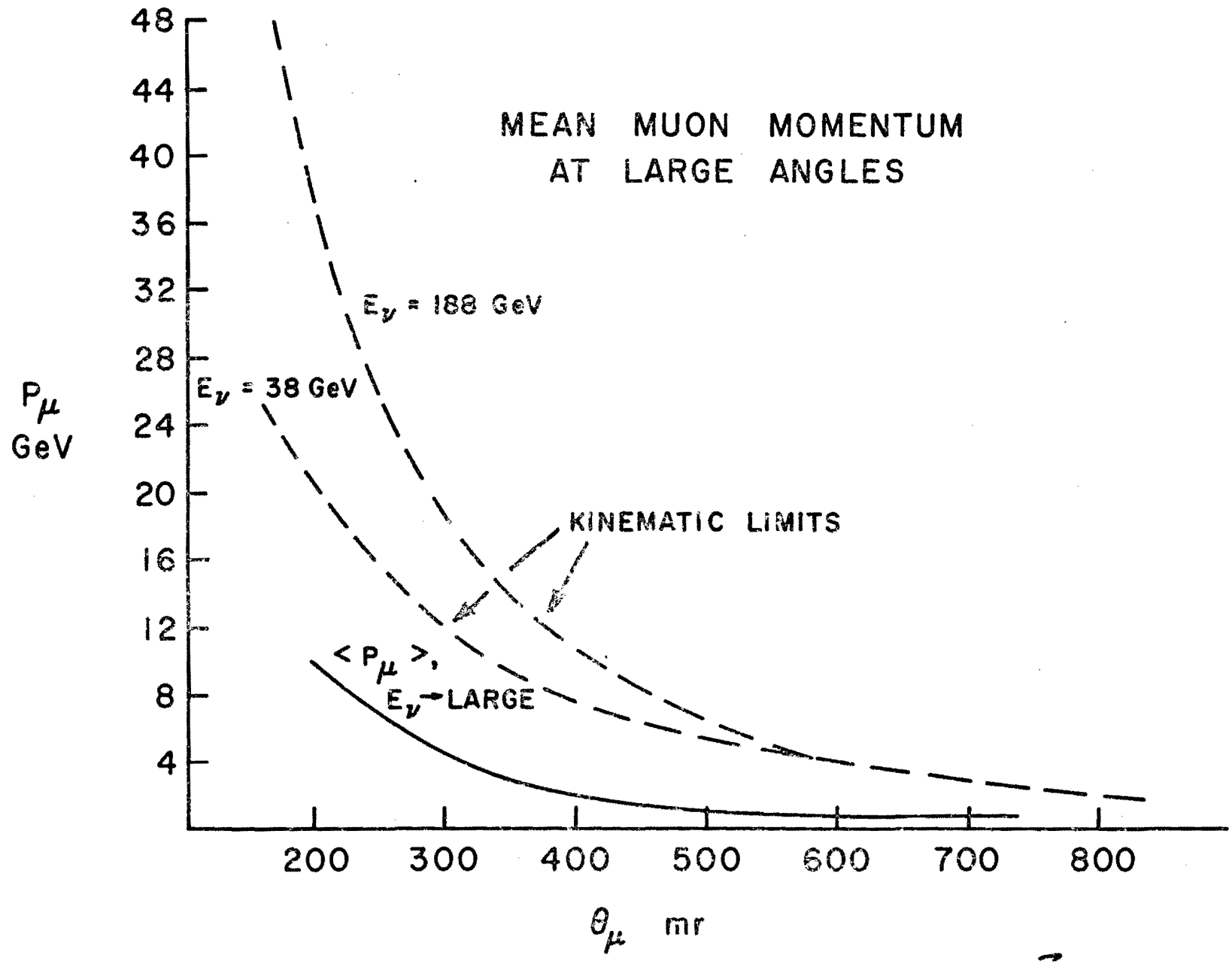
MEAN MUON MOMENTUM
AT LARGE ANGLES
E_ν = 188 GeV
E_ν = 38 GeV
KINEMATIC LIMITS
$\langle P_\mu \rangle$, $E_\nu \to$ LARGE
P_μ GeV
θ_μ mr
48
44
40
36
32
28
24
20
16
12
8
4
200
300
400
500
600
700
800

FIG 13

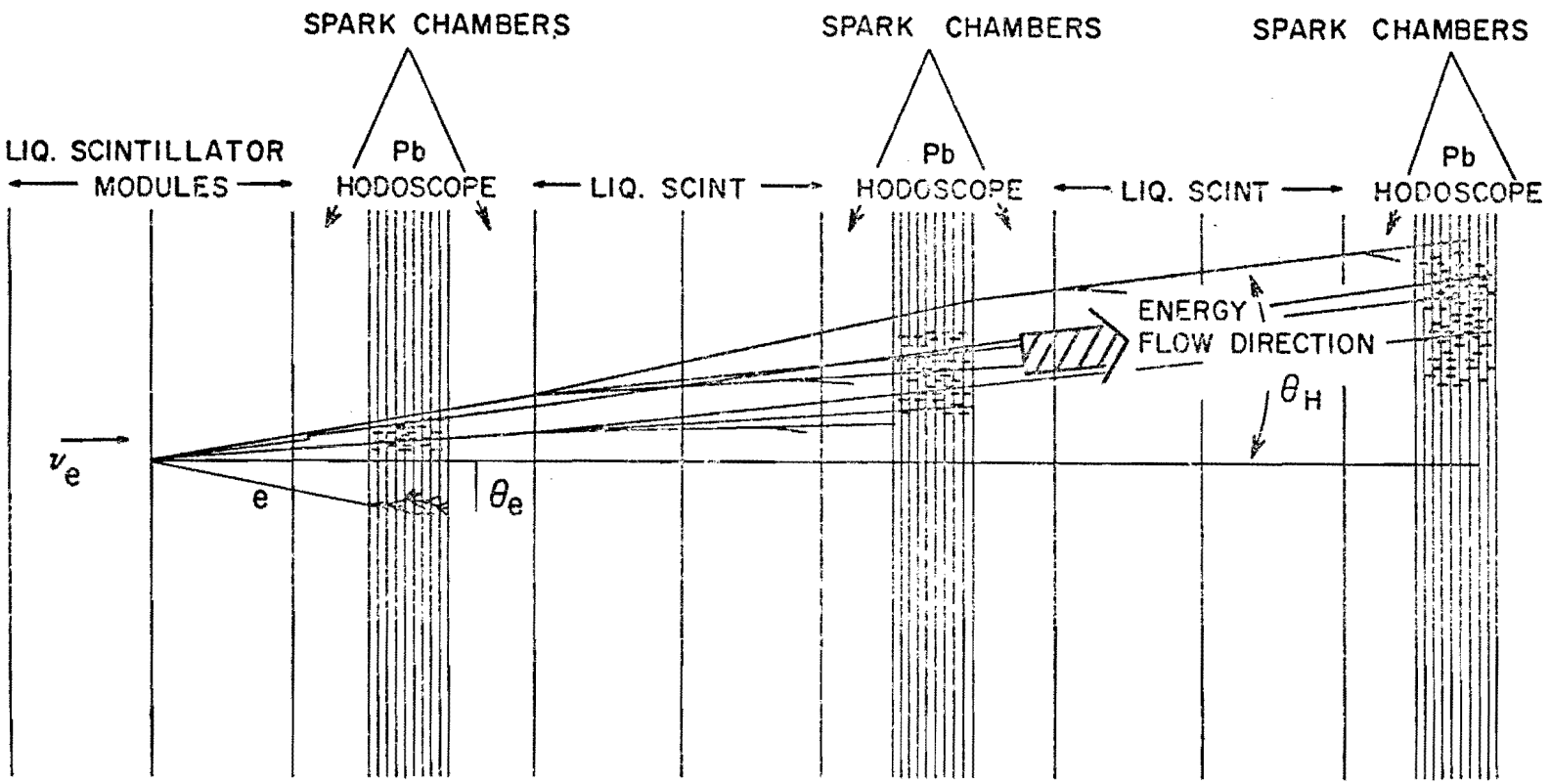

SCHEMATIC DIAGRAM OF AN EVENT OF TYPE

$\nu_e + N \longrightarrow e + X$

Fig 14

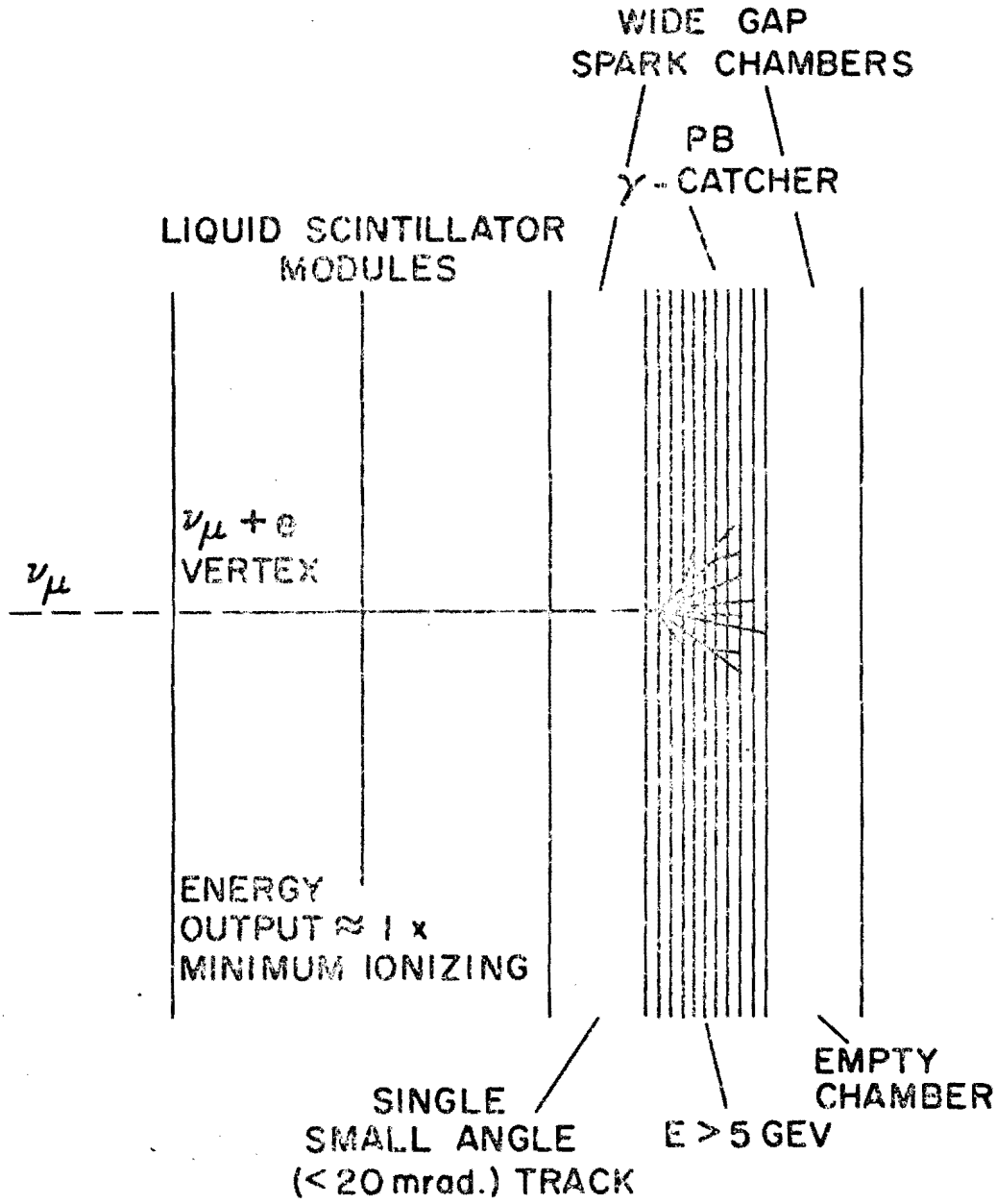

SCHEMATIC DIAGRAM OF AN EVENT OF TYPE

$\nu_\mu + e \longrightarrow \nu_\mu + e$

FIG 15

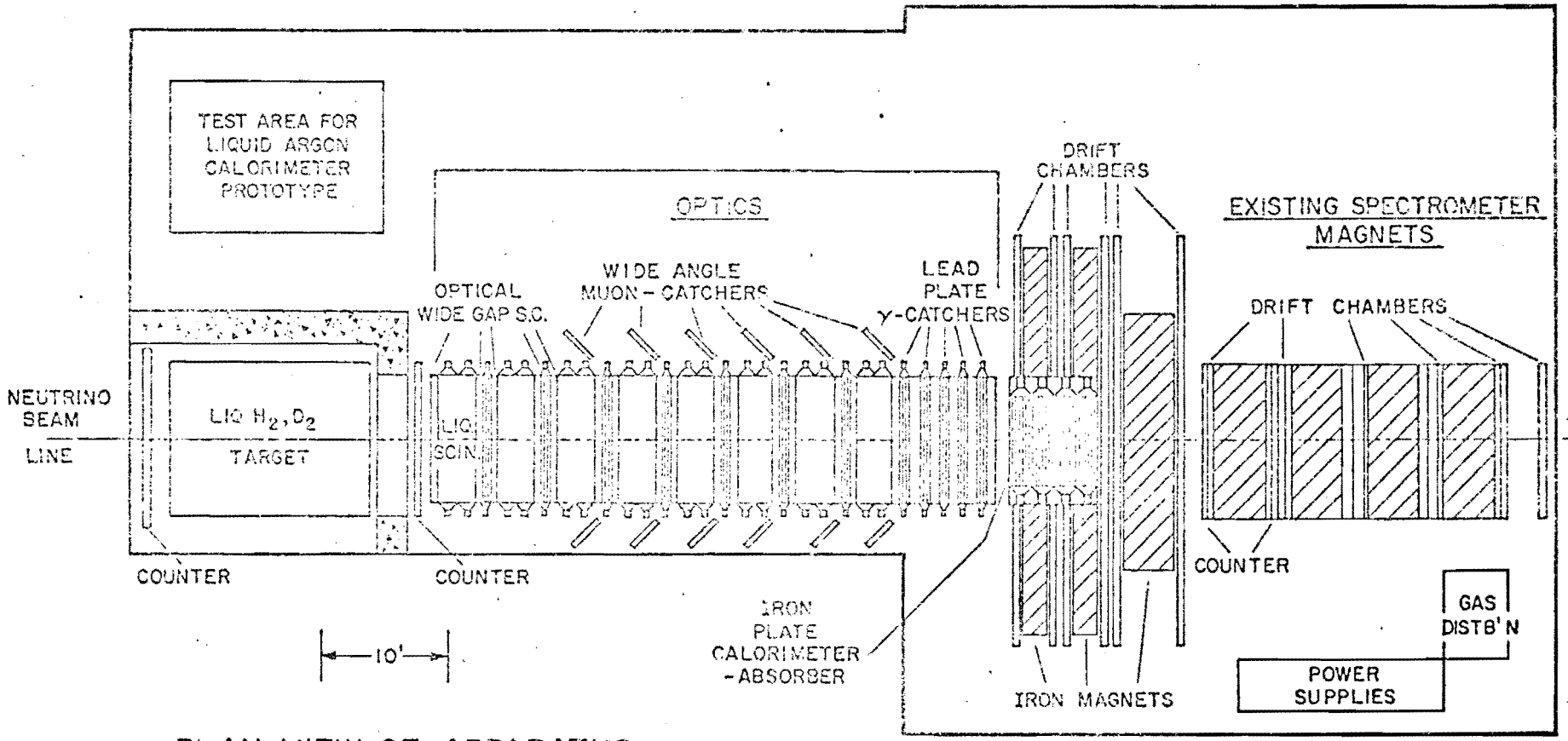

PLAN VIEW OF APPARATUS

EARLY, 1975

FIG 16

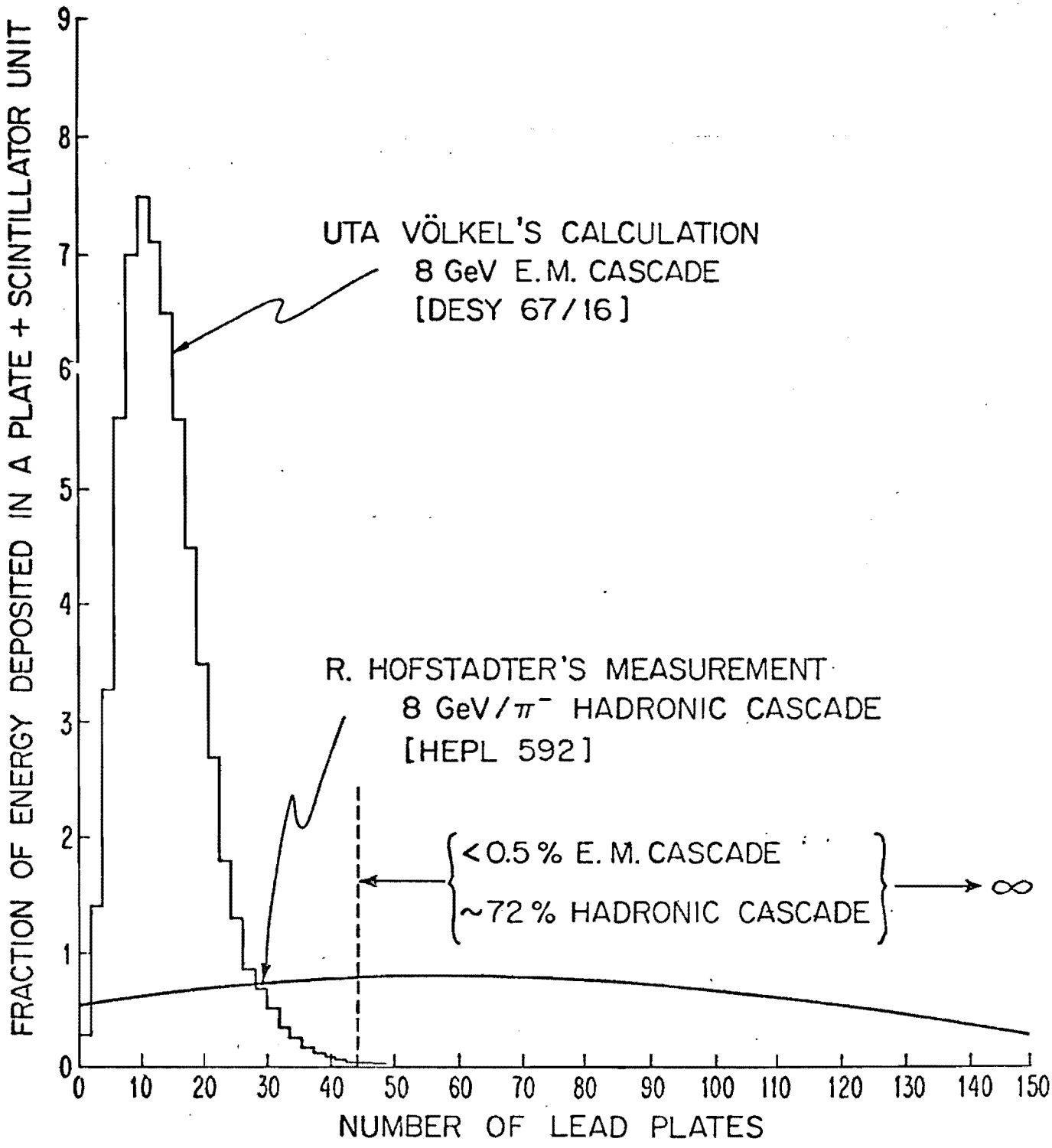
FRACTION OF ENERGY DEPOSITED IN A PLATE + SCINTILLATOR UNIT
NUMBER OF LEAD PLATES
UTA VÖLKEL'S CALCULATION
8 GeV E.M. CASCADE
[DESY 67/16]
R. HOFSTADTER'S MEASUREMENT
8 GeV/π⁻ HADRONIC CASCADE
[HEPL 592]
<0.5% E.M. CASCADE
~72% HADRONIC CASCADE
∞

FIG 17

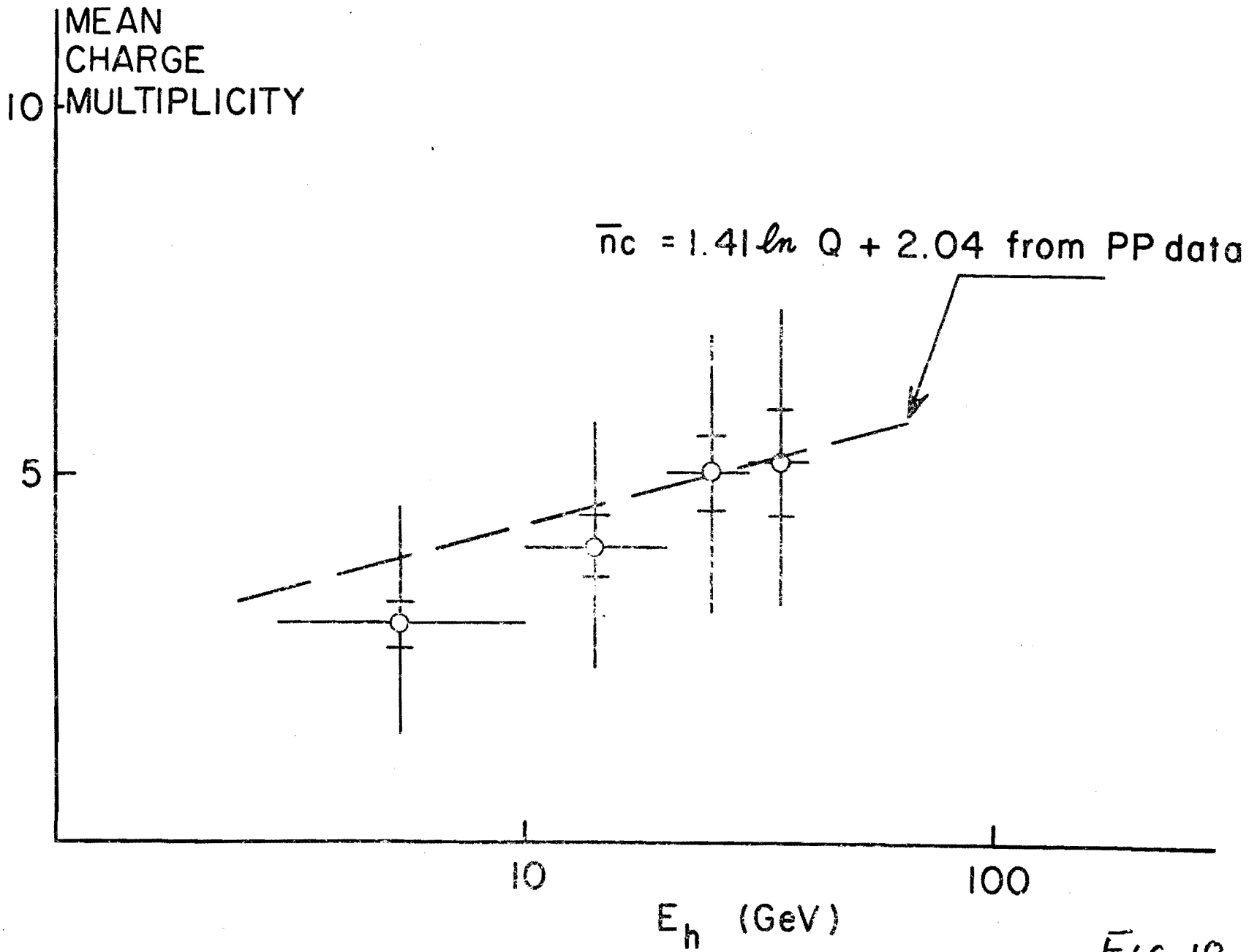
MEAN
CHARGE
MULTIPLICITY
10
5
$\bar{n}c = 1.41 \ln Q + 2.04$ from PP data
10
100
E_h (GeV)

FIG 18

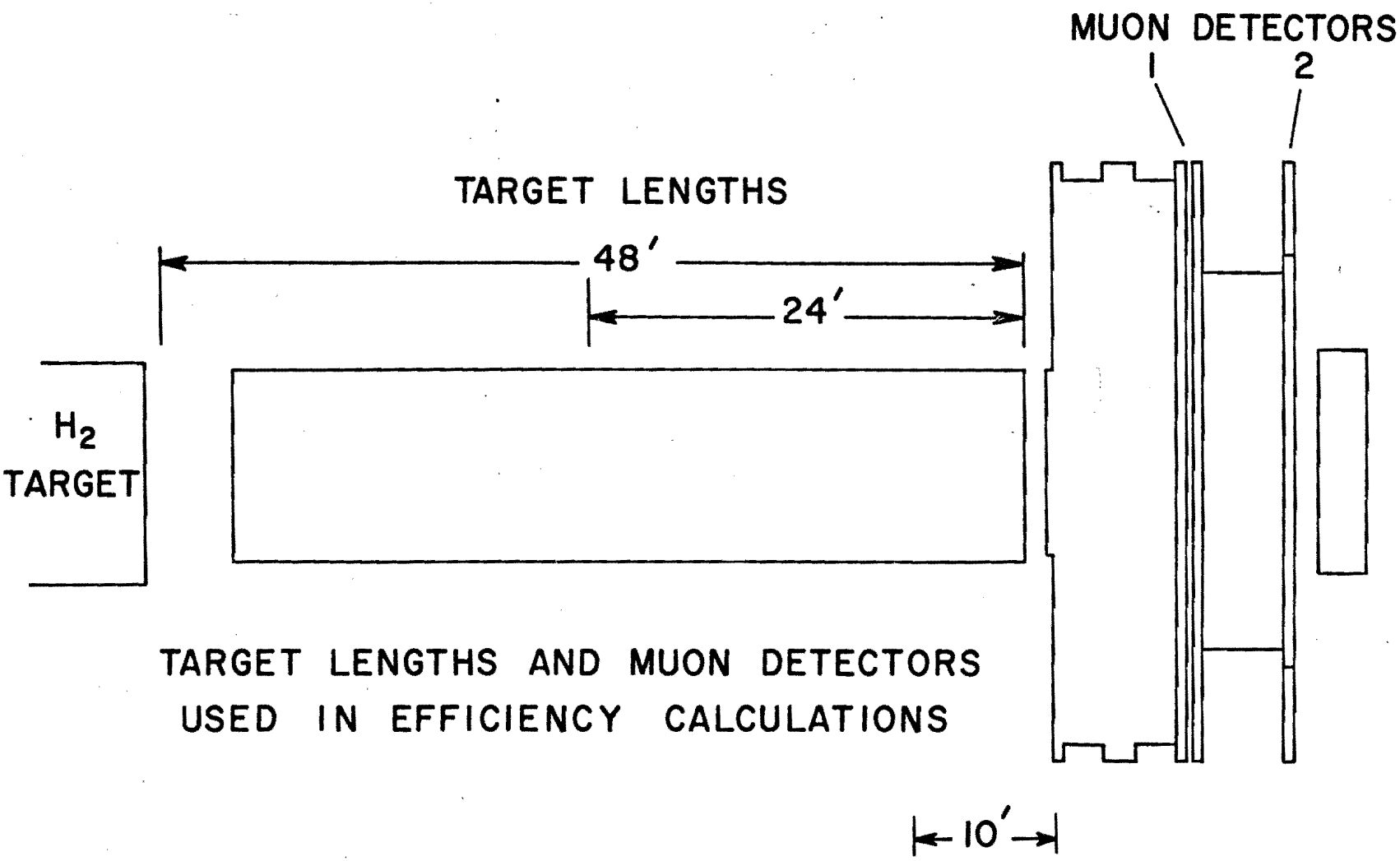

TARGET LENGTHS AND MUON DETECTORS
USED IN EFFICIENCY CALCULATIONS

FIG. 19

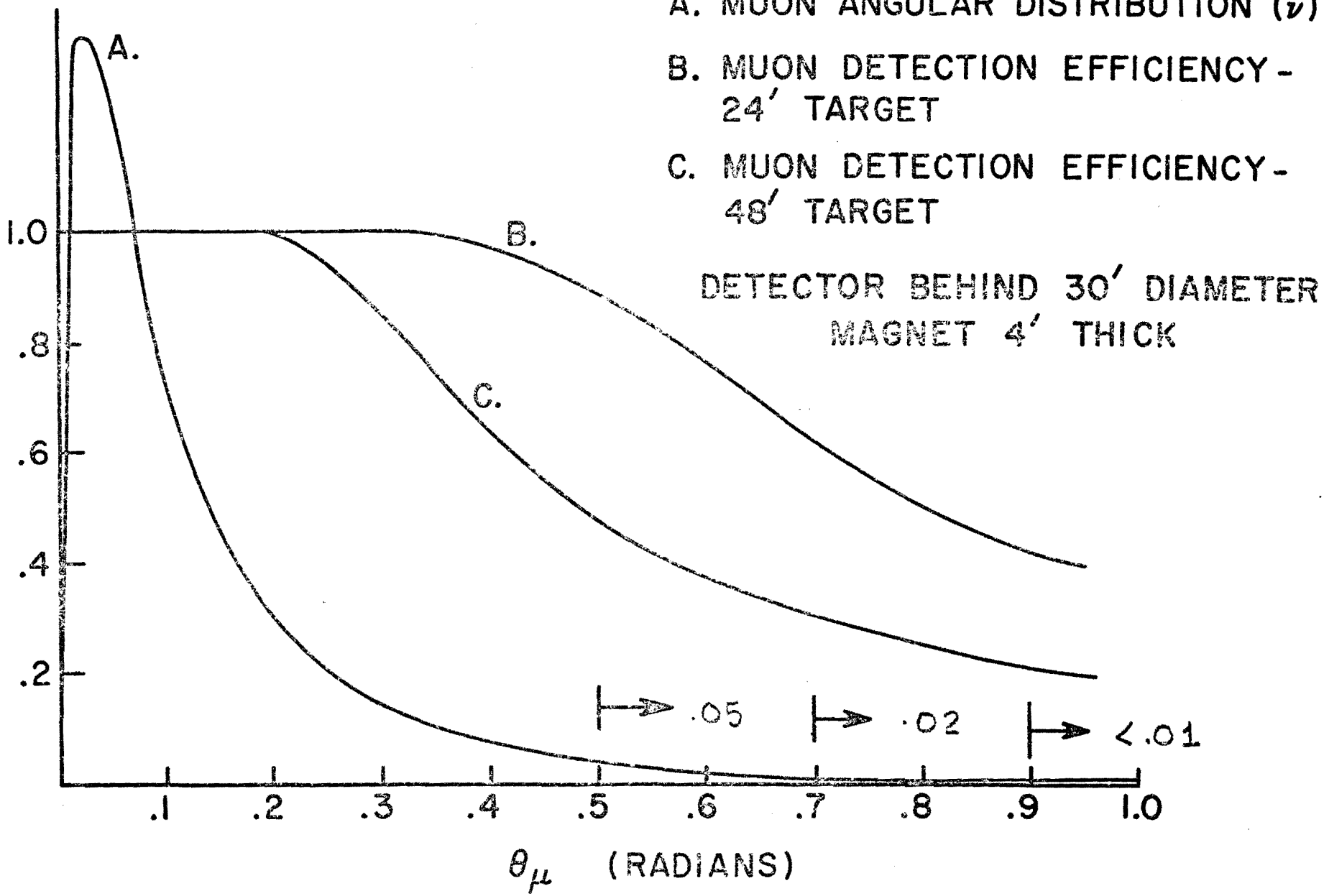
A. MUON ANGULAR DISTRIBUTION (ν)
B. MUON DETECTION EFFICIENCY - 24′ TARGET
C. MUON DETECTION EFFICIENCY - 48′ TARGET
DETECTOR BEHIND 30′ DIAMETER MAGNET 4′ THICK
A.
B.
C.
1.0
.8
.6
.4
.2
.05
.02
<.01
.1
.2
.3
.4
.5
.6
.7
.8
.9
1.0
θμ (RADIANS)

FIG 20

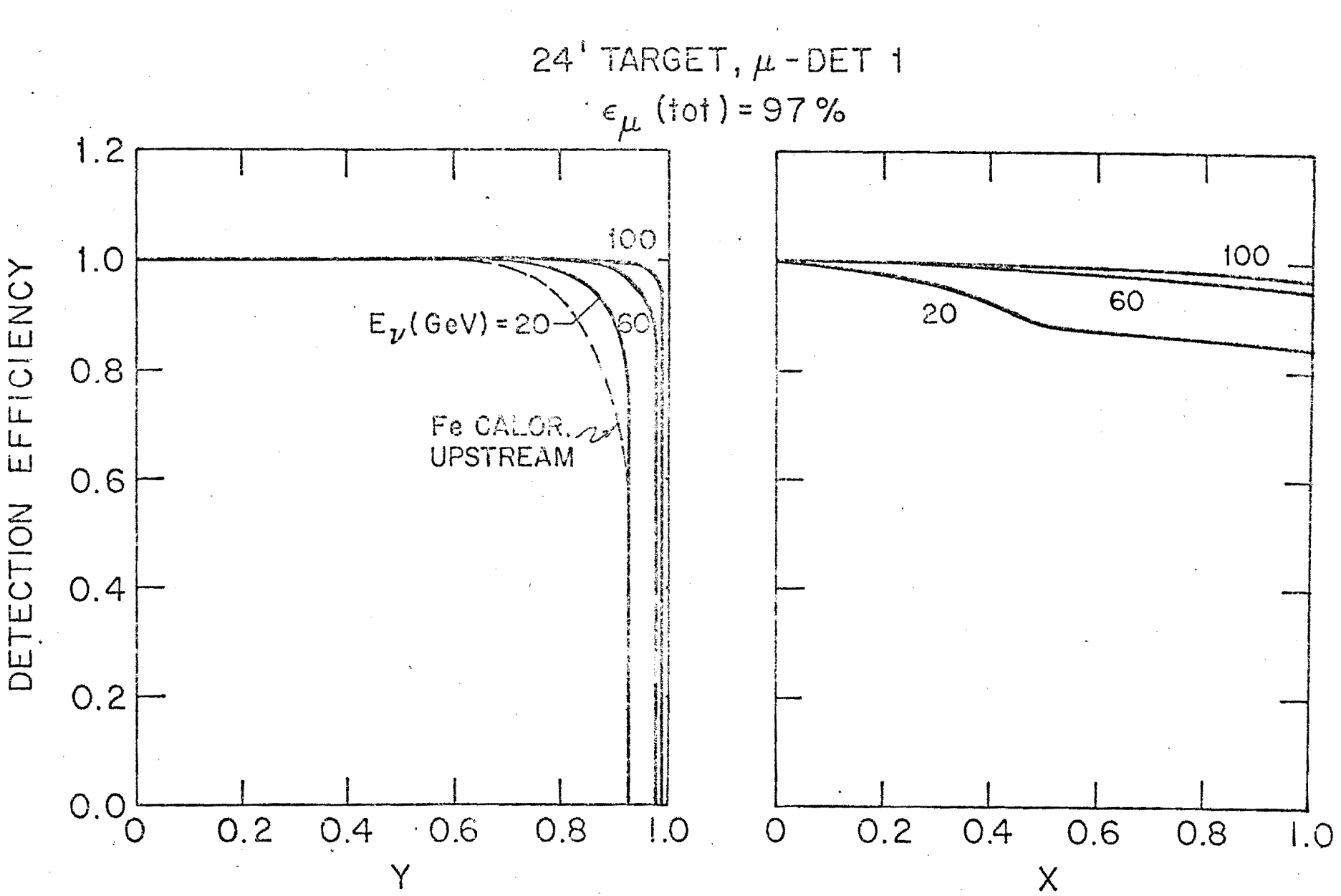
24' TARGET, μ-DET 1
ϵ_μ (tot) = 97 %
DETECTION EFFICIENCY
1.2
1.0
0.8
0.6
0.4
0.2
0.0
0
0.2
0.4
0.6
0.8
1.0
Y
X
100
60
20
E_ν(GeV) = 20
Fe CALOR. UPSTREAM

FIG 21

FIG 22

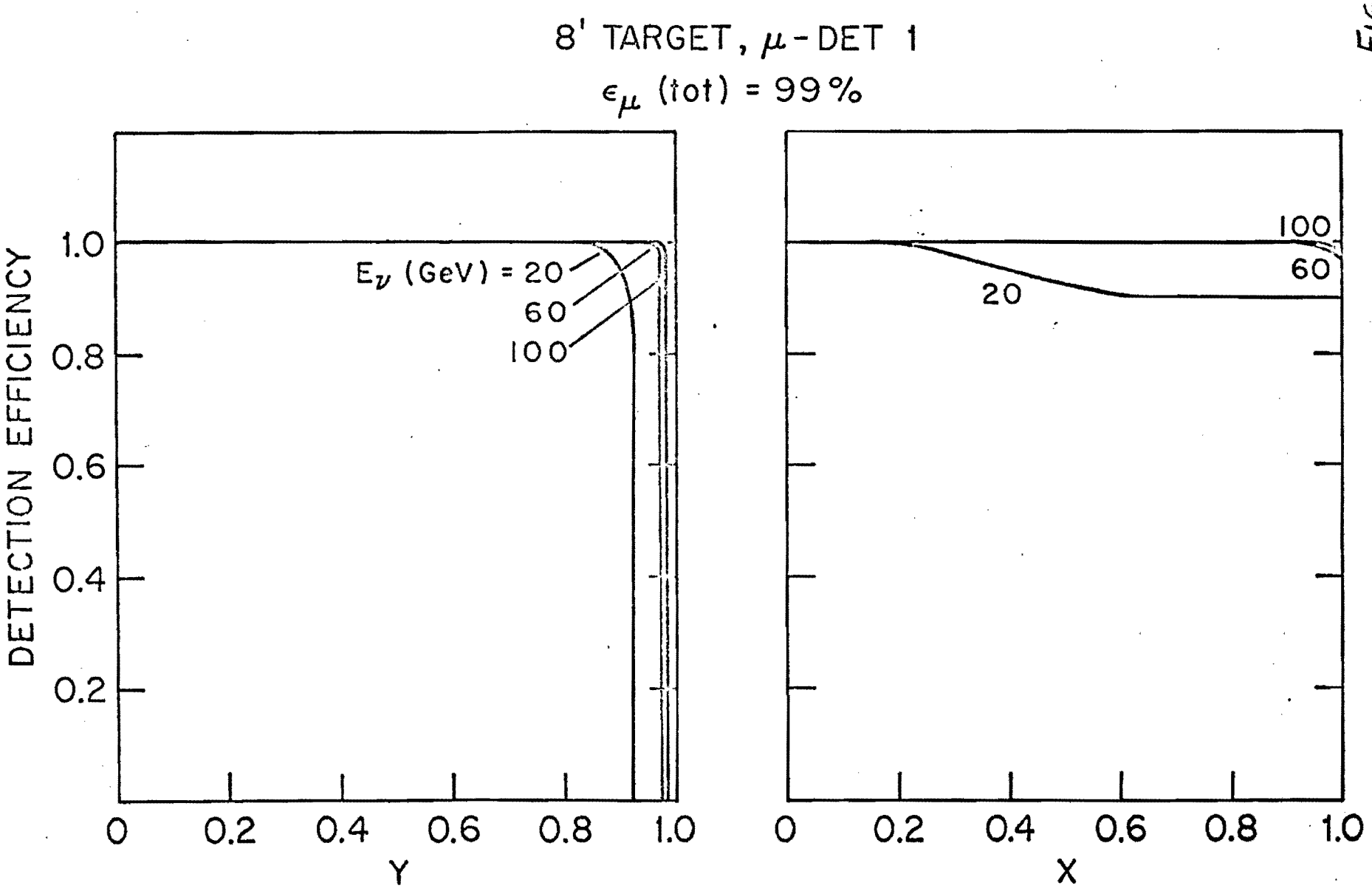
8' TARGET, μ-DET 1
ϵ_μ (tot) = 99%
DETECTION EFFICIENCY
1.0
0.8
0.6
0.4
0.2
E_ν (GeV) = 20
60
100
0
0.2
0.4
0.6
0.8
1.0
Y
100
60
20
0
0.2
0.4
0.6
0.8
1.0
X

FIG 23

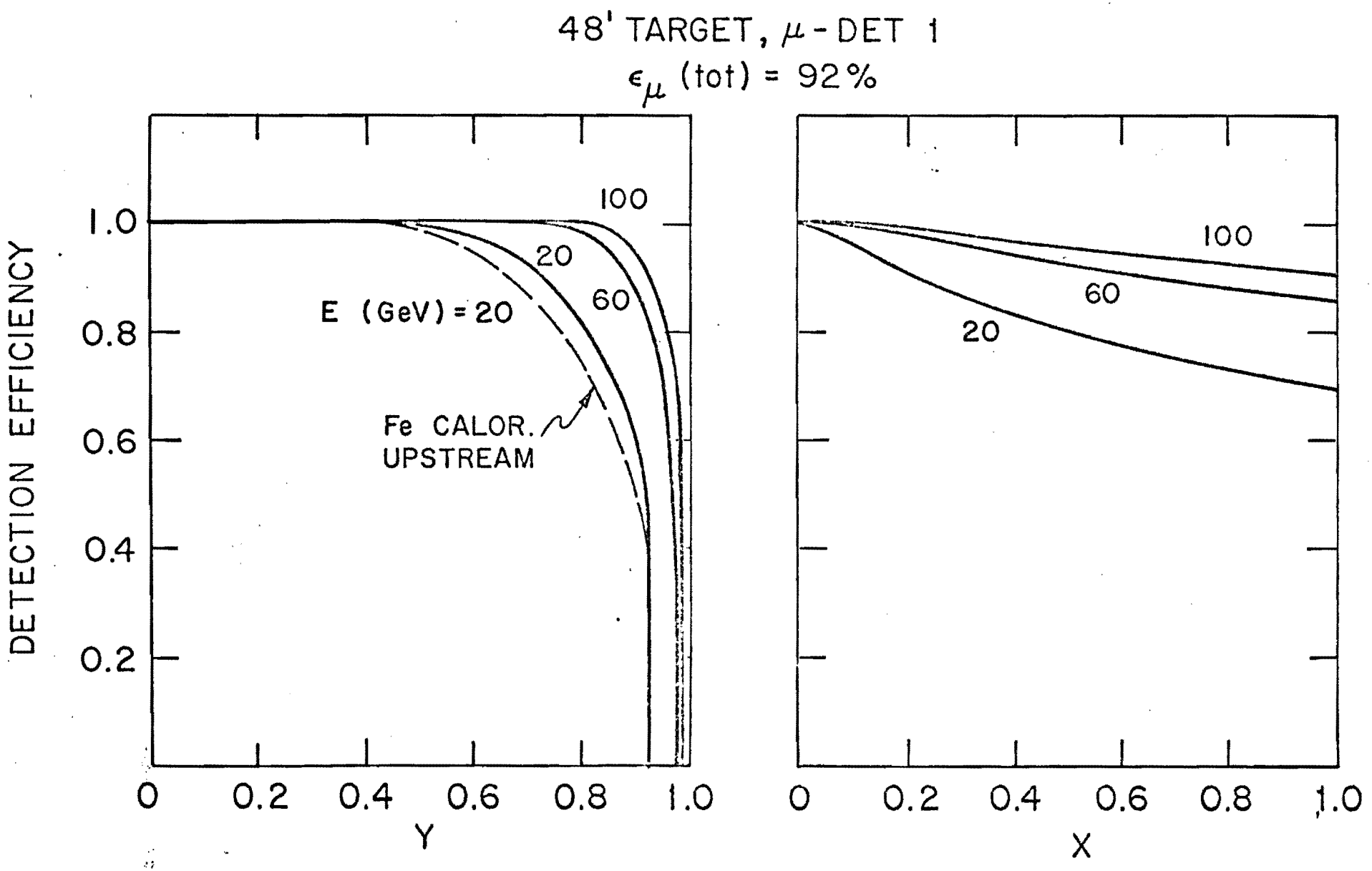
48' TARGET, μ - DET 1
ϵ_μ (tot) = 92%
DETECTION EFFICIENCY
1.0
0.8
0.6
0.4
0.2
0
0.2
0.4
0.6
0.8
1.0
Y
X
100
20
60
E (GeV) = 20
Fe CALOR.
UPSTREAM
100
60
20

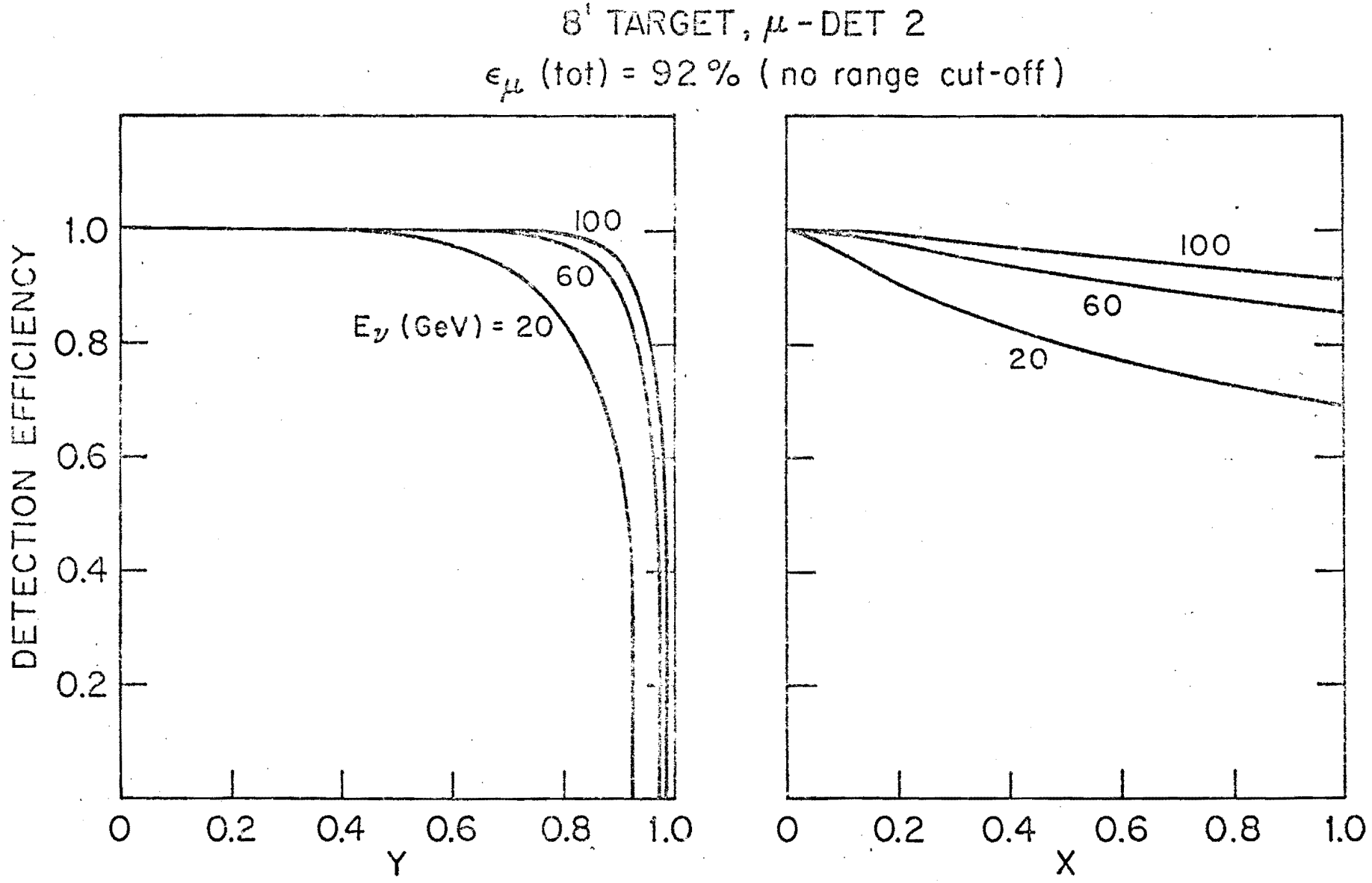
8' TARGET, μ-DET 2
ϵ_μ (tot) = 92 % (no range cut-off)
DETECTION EFFICIENCY
1.0
0.8
0.6
0.4
0.2
0
0.2
0.4
0.6
0.8
1.0
Y
X
100
60
20
E_ν (GeV) = 20

FIG. 24

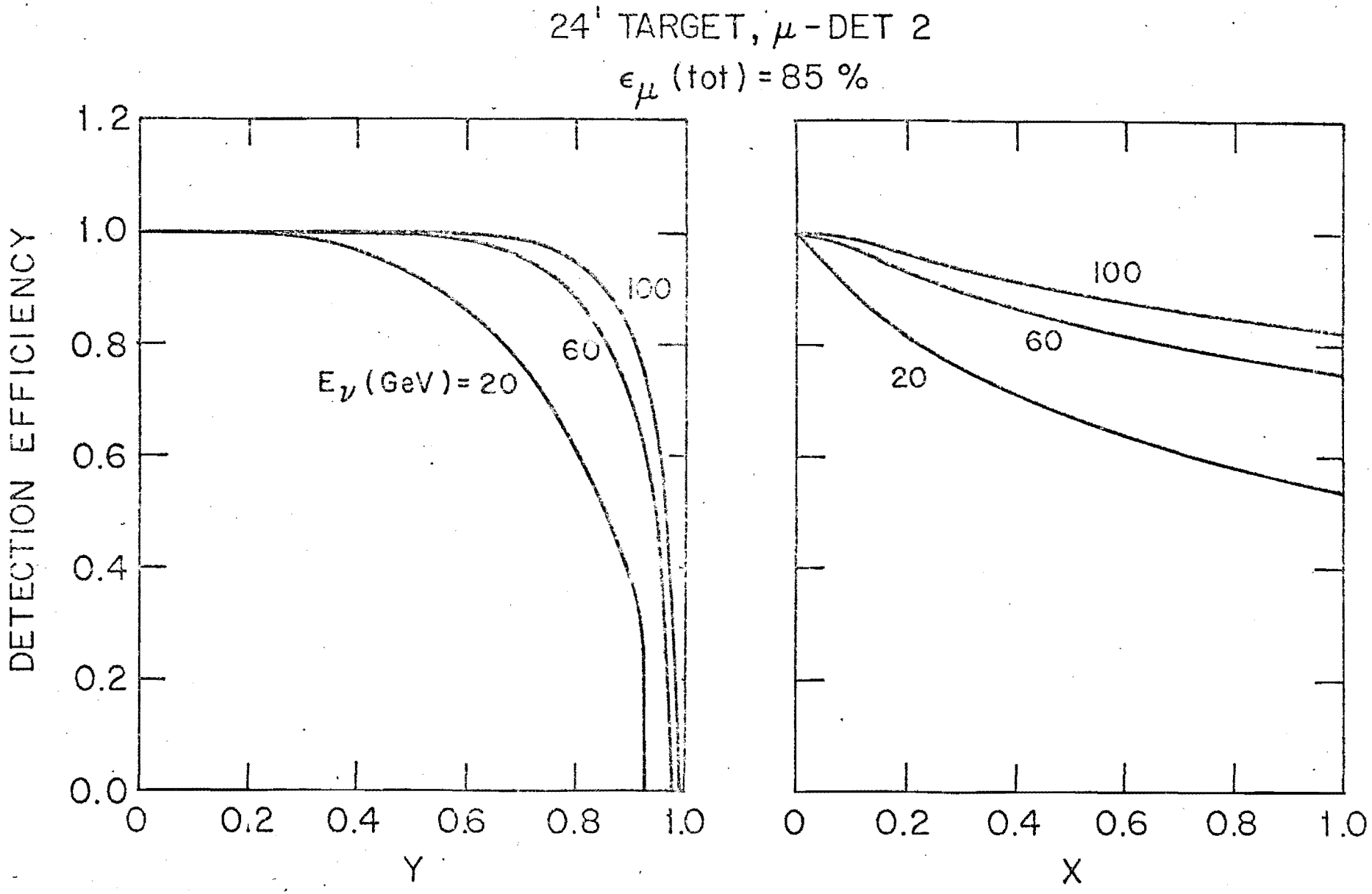
24' TARGET, μ-DET 2
ϵ_μ (tot) = 85 %
DETECTION EFFICIENCY
1.2
1.0
0.8
0.6
0.4
0.2
0.0
0
0.2
0.4
0.6
0.8
1.0
Y
X
100
60
20
E_ν (GeV) = 20

FIG. 25

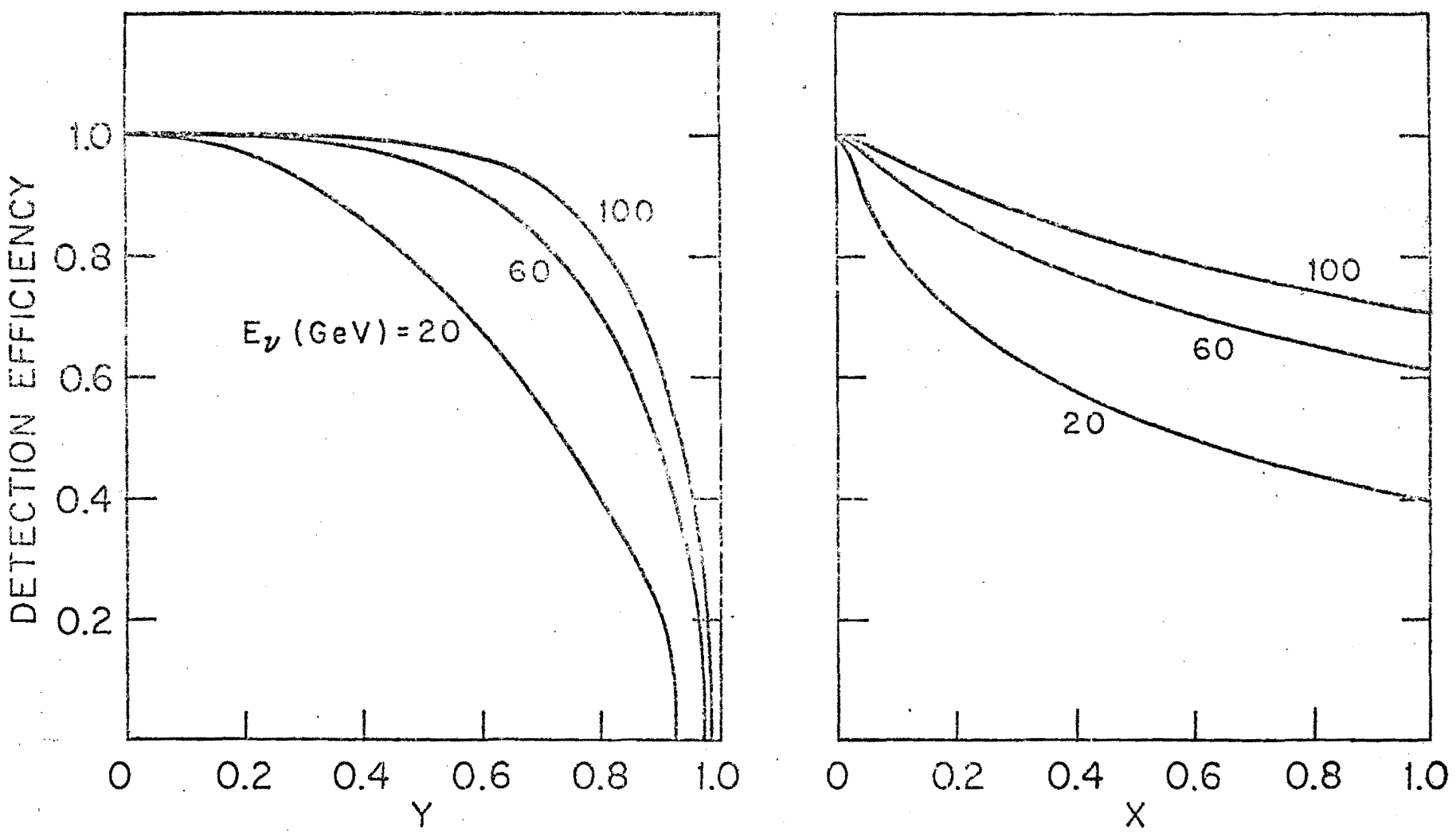
48' TARGET, μ-DET 2
ϵ_μ (tot) = 75 %
DETECTION EFFICIENCY
1.0
0.8
0.6
0.4
0.2
0
0.2
0.4
0.6
0.8
1.0
Y
X
100
60
20
E_ν (GeV) = 20

FIG. 26

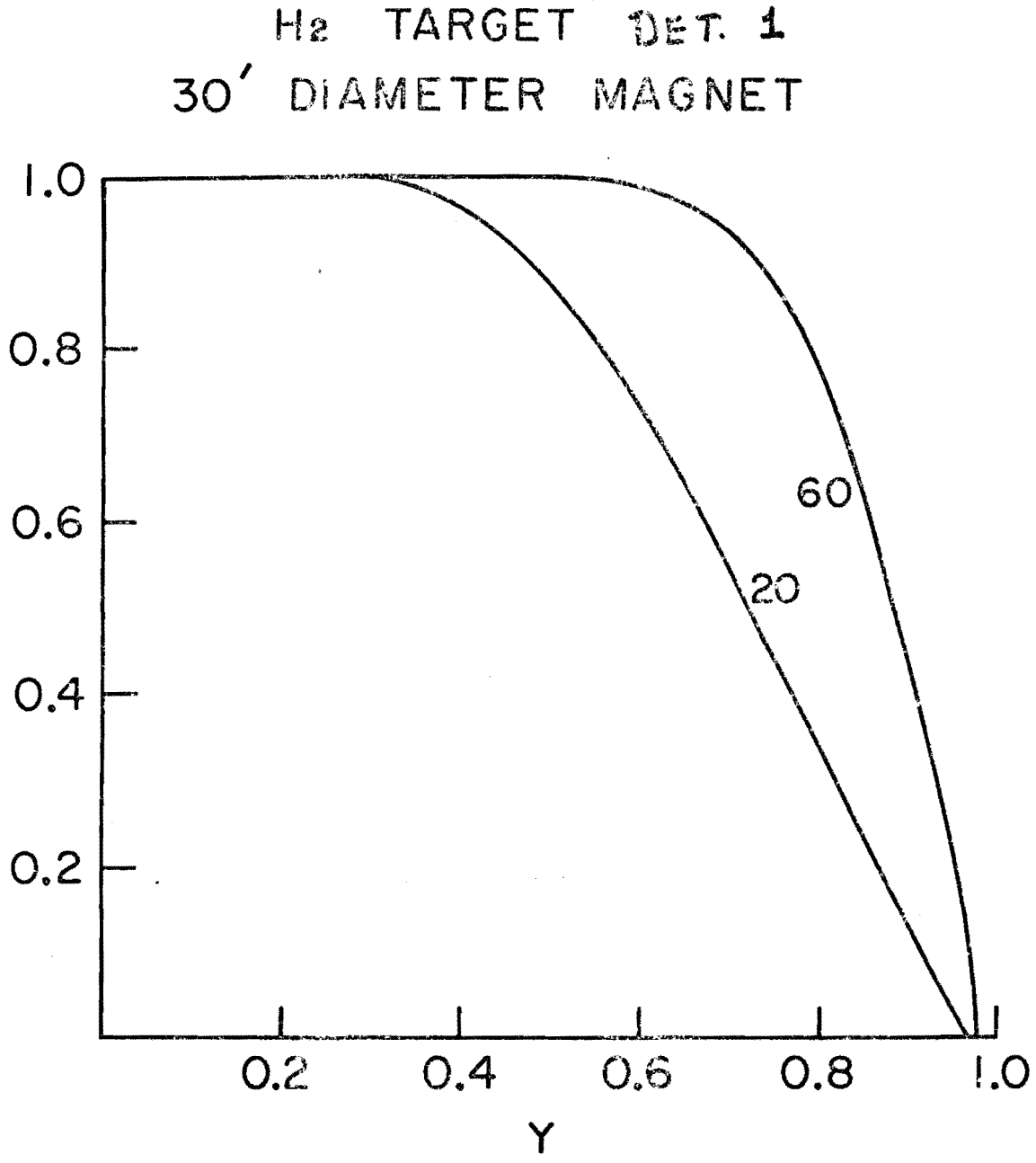
H2 TARGET DET. 1
30' DIAMETER MAGNET
1.0
0.8
0.6
0.4
0.2
60
20
0.2
0.4
0.6
0.8
1.0
Y

FIG 27a

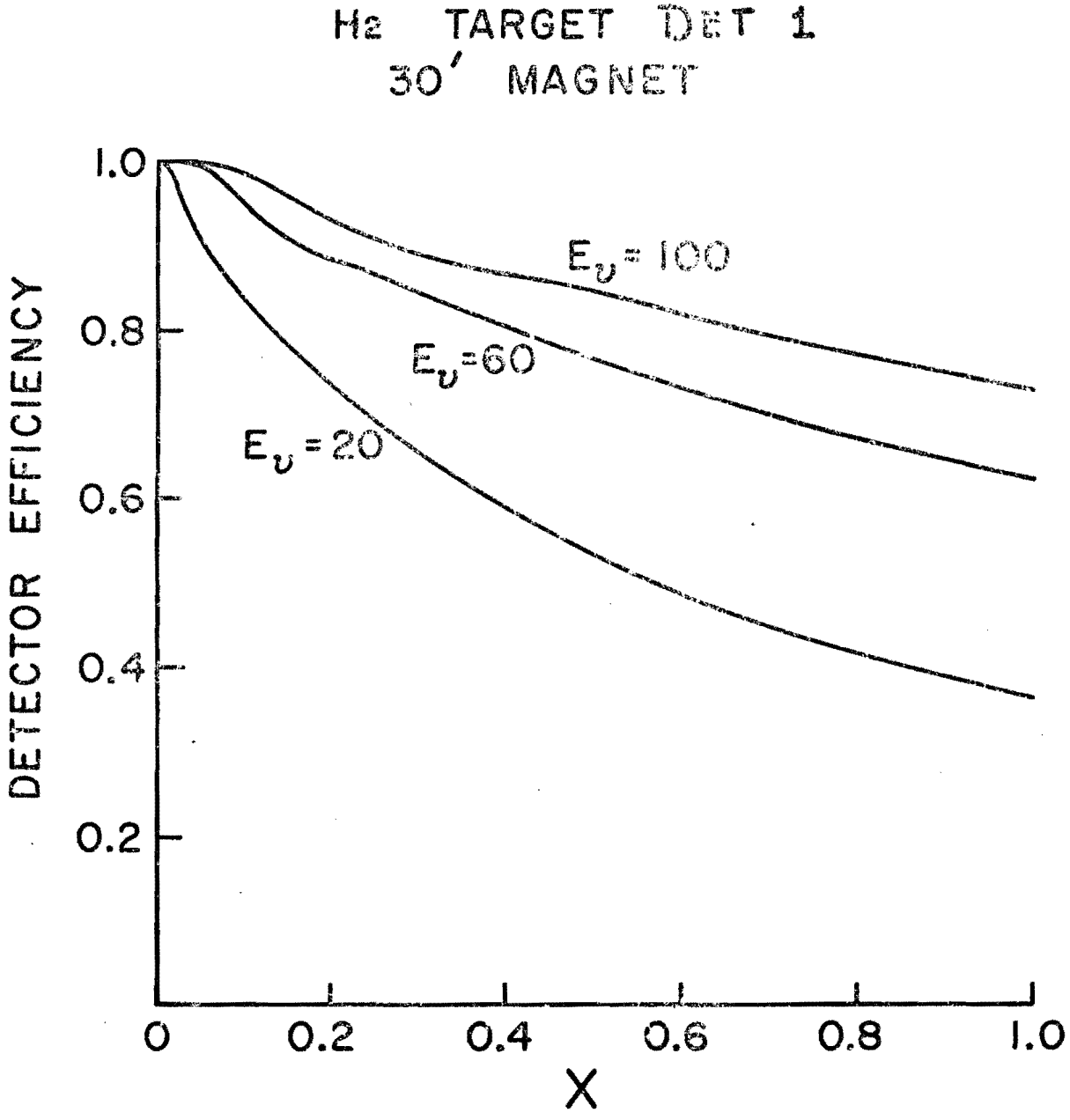
H2 TARGET DET 1
30' MAGNET
DETECTOR EFFICIENCY
1.0
0.8
0.6
0.4
0.2
0
0.2
0.4
0.6
0.8
1.0
X
E_ν = 100
E_ν = 60
E_ν = 20

FIG 27b

Appendix 1

1. The Set-Up.

The new muon spectrometer is shown in Fig. 1. It consists of the old magnet spectrometer and of three additional large blocks of magnetized steel to extend the detection efficiency to the very large angles. The additional blocks are a 1.25 m thick cylindrical unit of 6 m diameter and of two toruses of 9 m outer diameter, each one $\sim$ 65 cm thick. The 3×3 m^2 centered hole of the toruses houses the last sections of the high density calorimeter. Drift chambers and scintillation counters have been added in order to determine the direction and the momentum of the muon and to trigger on a rather forward going muon (quasi-elastic events), for which an effective energy trigger may be impossible because of the relatively small energy depositions.

2. Why Drift Chambers?

The detectors to determine muon trajectories around the spectrometer must be capable of determining with precision $\sigma \leq 0.5$ mm the location of the tracks. Because of the huge size of the spectrometer this is equivalent to a resolution of 1/20000 along each of the chamber coordinates. The large mass, the large area and the high neutrino fluxes are such that usually more than one neutrino event can occur at each short machine burst. Therefore, an excellent time resolution and a fast recovery are also necessary.

We have developed a type of drift chamber capable of meeting all of these stringent requirements. The initial idea of a drift chamber is due to G. Charpak et al[1]: The point of impact of an ionizing particle can be located very precisely by measuring the time of flight of the ionization electrons to the collecting wire of a proportional counter. Practical applications of this fundamental idea have been made by Walente et al[2] and Chaminade et al[3].

In the present application, because of their low cost per unit area, the higher spatial resolution and the absence of electrostatic instabilities, this type of chambers competes very favorably with multi-wire proportional chambers.

We have so far constructed and operated 24 planes (DCH1-5 and DCH9) For details we refer to reference 4. On the basis of the experience we have achieved, we are confident that the further extrapolation of a factor 1.5 in the maximum dimensions required in the proposed set-up it is within our possibilities.

3f.-Main Design Criteria for the Large Area Chambers DCH1-5 and DCH9

To meet the large size requirement we have built drift chamber modules in the form of a square frame (3.6 m x 3.6 m, 5 cm thick) with 1 mm metallic sheets on both sides (fig. 2A). This gives sufficient mechanical support while providing dimensions whose tolerances can be easily maintained.

To obtain good drift time linearity, we employ a drift wire with a repulsive field to eliminate low fields far from the sense wire (cross section shown in Fig. 3) and use a velocity saturated gas to overcome the divergences near the sense and drift wires. Simplicity and economy call for as few sense wires as possible. On the other hand, the wire spacing cannot be too large, without the electric field midway between wires becoming too small. For a gap spacing of 5 cm, electric field studies suggest a cell 10 cm wide. The resulting 5 cm drift region implies a maximum dirft time of $\sim$2 μsec for C_2H_4, well within our rate requirements. This cell size leads to a plane with only 34 sense wires over the full 3.6 m span.

In choosing sense wire diameter, construction simplicity favors wires suspended only at their ends (i.e., a 3.6 m long span) and large diameter wires which are easily handled. A 3.6 m long wire with 100 μ diameter sags <0.2 mm when stretched horizontally by 150 g of tension. As calculated above, electrostatic stability for a gap spacing at 5 cm is good for wire lengths up to ~12 m with 6KV operating voltage. Light, economical construction of the box requires low total tension on the frame. In the above system, the total force on the frame. In the above system, the total force on the frame is 10 kg for 70 drift and sense wires.

The module consists of three basic components:

i) There is a square welded frome of U-profile aluminum channel, reinforced by two I-beams (fig. 2). Large holes spaced at 5 cm in two opposite sides of the frame allow insulated passage of drift and sense wires to the outside (fig. 4).

ii) A plexiglas insulator is epoxied to the inside of this frame (fig. 4) A thin tube feeds through a teflon bushing to anchor the wire and suppress corona.

iii) Aluminum sheets are epoxied to the frame, epoxied to the frame enclosing the gas and shielding the wires as well as providing the ground planes.

At one end of the wires, the U-channel serves as a shielded location for the preamplifiers attached to the sense wires. In the opposite channel, an epoxy cast of two bars (one for drift and one for sense wires) busses around the high voltage.

Since no electrostatic instability problem exists, the only critical precautions in the above construction are those taken to avoid corona. Before closing each chamber, all wires are raised to +10 kV and examined for discharge.

Four of these elementary chambers are sandwiched into what we call a supermodule. The super-module consists of a pair of two-module systems sandwiched so that wires run in an x-y-x-y sequence. Parallel sense wires in different planes are staggered with respect to each other by half a cell width (fig. 2B). Measurement of four independent drift times for this super-module yields four independent variables. A measure of the traversal time t, from scintillator information, provides a fifth independent variable. This is sufficient to remove left-right

ambiguities and to measure x, y, θ_x, θ_y and the time of traversal of the particle across the chamber.

4. Results of the Tests with Cosmic Rays

We have been operating a stack of 16 planes during the last several months. The enormous size of these chambers simplifies calibration, because cosmic-ray rates are high enough to make them useful as test particles. Scintillation counters located above and below the chamber define the time of passage of the particle.

The results of these tests indicate that the chambers operate reliably, with good efficiency and acceptable spatial resolution over periods of several weeks. We show in Figs. 5, 6, and 7 some of the typical distributions.

5. General Organization of the Read-Out Electronics.

Drift chamber read-out electronics consists of two sections. The first section is the amplifier, delay and strobe typical of MWPC systems. The second section digtizes and reconds the time of the pulse. Since we have to detect a relatively low density of particles, we record only one drift time at each event. Furthermore, we expect to have at most 2-3 event triggers per beam burst. As the bursts are short (~200μsec), and the time between bursts is large (4-12 sec), we wish to store rapidly the data from several events during the burst, and then read them out to the computer between bursts.

The selected design is shown in figg. 8-9. Drift times are measured to an accuracy of 3 nsec rms. This design has the capacity to record up to one drift time per wire per event and up to six events before read-out to the computer. By using a time expander[5] we are able to reduce the counting frequency in the time digitizer stage to 20 MHz, where standard TTL circuitry is available.

The recovery time between events is $\lesssim$25 μS.

6. Design criteria for DCH8, DCH10-14

The chambers DCH8, DCH10-14 cover very large angles from the target (Fig. 10). The density of particles is sufficiently low as to permit to relax somewhat on the requirement of resolving time of the chambers. As long as a resolving time of ~1μs is acceptable, we can re-

duce to two the number of planes (1x,1y) of each supermodule. The geometry of the basic cell has to be modified slightly in order to be able to resolve the left-right ambiguities. The method, used successfully by us and others[2][3] consists of doubling the sense wires, as shown in Figs 11 and 12.

7. Summary of Parameters AI

We summarize in tables [redacted] all relevant parameters of the detectors for the muon spectrometer.

TABLE A I

LIST OF DRIFT CHAMBERS

Chamber Module	Size	No. Wires/Plane	No. Plane/Module	Remarks
DCH1	4 x 4 m^2	32	2x, 2y	Existing + Tested
DCH2	4 x 4 m^2	32	2x, 2y	Existing + Tested
DCH3	4 x 4 m^2	32	2x, 2y	Existing + Tested
DCH4	4 x 4 m^2	32	2x, 2y	Existing + Tested
DCH5	4 x 4 m^2	32	2x, 2y	Existing + Tested
DCH6	6 x 6 m^2	48	2x, 2y	New
DCH7	6 x 6 m^2	48	2x, 2y	New
DCH8	4 x 4 m^2	32	2x, 2y	Existing + Tested
DCH9	4 x (3 x 6m^2)	$\begin{cases}24\\48\end{cases}$	$\begin{cases}1x\\1y\end{cases}$	New
DCH10	4 x (3 x 6m^2)	$\begin{cases}24\\48\end{cases}$	$\begin{cases}1x\\1y\end{cases}$	New
DCH11	4 x (3 x 6m^2)	$\begin{cases}24\\48\end{cases}$	$\begin{cases}1x\\1y\end{cases}$	New
DCH12	4 x (3 x 6m^2)	$\begin{cases}24\\48\end{cases}$	$\begin{cases}1x\\1y\end{cases}$	New
DCH13	4 x (3 x 6m^2)	$\begin{cases}24\\48\end{cases}$	$\begin{cases}1x\\1y\end{cases}$	New
DCH14	4 x (3 x 6m^2)	$\begin{cases}24\\48\end{cases}$	$\begin{cases}1x\\1y\end{cases}$	New

Total No. of wires already available and tested = 768 (3.07 Kilometers)
Total No. of new wires required = 2112 (10.1 Kilometers)

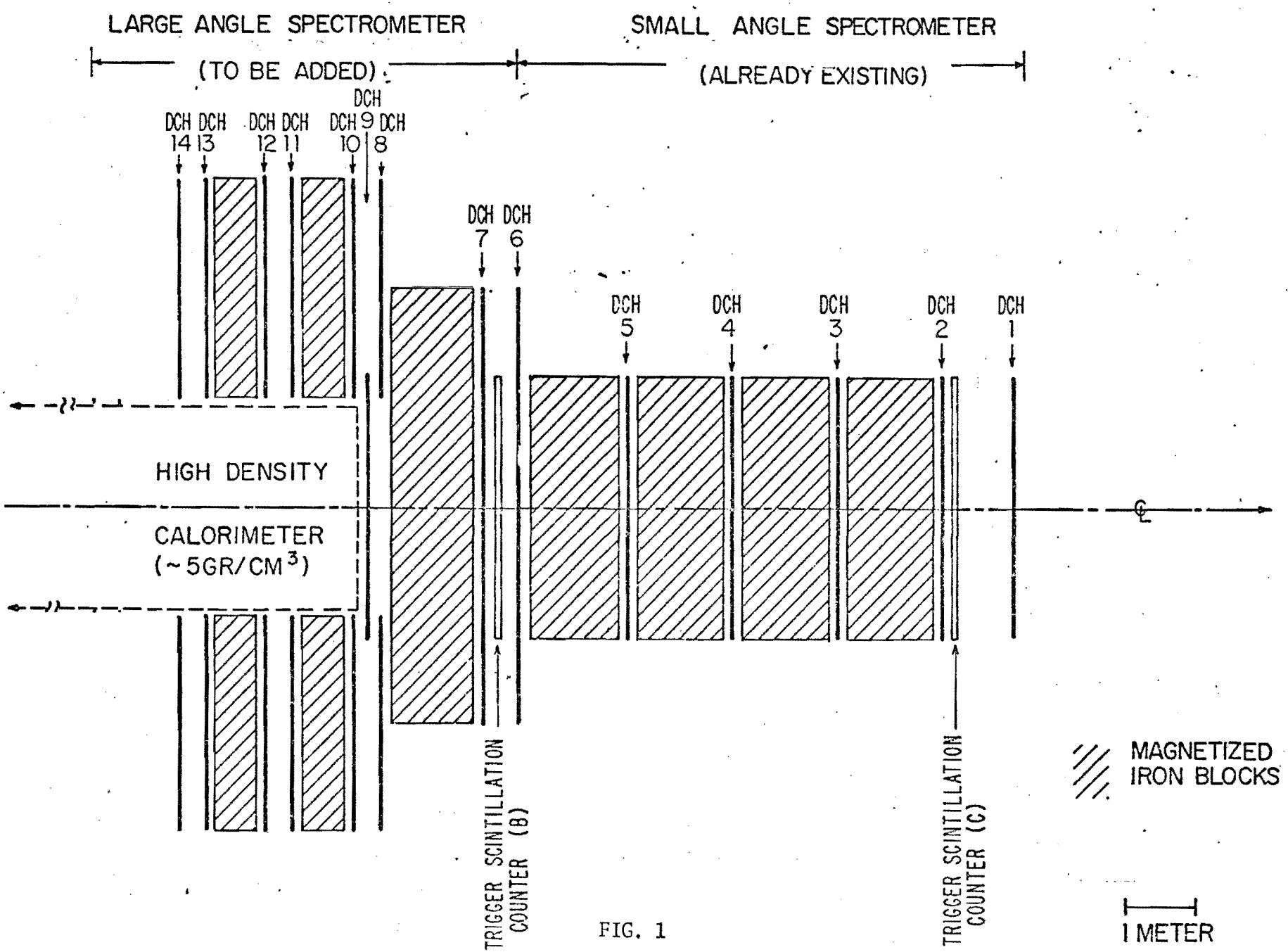
LARGE ANGLE SPECTROMETER
(TO BE ADDED)
SMALL ANGLE SPECTROMETER
(ALREADY EXISTING)
DCH 14
DCH 13
DCH 12
DCH 11
DCH 10
DCH 9
DCH 8
DCH 7
DCH 6
DCH 5
DCH 4
DCH 3
DCH 2
DCH 1
HIGH DENSITY
CALORIMETER
(~5GR/CM3)
TRIGGER SCINTILLATION COUNTER (B)
TRIGGER SCINTILLATION COUNTER (C)
MAGNETIZED IRON BLOCKS
1 METER

FIG. 1

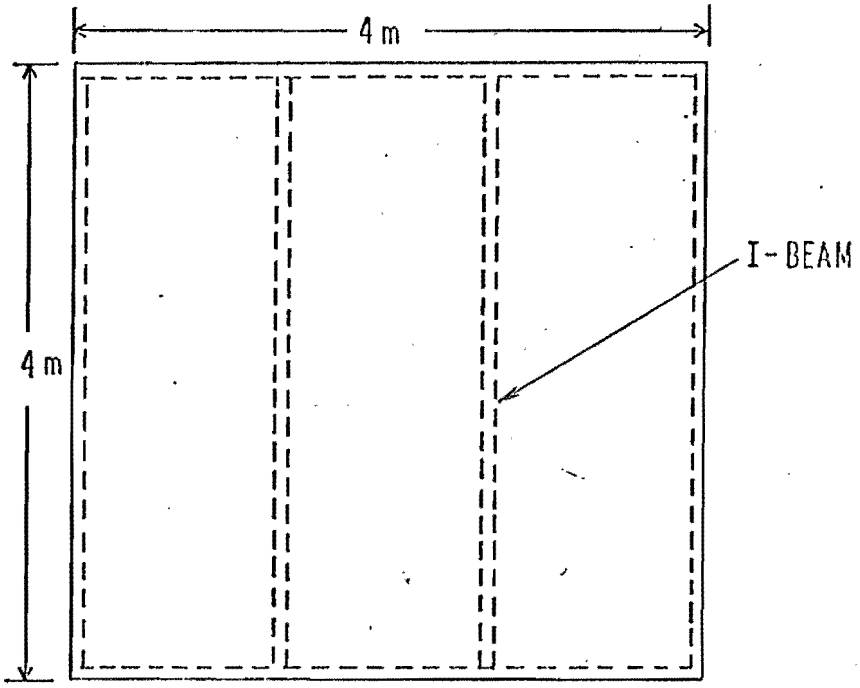
4 m
4 m
I-BEAM

(a)

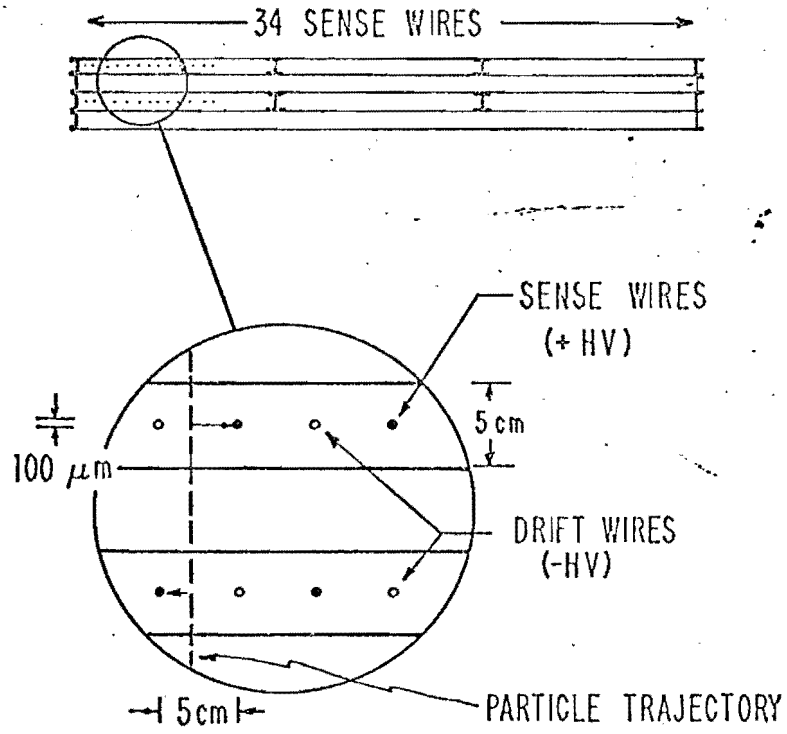
34 SENSE WIRES
SENSE WIRES
(+ HV)
5 cm
100 μm
DRIFT WIRES
(-HV)
5 cm
PARTICLE TRAJECTORY

(b)

FIG. 2

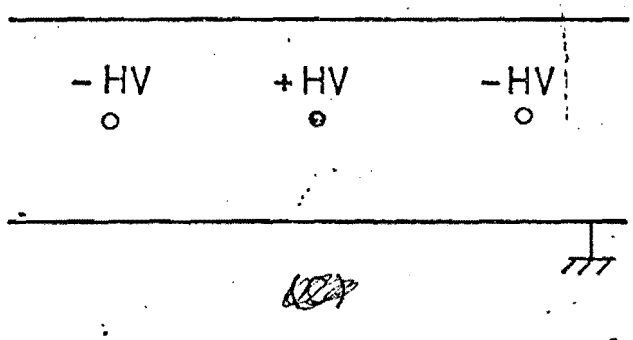

FIG. 3

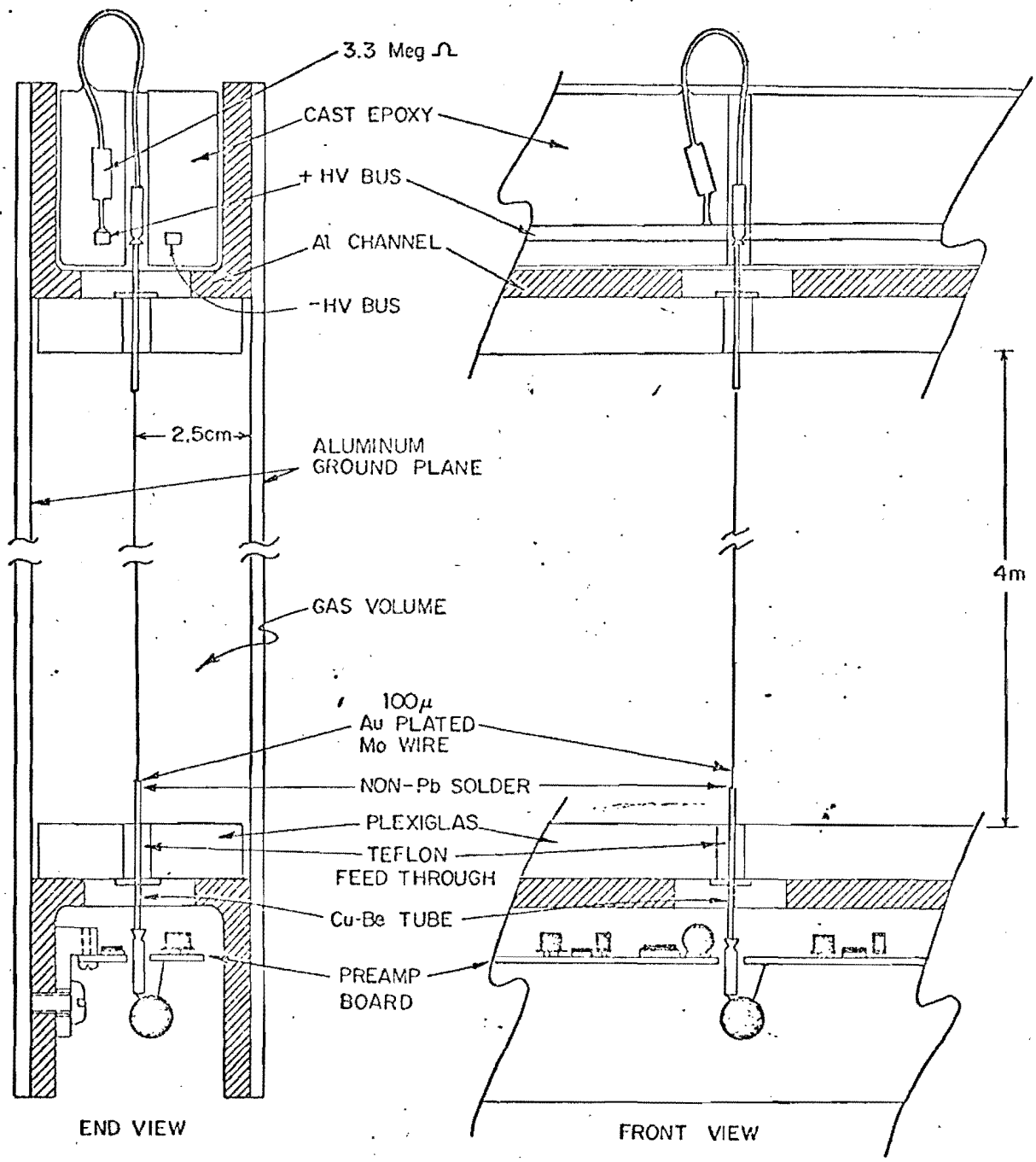
3.3 Meg Ω
CAST EPOXY
+ HV BUS
Al CHANNEL
-HV BUS
2.5cm
ALUMINUM
GROUND PLANE
4m
GAS VOLUME
100μ
Au PLATED
Mo WIRE
NON-Pb SOLDER
PLEXIGLAS
TEFLON
FEED THROUGH
Cu-Be TUBE
PREAMP
BOARD
END VIEW
FRONT VIEW

FIG. 4

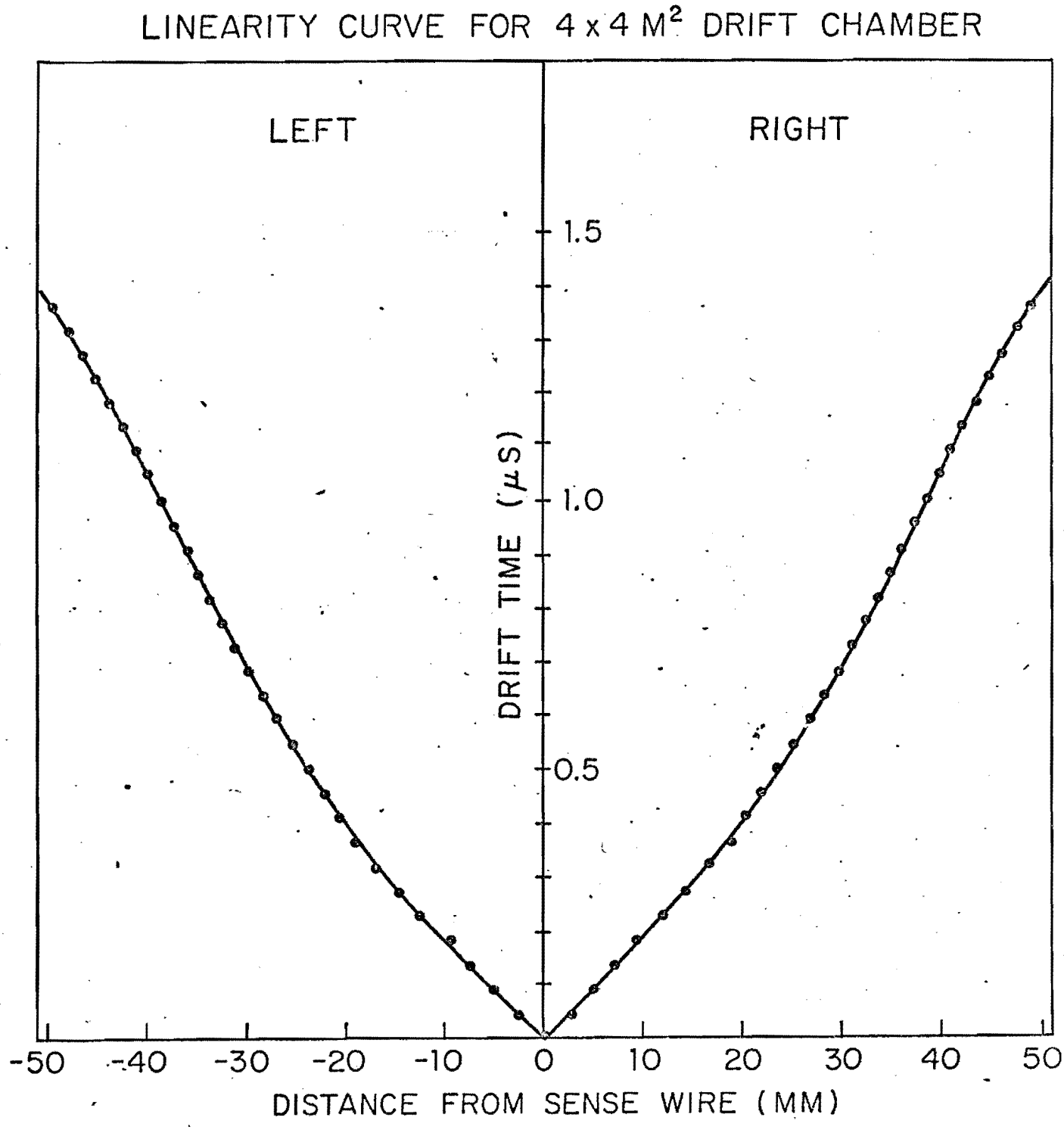
LINEARITY CURVE FOR 4 x 4 M² DRIFT CHAMBER
LEFT
RIGHT
1.5
1.0
0.5
DRIFT TIME (μS)
-50
-40
-30
-20
-10
0
10
20
30
40
50
DISTANCE FROM SENSE WIRE (MM)

FIG. 5

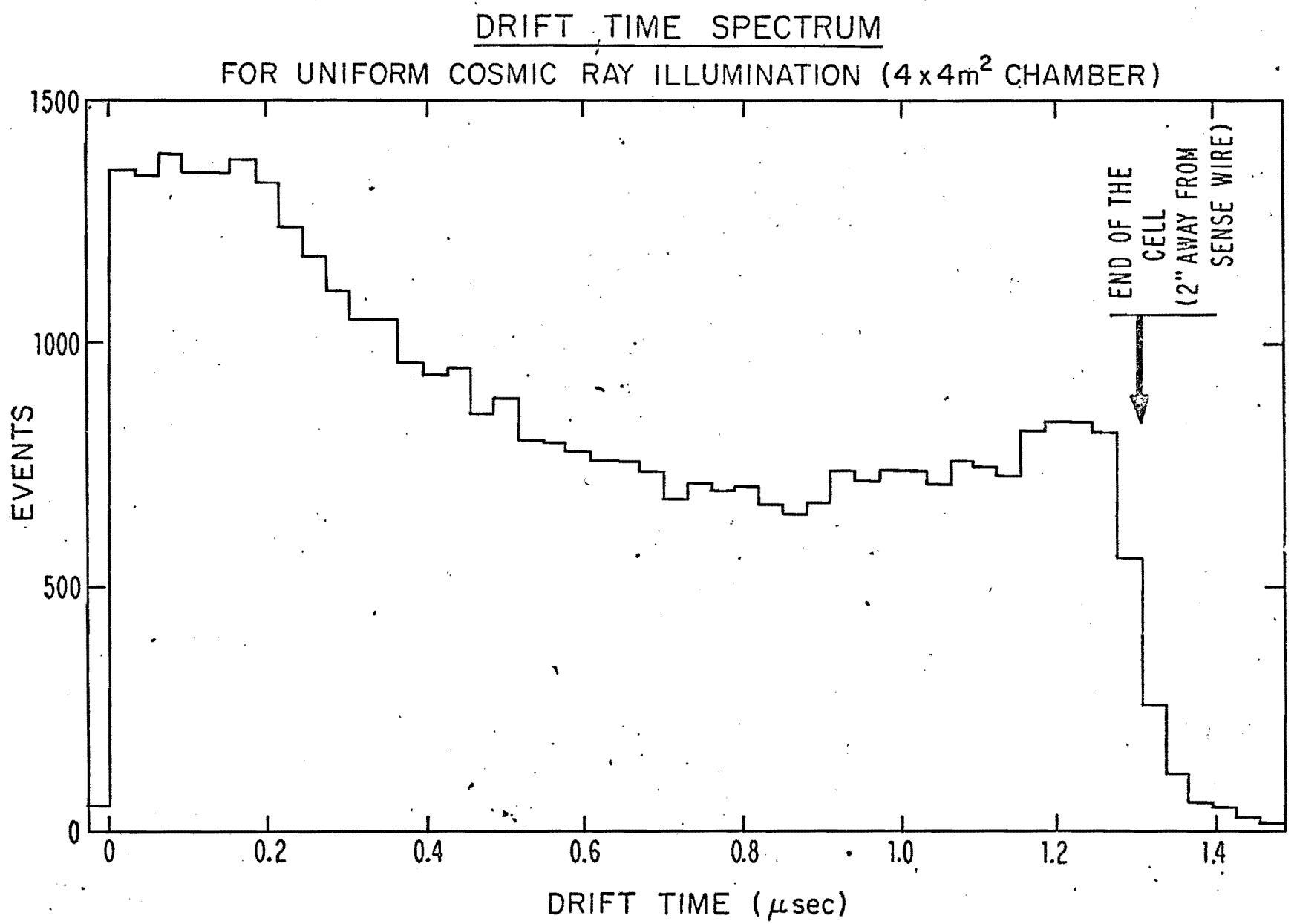
DRIFT TIME SPECTRUM
FOR UNIFORM COSMIC RAY ILLUMINATION (4x4m² CHAMBER)
1500
1000
500
0
EVENTS
0
0.2
0.4
0.6
0.8
1.0
1.2
1.4
DRIFT TIME (μsec)
END OF THE CELL (2" AWAY FROM SENSE WIRE)

FIG. 6

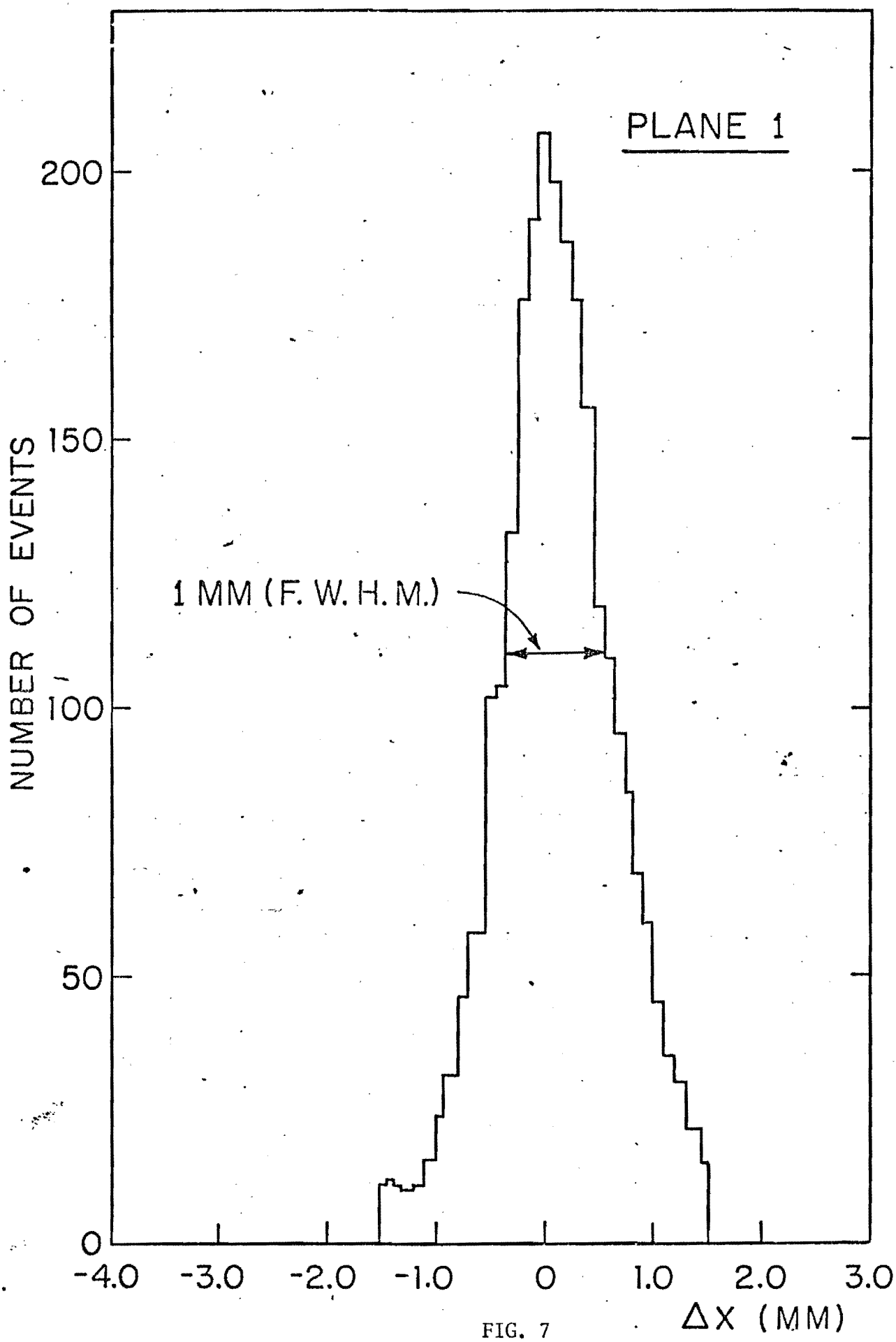
4 x 4 M² DRIFT CHAMBER-MEASURED DEVIATION FROM
STRAIGHT LINE FOR COSMIC RAYS INCIDENT AT ALL ANGLES
PLANE 1
1 MM (F. W. H. M.)
NUMBER OF EVENTS
0
50
100
150
200
-4.0
-3.0
-2.0
-1.0
0
1.0
2.0
3.0
ΔX (MM)

FIG. 7

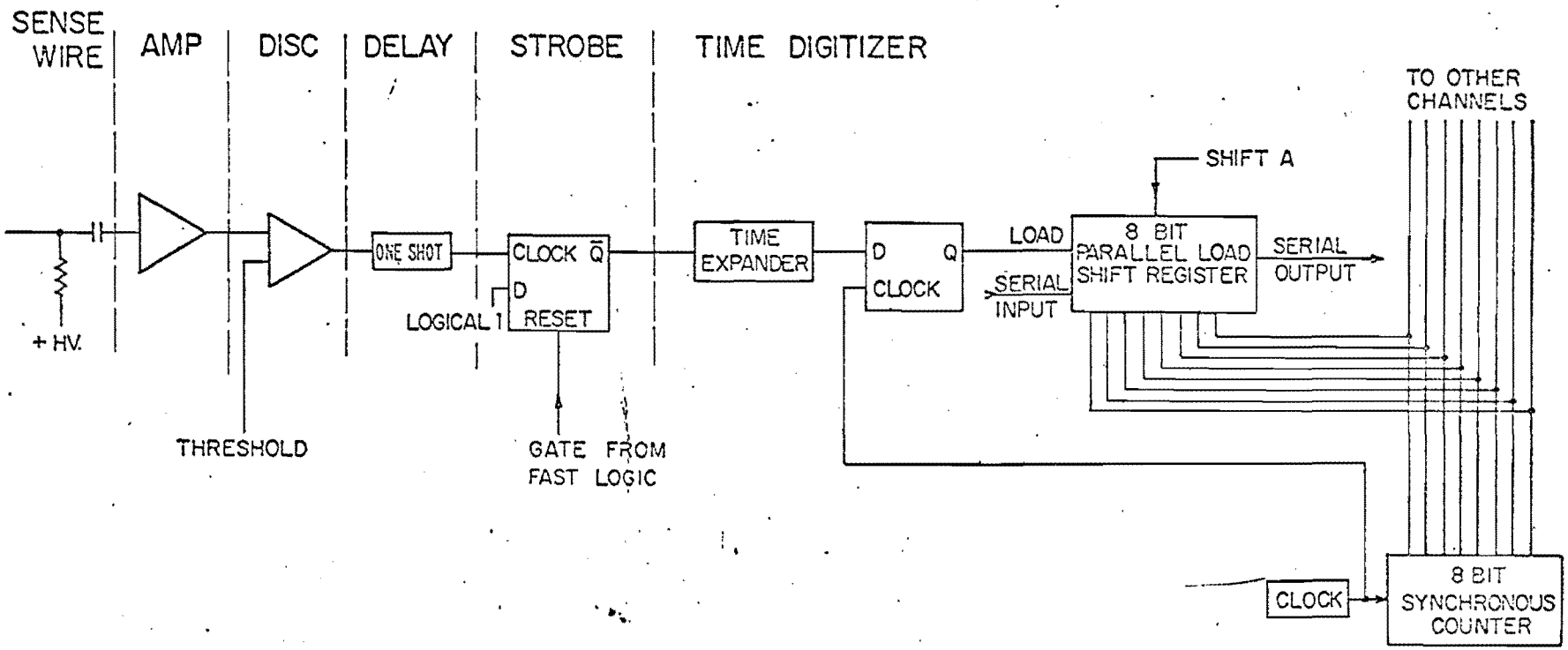
SENSE WIRE
AMP
DISC
DELAY
STROBE
TIME DIGITIZER
TO OTHER CHANNELS
SHIFT A
+ HV.
ONE SHOT
CLOCK Q̄
D
RESET
LOGICAL 1
TIME EXPANDER
D Q
CLOCK
LOAD
SERIAL INPUT
8 BIT PARALLEL LOAD SHIFT REGISTER
SERIAL OUTPUT
THRESHOLD
GATE FROM FAST LOGIC
CLOCK
8 BIT SYNCHRONOUS COUNTER

FIG. 8

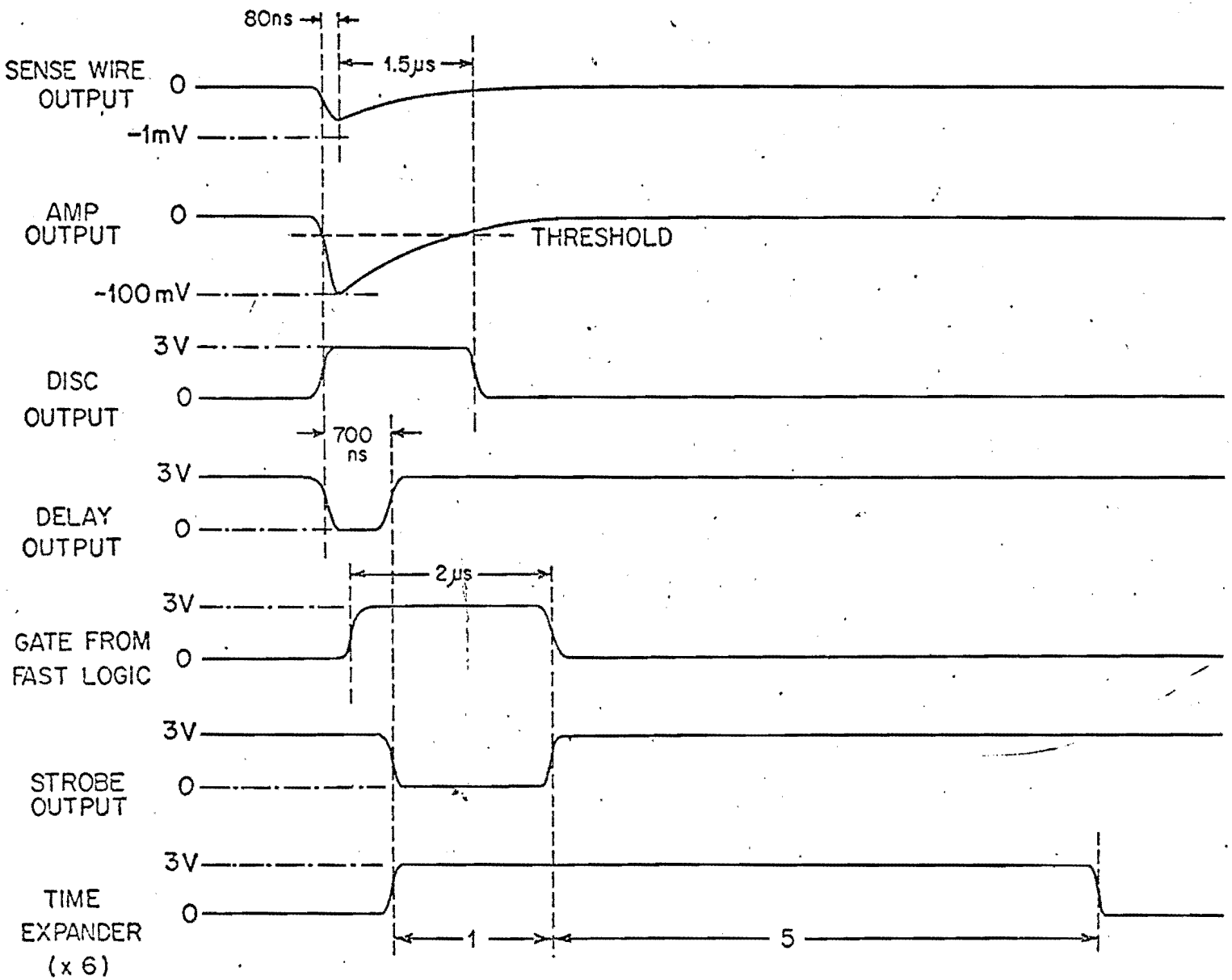
80ns
1.5μs
SENSE WIRE OUTPUT
0
-1mV
AMP OUTPUT
0
THRESHOLD
-100mV
3V
DISC OUTPUT
0
700 ns
3V
DELAY OUTPUT
0
2μs
3V
GATE FROM FAST LOGIC
0
3V
STROBE OUTPUT
0
3V
TIME EXPANDER (x 6)
0
1
5

FIG. 9

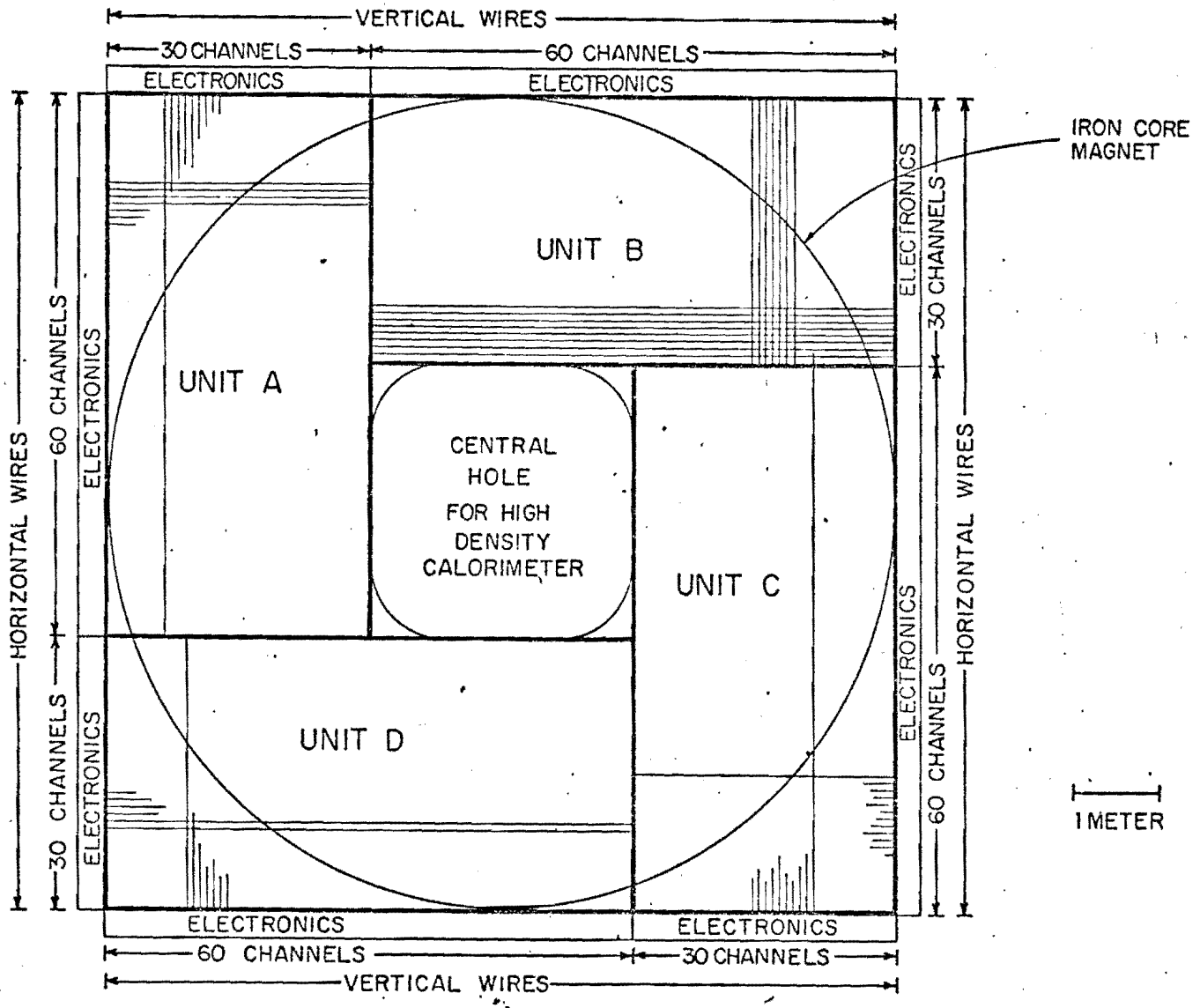
VERTICAL WIRES
30 CHANNELS
60 CHANNELS
ELECTRONICS
ELECTRONICS
IRON CORE MAGNET
UNIT B
UNIT A
CENTRAL HOLE FOR HIGH DENSITY CALORIMETER
UNIT C
UNIT D
HORIZONTAL WIRES
60 CHANNELS
30 CHANNELS
ELECTRONICS
ELECTRONICS
ELECTRONICS
ELECTRONICS
30 CHANNELS
60 CHANNELS
HORIZONTAL WIRES
1 METER
ELECTRONICS
ELECTRONICS
60 CHANNELS
30 CHANNELS
VERTICAL WIRES

FIG. 10

GOMETRY OF THE ELEMENTARY
CELL OF THE DRIFT CHAMBERS DCH 9-14

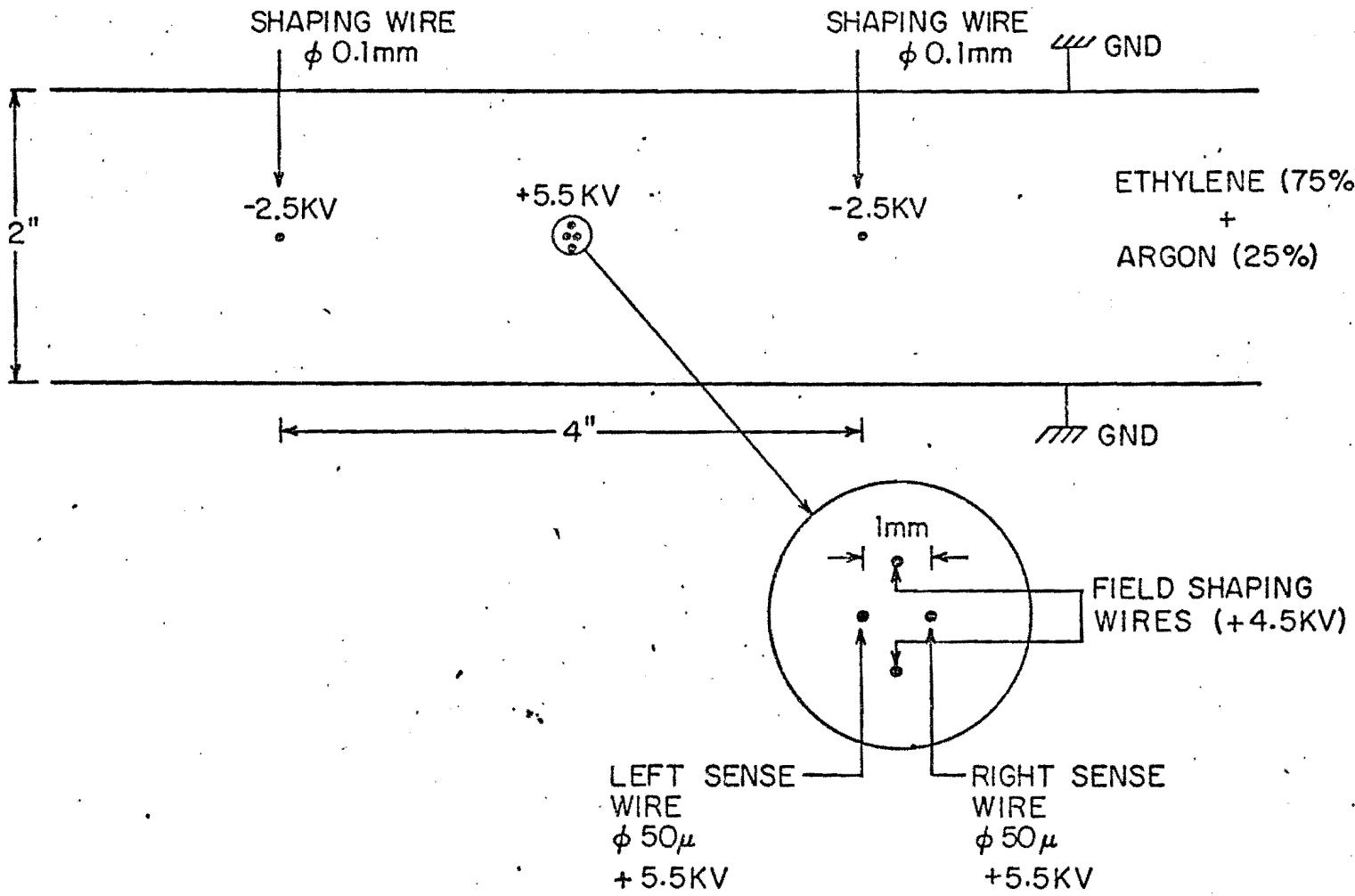

FIG. 11

PRINCIPLE OF RESOLVING LEFT/RIGHT AMBIGUITIES OF DRIFT CHAMBERS WITH DOUBLE SENSE WIRES

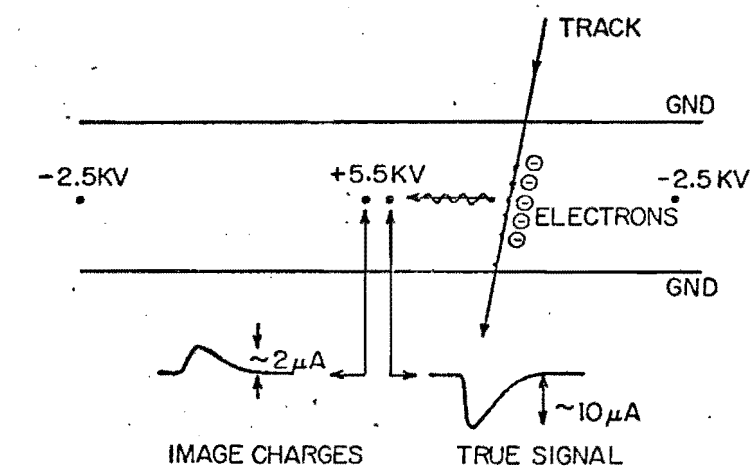

RIGHT

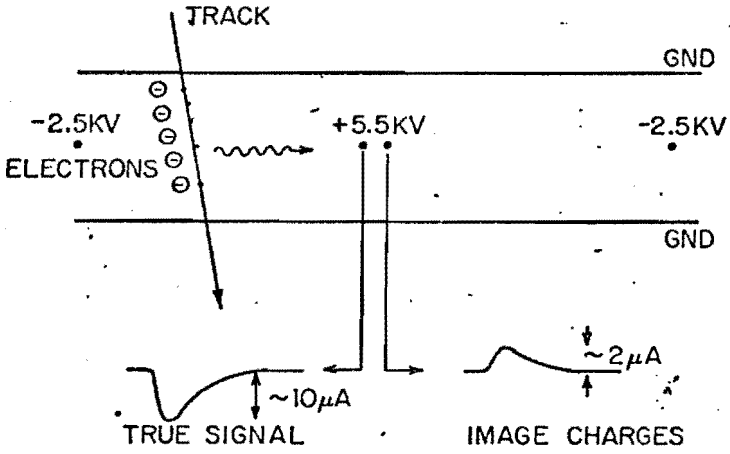

LEFT

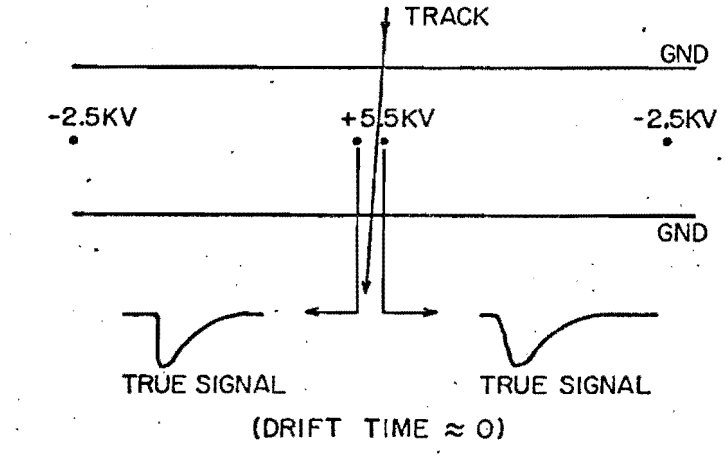

CENTER

FIG. 12

APPENDIX II

A DETAILED DISCUSSION OF THE TARGET CALORIMETER TO DETERMINE BOTH ENERGY AND DIRECTION OF THE HADRONIC JET (THE ENERGY FLOW DEVICE)

1. Introduction - In our original proposal for the experiment 1A (1971) we put forward the idea of a massive neutrino target which is at the same time an energy sampling device (calorimeter). The target of a neutrino experiment must be very massive and therefore it automatically contains the greater fraction of the hadronic and electromagnetic cascades produced by the events. It appeared very natural at that time to propose to determine the energy transferred by the incident neutrinos into hadrons, E_h, by a measurement of the total amount of ionization produced inside the target detector. In some cases, whenever the number of particles produced by the cascade is very large, it may be sufficient to sample the ionization with a sandwich arrangement of metal plates and (liquid) scintillators, providing of course that the number of samplings is large. We called such a device a fine grain calorimeter. However for elastic or quasi-elastic events, where E_h is relatively small, the sampling cannot be done with sufficient accuracy and a pure liquid scintillation counter, a true total absorption detector, is vastly superior. Electronic neutrino experiments with calorimeter-target detectors have turned out to be considerably more powerful than the earlier spark chamber "visual type" devices used at BNL and CERN. Several recently published results have shown that they can be very competitive, and in some instances even superior to a large heavy liquid bubble chamber (CERN Gargamelle).

In the course of the last three years the technology of calorimeters has made very considerable progress. Many different types of sampling calorimeters have been constructed by several groups[1] and extensive theoretical work based on Monte Carlo calculations[2] has become available. The calculation approach gives good agreement with experimental data and in general it is now possible to predict reasonably well both the energy deposition and the energy-deposition fluctuations in this type of counter. In parallel, considerable progress has been made in the technology of constructing such counters. The sampling devices, initially plastic scintillators, have been replaced with liquid scintillators which have (i) very much lower cost, (ii) a much lower light attenuation and (iii) much more uniform light yield. In analogy with the principle of fiber-glass optics, the light collection from very large stacks of liquid scintillators and metal plates can be performed by coating the plates with a very thin (< 1 mil) layer of plastic material with a refractive index appreciably lower than that of the liquid (1.33 vs 1.50). Light travels inside the gaps between metal plates by total internal reflections.[3] At the same time, coating the plates with an inert, plastic material solves the problem of conditioning the huge total amount of metal surface exposed to the liquid scintillator.

On the basis of the progress achieved so far, we believe that the amount of information potentially available from fine grain calorimeter devices can be made considerably more complete than a simple number i.e. the total energy deposition, of course provided that the devices are built in order to extract it. We propose a type of device which can (i) separately determine the energies of the electromagnetic and hadronic components and (ii) determine the

direction of the resultant of the momenta of interacting particles emitted in the neutrino induced interaction. We call this an energy flow device. In order to achieve these goals the calorimeters must become necessarily more sophisticated than a simple, homogeneous stack. We propose a structure made of alternating sections of low - Z (pure liquid scintillators) with sections of high - Z (sandwiches of lead + liquid scintillator). The configuration is arranged in such a way that most of the hadron interactions occur in the liquid scintillator while the electromagnetic component is almost totally absorbed in one of the high - Z sandwiches (γ-catchers). Localization of the centroid of the energy deposited by ionization in each unit is provided both in the low - Z and high - Z modules by (i) a rough hodoscopic arrangement and (ii) measuring the amount of light collected at both ends of the hodoscopic counters. (The position along the counter is then determined from the ratio of light yields at the two ends.)

We have verified both the basic localization techniques and the feasibility of the energy flow device on a 10 ton fine grain calorimeter exposed to a 17 GeV proton beam.[4] On the basis of these extensive tests, described in detail in the following paragraphs, we conclude that both ideas work very well. We have then used Monte Carlo calculations on the development of nuclear and electromagnetic cascades to extrapolate to the performance of the full scale device.

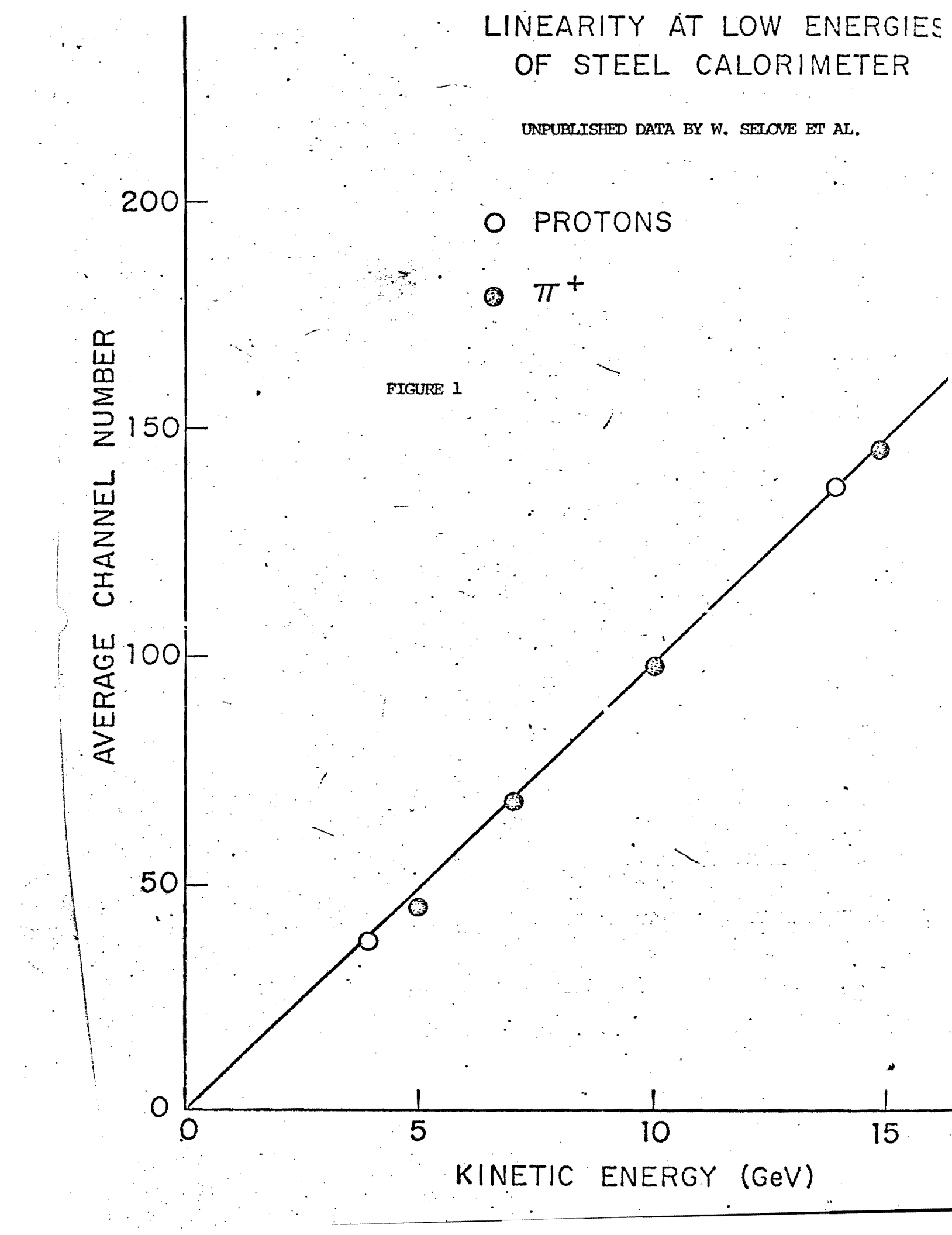
LINEARITY AT LOW ENERGIES
OF STEEL CALORIMETER
UNPUBLISHED DATA BY W. SELOVE ET AL.
PROTONS
π^+
FIGURE 1
AVERAGE CHANNEL NUMBER
200
150
100
50
0
0
5
10
15
KINETIC ENERGY (GeV)

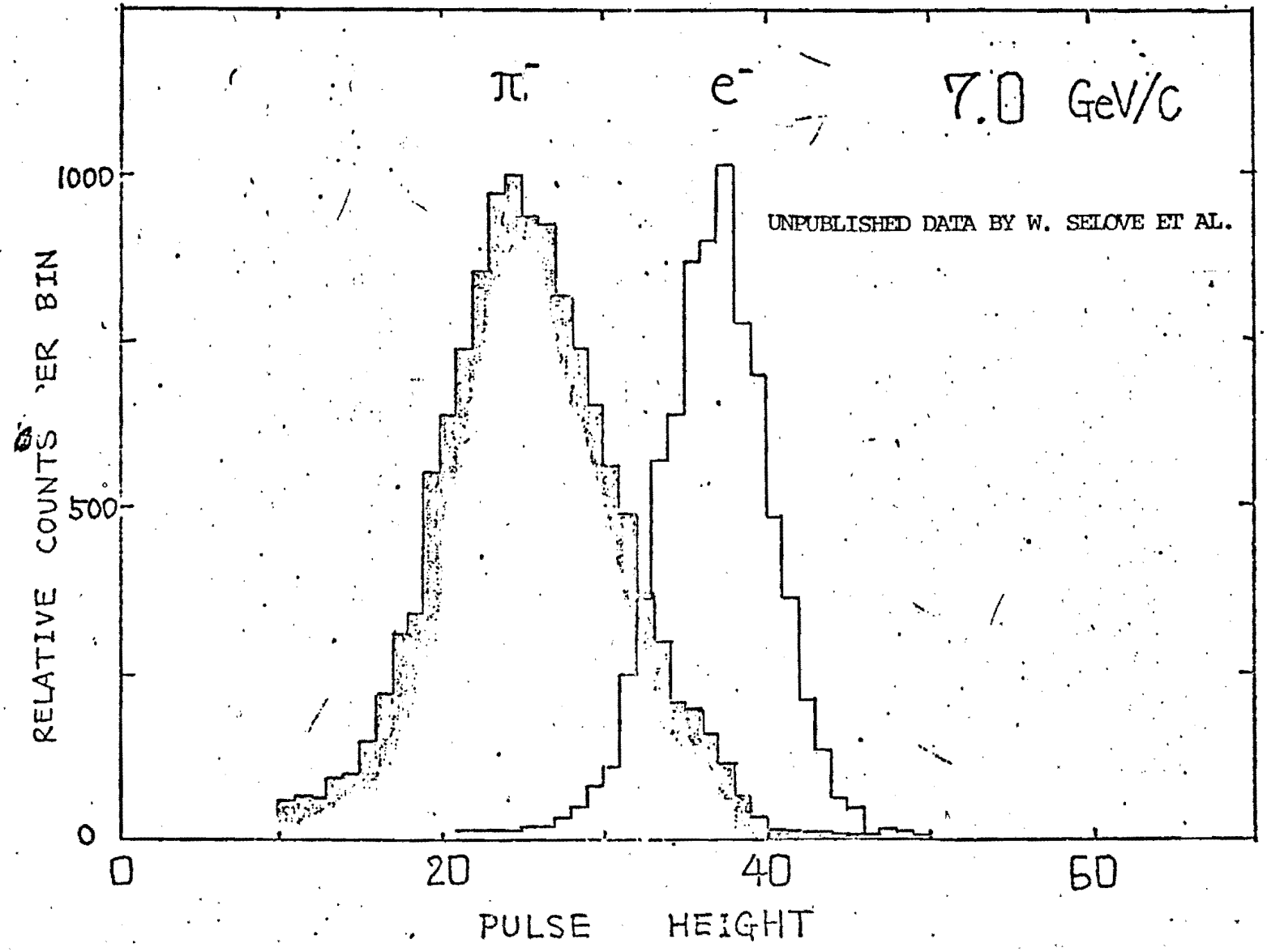
π⁻ e⁻
7.0 GeV/C
UNPUBLISHED DATA BY W. SELOVE ET AL.
RELATIVE COUNTS PER BIN
1000
500
0
0
20
40
60
PULSE HEIGHT

FIGURE 2

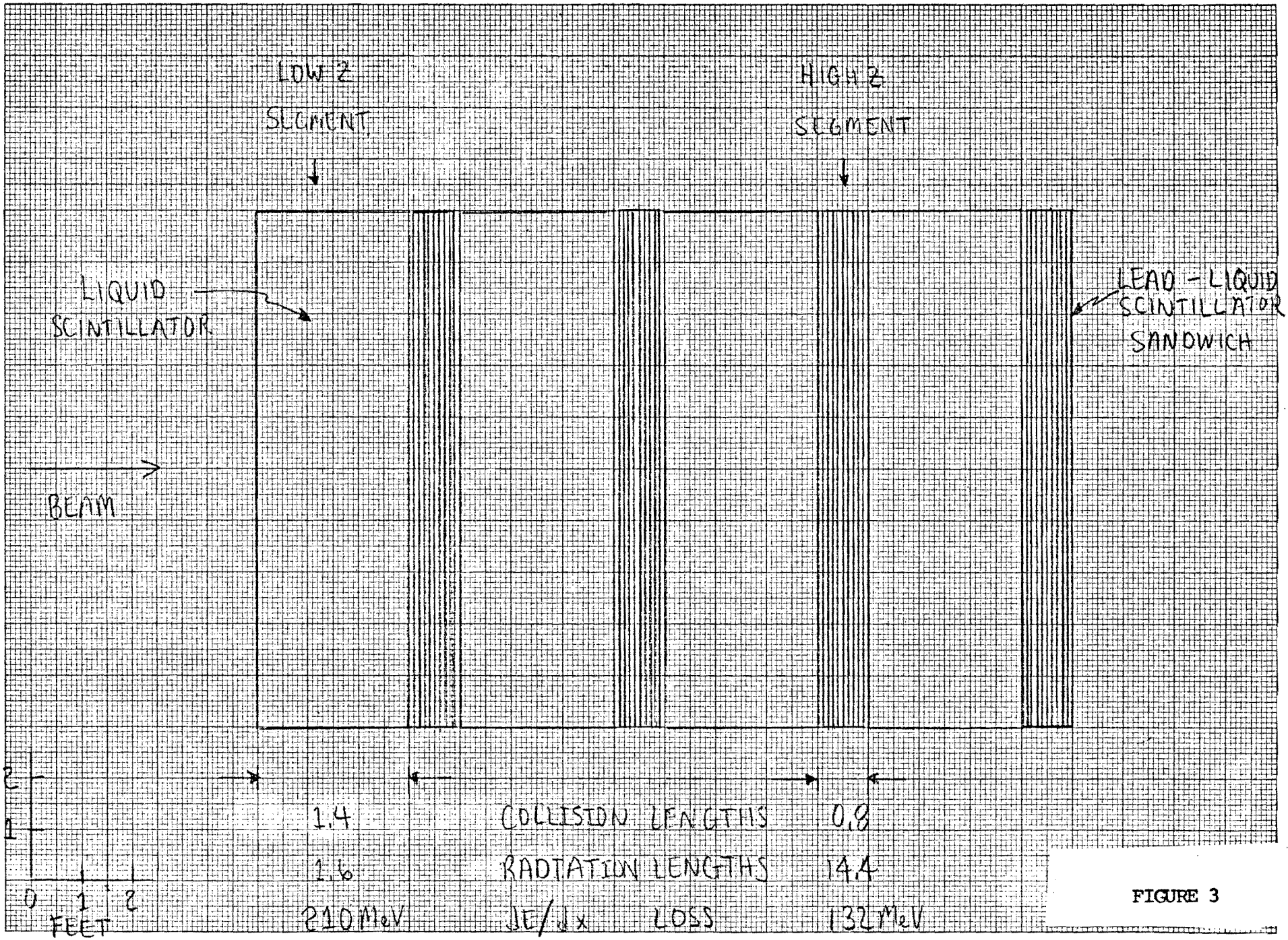

FIGURE 3

2. Separation of the hadronic and electromagnetic cascades. - It has been determined experimentally that calorimeters have a linear light yield response vs. the total incident energy which is not appreciably different for various incident hadronic particles. (Fig. 1) However systematic differences appear when we compare them with the energy calibration for incident electrons (or photons). (Fig. 2) More precisely high energy electrons give on the average of about 30% more total light output than pions or protons of the same (kinetic) energy. The phenomenon is due to two main effects: i) the nuclear cascades associated with incident hadrons dissipate 15 - 20% of the available energy in breaking nuclear bonds which does not produce subsequent ionizing energy. The effect is not present for e.m. cascades. ii) about 10% of the energy dissipation comes from heavy ionizing tracks for which the light yield of the liquid scintillator is heavily saturated. (i.e. the light observed is no longer in direct proportion to the energy deposited). Instead, for electrons and positrons, to a very good approximation, a linear relation holds.

The occurence of this systematic difference is of considerable consequence. The energy response to an initial multiparticle jet produced for instance by a neutrino will vary according to the ratio between π^o's and hadrons. Furthermore, during the development of the hadronic part of the cascade, a substantial fraction of the energy (30 - 50%) will be converted into π^o's and deposited by electromagnetic cascades. Because of these fluctuations, the response of the counter would be subject to substantial variations even for incident hadrons at fixed energy. The low - Z, high - Z alternating structure proposed here (Fig. 3) overcomes these effects since most of the electromagnetic energy is deposited in the γ-catchers (high - Z units). This is seen in Fig. 4 where we display the fractional energy deposited by an electromagnetic cascade as a

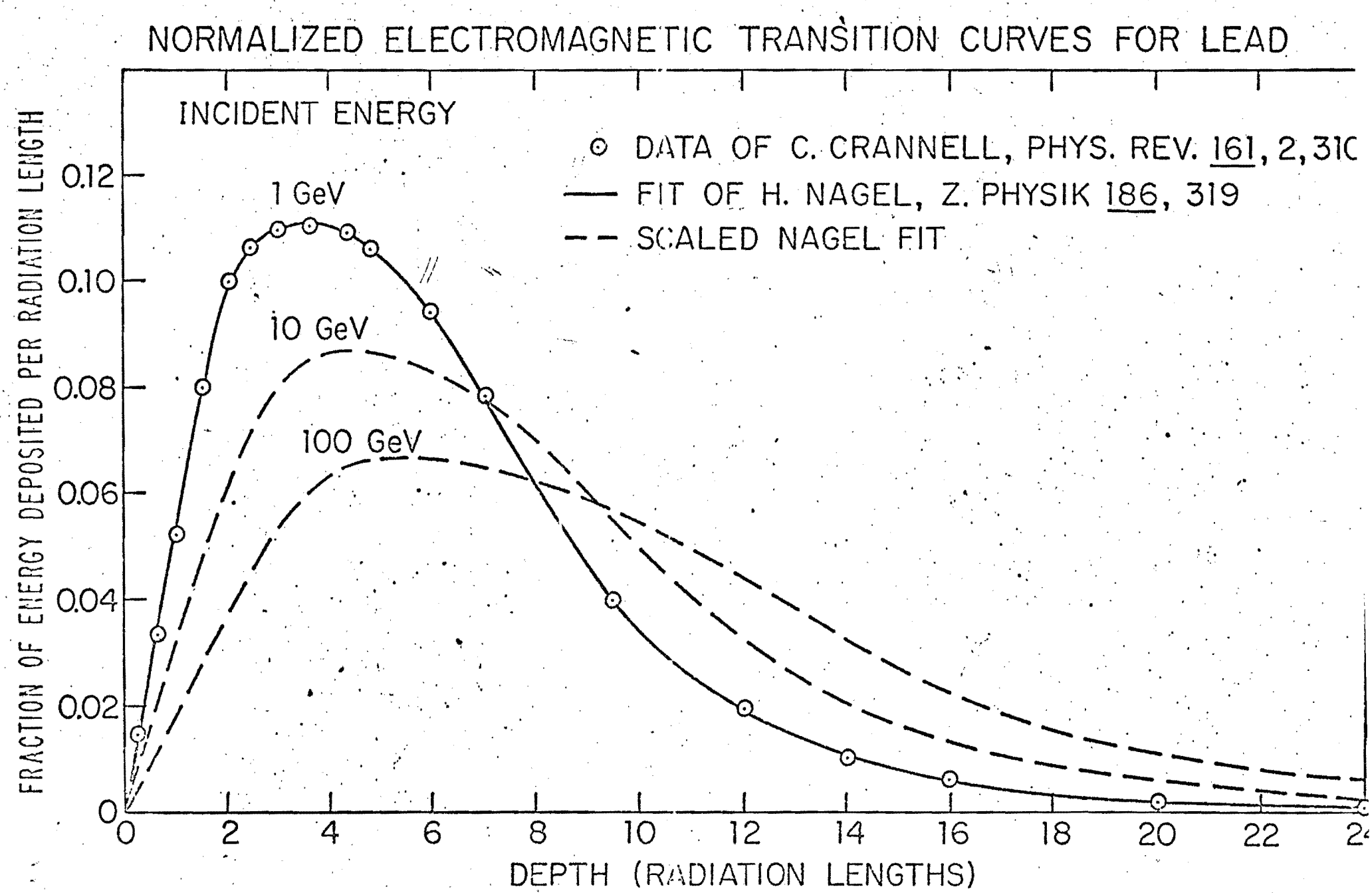
NORMALIZED ELECTROMAGNETIC TRANSITION CURVES FOR LEAD
INCIDENT ENERGY
DATA OF C. CRANNELL, PHYS. REV. 161, 2, 310
FIT OF H. NAGEL, Z. PHYSIK 186, 319
SCALED NAGEL FIT
1 GeV
10 GeV
100 GeV
FRACTION OF ENERGY DEPOSITED PER RADIATION LENGTH
0.12
0.10
0.08
0.06
0.04
0.02
0
0
2
4
6
8
10
12
14
16
18
20
22
DEPTH (RADIATION LENGTHS)

FIGURE 4

function of longitudinal depth. Even in the most unfavorable case of a photon produced at the beginning of a low - Z section, only about 8% of its total energy is dissipated on the average before the first γ-catcher in which almost all of the residual e.m. energy is deposited. Instead, all other forms of energy deposition are primarily concentrated in the low - Z units which have the largest number of nuclear collision lengths and ionization stopping power.

To conclude: We determine directly the total energy of the electromagnetic component of the initial neutrino induced jet from the first γ-catcher immediately following the interaction point. The remaining energy is determined from the sum of the energies deposited in the low - Z units and the corresponding sum in the high - Z units, weighted appropriately in order to correct for the invisible energy fraction of the hadronic cascade.

3. Determination of the spatial coordinates of high energy photons or electrons. - We consider initially the case of a single electromagnetic shower developing in a high-Z unit. Experimental results are avaliable [5] in the case of a lead-scintillator sandwich which is very similar to the high-Z units of the proposed spectrometer. The measurements have been performed with electrons of 32, 20, 5 and 0.7 GeV and a finely subdivided hodoscope at differents depths. The position of a photon or of an electron at the face of the lead scintillator counter can be determined with an accuracy of a few millimeter if the center of gravity of the energy deposition is taken as coordinate:

$$X_0 = \frac{\int \varepsilon(x)\, x\, dx}{\int \varepsilon(x)\, dx}$$

where $\varepsilon(x)$ is the specific energy deposition at the coordinate x.

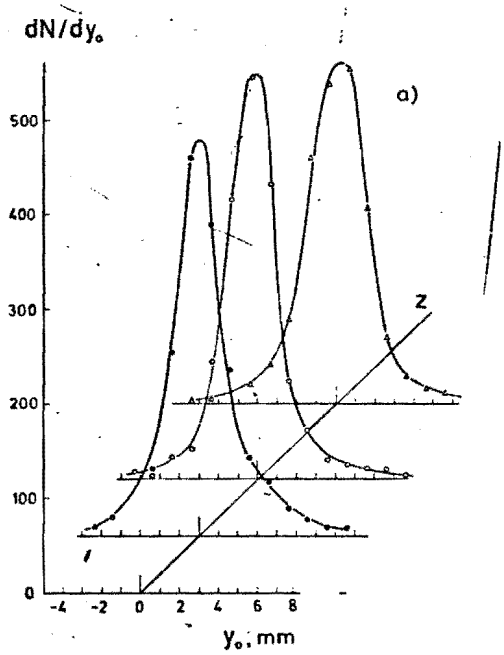

Fig. 2. The distribution dN/dy_0 plotted against the center of gravity of the shower y_0, measured at 32 GeV with the lead sandwich. (●) $t = 1.5$ cm Pb, (○) $t = 3$ cm Pb and (△) $t = 5$ cm Pb.

be-

FIGURE 5

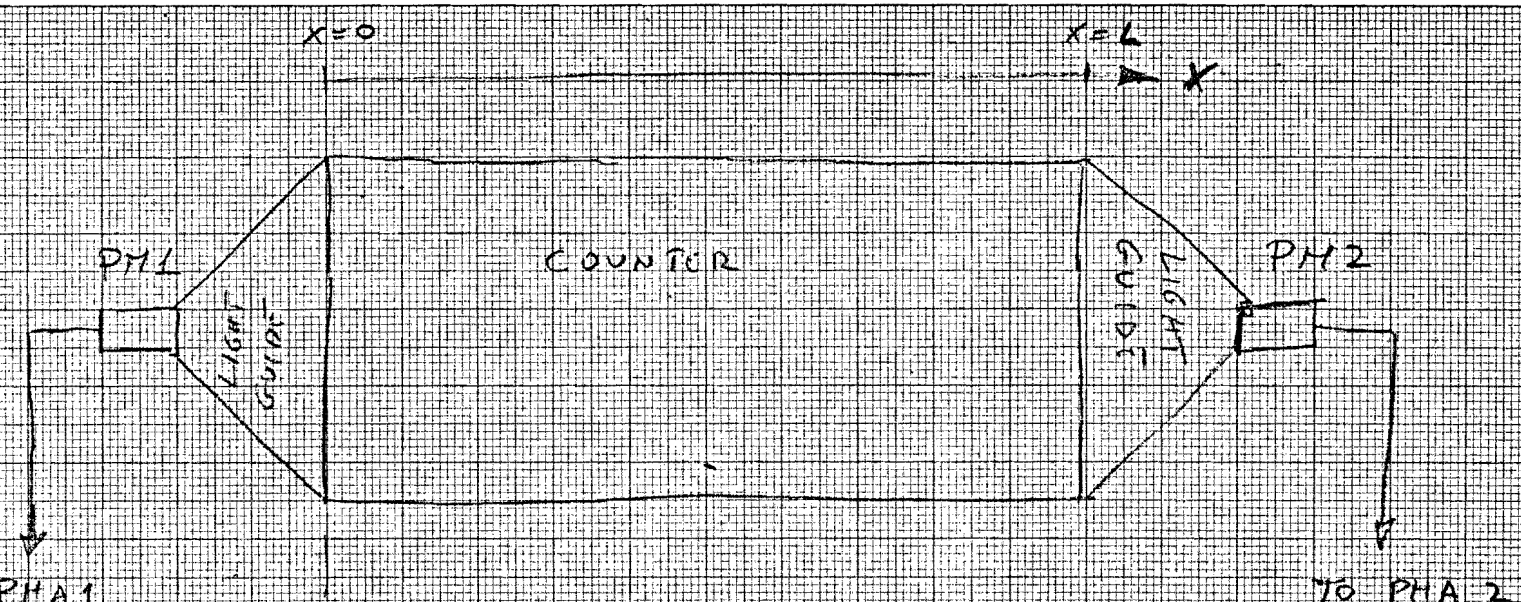

$V_1 \sim A - BX$

$V_2 \sim A - B(L-X)$

FIGURE 6

The intrinsic precision in the determination of X_o is relatively insensitive to the depth at which the measurements are performed (Fig. 5) and to the energy of the initial electron. For instance it varies from $\sigma = 2.8$ mm at E= 32 GeV to $\sigma = 4$ mm for E = 1 GeV.

If the initial neutrino interaction occurs in the low-Z unit and at an appreciable distance from the high-Z unit,we can determine the direction of the photon or electron from the impact point on the high-Z unit and the position of the initial vertex (determined for instance from the spark chamber tracks).

In a broad class of events several photons are simultaneously produced. The center of gravity of the total energy deposition gives directly the direction of the resultant vector momentum, even if individual photon showerscannot be separated :

$$\vec{P} = \sum_i \vec{p}_i$$

4. Determination of the spatial coordinates of hadronic showers . - The corresponding study of the spatial parameters of hadronic showers in a total absorption counter is made very complicated by the greater mass over which it develops and by the large fluctuations of the development of the cascade ,suggesting a simultaneous sampling at several different depths. A set of hodoscope counters of the type used to study the electron or photon induced cascades is not very practical since it would require a prohibitive number of separate elements . We have chosen instead a simpler method in which the center of gravity of the energy depositions is directly measured by an analog technique. It is based on the observation that the light collection in a large counter varies in a good approximation linearly with the distance from the phototube. Let us consider a symmetric arrangement of two phototubes, one at each end of a relatively long opunter (Fig. 6). The light collection efficiencies for the phototubes 1 and 2

are of the form :

$$\eta_1(x) = A - Bx \qquad \eta_2(x) = A - B(L-x)$$

with A, B and L constants. The total light yield at the phototubes for an energy density distribution $\varepsilon(x)$ is :

$$V_{1,2} = \int \eta_{1,2}(x)\, \varepsilon(x)\, dx$$

The average light yield is related to the total energy deposition, corrected for collection efficiency:

$$V = (V_1 + V_2)/2 = (A - BL/2) \int \varepsilon(x)\, dx$$

The normalized ratio, $R = (V_1 - V_2)/(V_1 + V_2)$, is indipendent of the total energy deposition and it varies linearly with the position of the center of gravity of the energy deposition:

$$R = \frac{V_1 - V_2}{V_1 + V_2} = \frac{B}{2A - LB}\,(L - 2\langle x \rangle)$$

$$\langle x \rangle = \frac{\int \varepsilon(x)\, x\, dx}{\int \varepsilon(x)\, dx}$$

For a calibrated counter the main contribution to the uncertainty in the value of R is due to fluctuations in the number of photoelectrons n_1 and n_2 of phototubes 1 and 2. Assuming Poisson statistics, the error in the quantity R is :

$$\delta R = 1/\sqrt{n_1 + n_2}$$

A typical counter has L = 3 meters , BL = 2/3 A and $n_1 + n_2 =$ 5/MeV . For a total energy deposition of 2 GeV one gets :

$$\delta \langle x \rangle = L \cdot \delta R = L/\sqrt{n_1 + n_2} \cong 3 \text{ cm} !$$

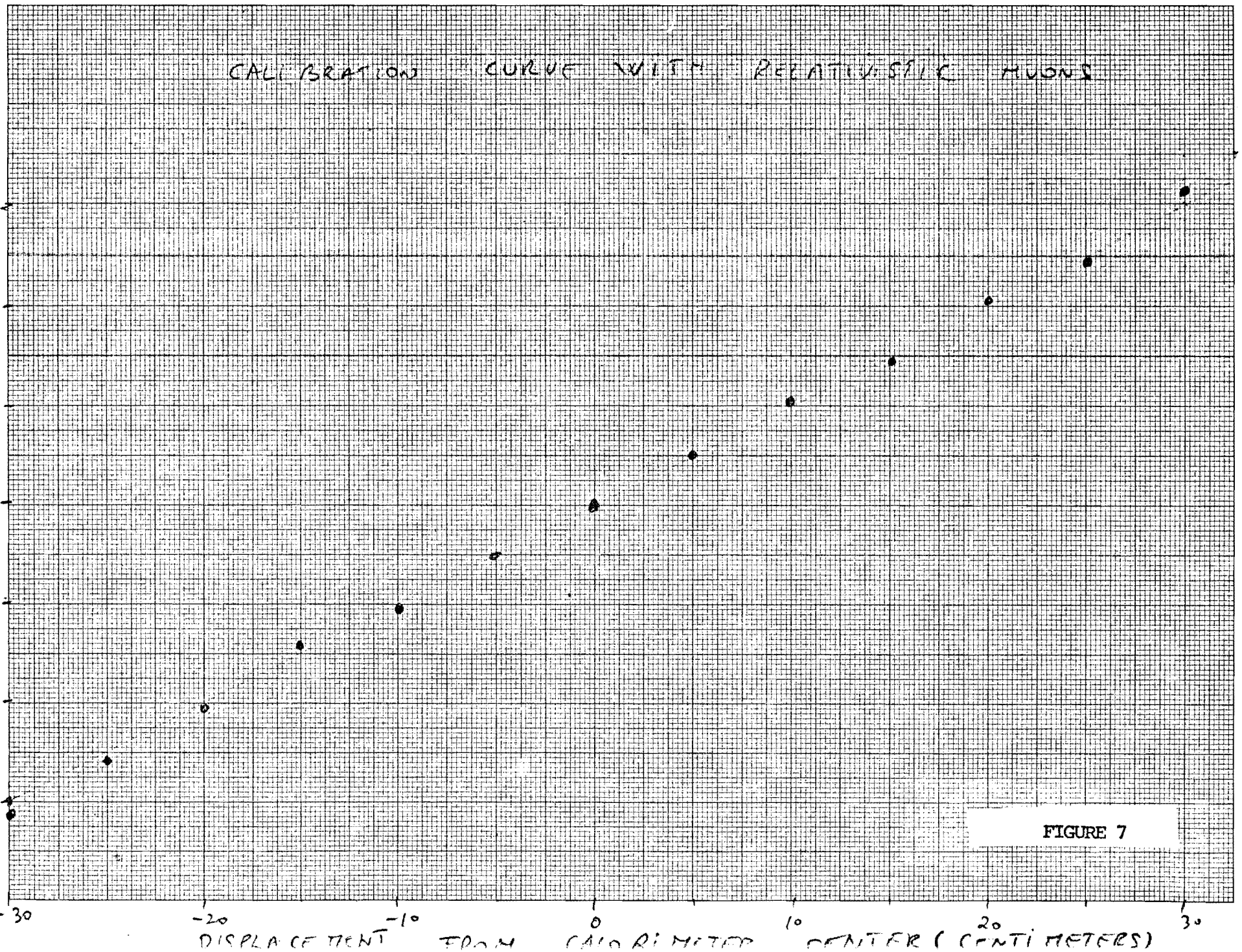

FIGURE 7

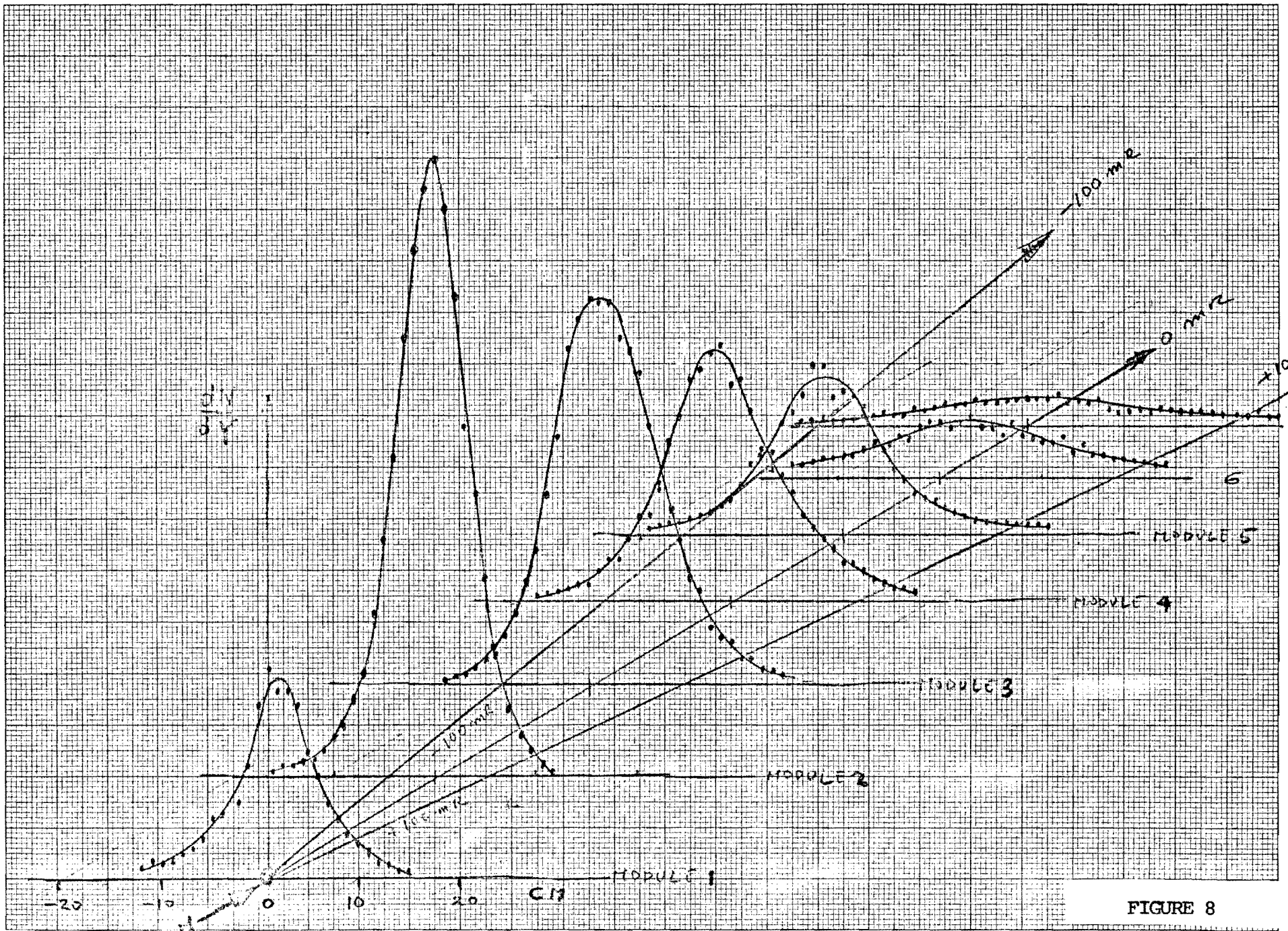

FIGURE 8

The method has been applied to a fine grain calorimeter in a 17 GeV positive hadron beam. The calorimeter is made of 5 mm steel plates 80 x 84 cm^2, separated by 5mm scintillator gaps . Each module of 24 plates is viewed by a pair of 5" phototubes, one at each side. Seven of such modules, stacked close to each other, constitue the calorimeter. Pulse heights from the 14 phototubes are measured by separate charge digitizers and they are recorded onto tape by a HP 2100 computer . The incident hadron beam is defined by a 7 x 7 cm^2 counter telescope. The gain of each of the 14 tubes has been calibrated frequently with positive muons which are easily identified by an additional scintillator counter behind the concrete beam stopper. The light collection efficiency as a function of the impact point has been measured for each tube with the same muon line over the interval $\pm$ 30 cm , sufficiently large to insure a full containment of the hadronic cascade produced by particles incident at the center of the counter . Over this interval , the ratio $R = (V_1 - V_2)/(V_1 + V_2)$ varies linearly with the position of the incident muons. (Fig. 7). The width of the R distribution is entirely consistent with the statistical fluctuations in the number of photoelectrons.

Figure 8 shows the distribution in the variable R for each one of the seven modules of the calorimeter. We have assigned to each entry a weight proportional to the energy deposited in the module, i.e. proportional to V. This is necessary, since in order to construct the center of gravity from several of these points we must combine the quantities

$$V \cdot R = \int \varepsilon(x)\, x\, dx$$

rather than the normalized values R . We remark that this procedure is dictated also by the requirement that the sum of the contributions of the individual particles of a jet adds up to the resultants for the total

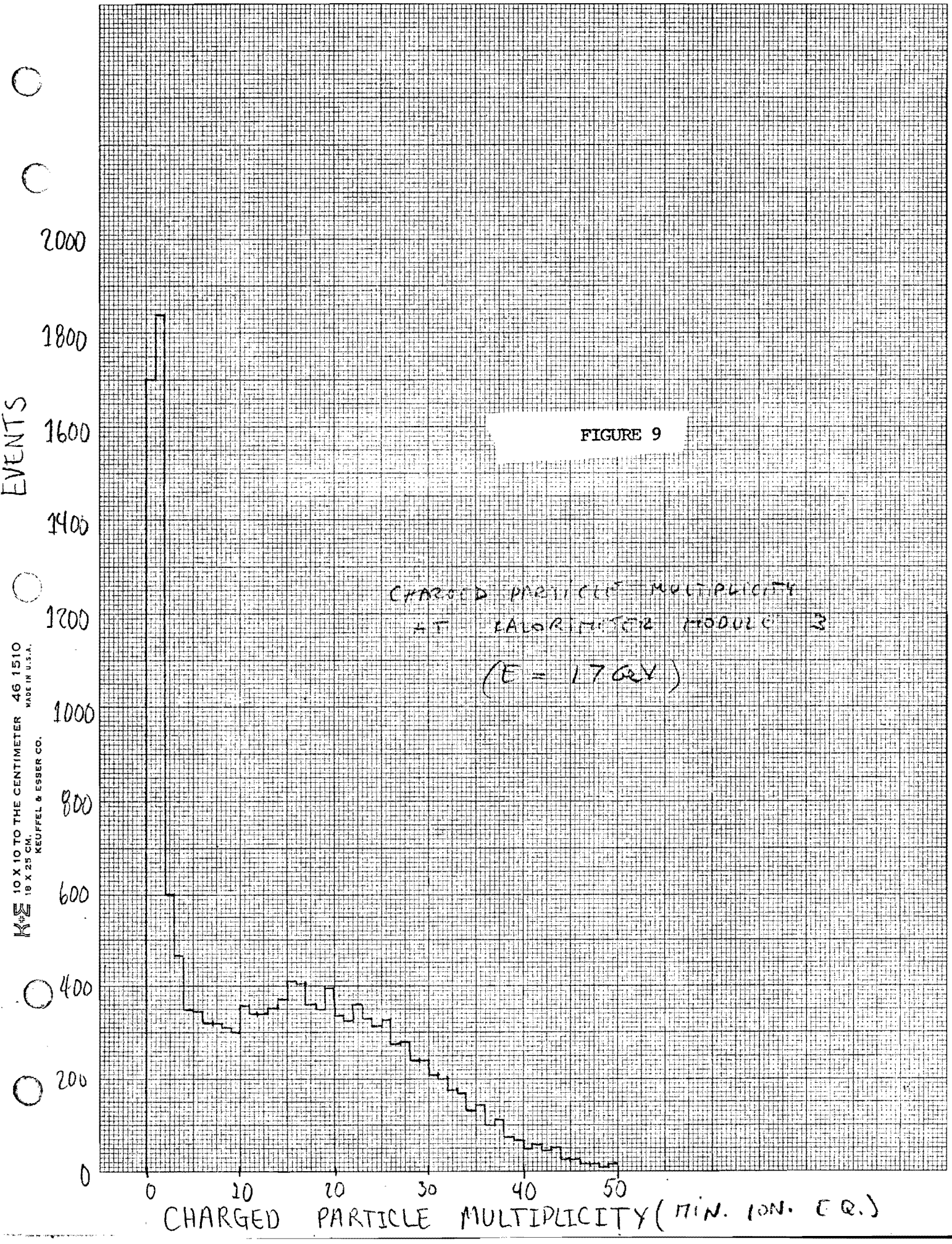
EVENTS
2000
1800
1600
1400
1200
1000
800
600
400
200
0
0
10
20
30
40
50
CHARGED PARTICLE MULTIPLICITY (MIN. ION. EQ.)
CHARGED PARTICLE MULTIPLICITY
+T CALORIMETER MODULE 3
(E = 17 GeV)
10 X 10 TO THE CENTIMETER 46 1510
18 X 25 CM.
KEUFFEL & ESSER CO.
MADE IN U.S.A.

FIGURE 9

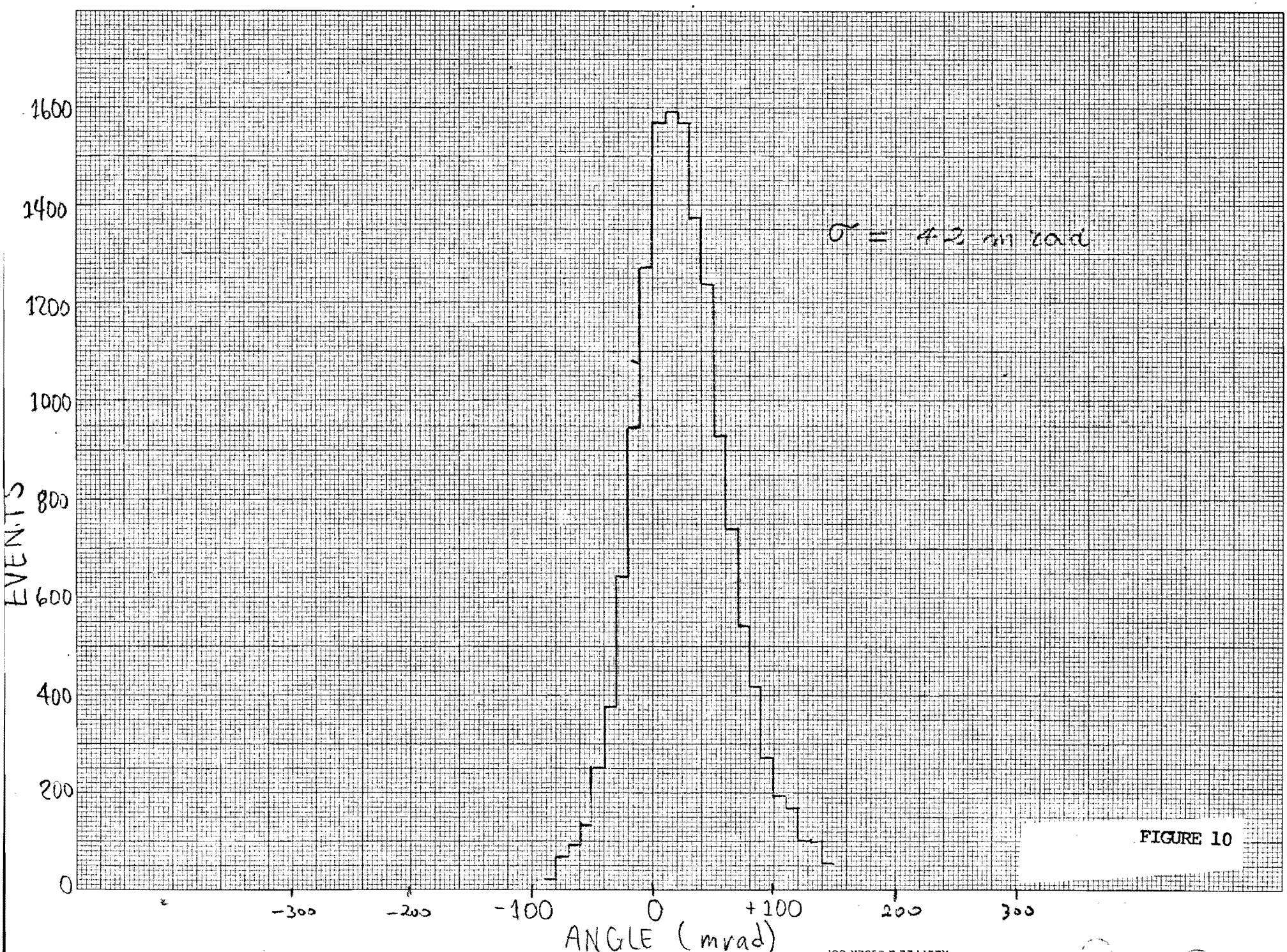

FIGURE 10

momentum of the jet. The procedure is essential because the energy depositions in individual modules are subject to large fluctuations from event to event. (Fig. 9)

We have fitted a straight line through the centers of gravity of individual events. Each point has received a weight proportional to the energy deposition in the module. It is interesting to compare the results of the fit with the a-priori known spatial coordinates of the incident beam. The residual angular spread has a r.m.s. deviation of approximately 40 mrad. (Fig. 10). The position of the incident hadron at the face of the calorimeter can be determined to an accuracy of about 8 cm .

Finally we have used the Montecarlo calculation on the development of the nuclear and electromagnetic cascades in order to extrapolate the experimental results of the test module to the final detector. and to the low-Z,high-Z structure .The conclusions are :

i) the Montecarlo calculation reproduces well the results of the test module, once the resolution in the localization of the center of gravity is taken into account.

ii)we reconstruct with the low-Z modules of the final set-up the direction of the total shower momentum with an r.m.s. deviation which is approximately equal to the one of the test module .

iii)The high-Z modules give an appréciably better angular resolution (i. e. 22 mrad r.m.s. for E ≈ 17 GeV) The π^0 component appears to be more sharply collimated than the total ionization losses .

iv) We have combined the information from the high-Z and the low-Z modules and we have taken into account the resolution of the determination of the center of gravity : the over-all resolution in the shower direction is

approximately 30 mrad r.m.s. for E = 17 GeV . The resolution improves slightly with energy. We find 20 mrad at E= 50 GeV and 15 mrad at E≈ 100 GeV.

REFERENCES

1) - J, Engler et al. N.I.M. 106, 189, (1973)

- Turkot et al . (unpublished, private communications from W. Selove)

- B. Barish et al. (unpublished)

- L. Baum et al. (Munich group at CERN)

2) - J.Ranft and G. Routti, CERN program CASKA

- T.A. Gabriel and K. C. Chandler ORNL -4606 and package code CCC-178/HETC

3) - C. Rubbia , never published.

4) L.Baum, G. Lobkowitz , H. Hilscher and A. Staude ,to be published. We are extremely grateful to these authors for having permitted the use of their data tapes.

5) - Y.B. Bushnin et al. N.I.M. ,106, 493, (1973)

APPENDIX 3

Beams

The neutrino source at NAL is a π-K beam produced at zero degrees with respect to the incident protons and having a 400-meter-long decay path which terminates 1100 meters upstream of the detector building. At the present time three interchangeable focussing arrangements are available for enhancing and/or momentum-analyzing the hadrons as they enter the decay pipe. These together with the option to omit the focussing devices altogether provide four neutrino beams with different properties any of which may be preferred depending upon the objectives of a given experiment. We have calculated the expected event rates in the proposed detector for these beams (see Table I). We discuss below the properties of each beam in the context of the experimental program.

1) Horn beam. This system provides the highest total event rate at nearly all energies, but particularly at the lower end of the spectrum. It is the clear choice for all of the very rare processes, reactions 5-12 of Table I. It also provides the highest-statistics for deep-inelastic scattering where the final state is well-determined by the detector.

2) Quadrupole triplet beam. The yields from this system are similar to those from the horn beam at the highest energies, with much lower fluxes at lower energies. This beam is more suitable for studying reactions in which the neutrino energy cannot be reconstructed from the observed final state, e.g. $\nu_\mu + N \rightarrow \nu_\mu +$ hadrons, or production of new particles at the highest beam energies which decay into neutrinos. In the first example it is desirable to limit the low-energy neutrino flux to insure high muon detection efficiency (by reducing the number of events with large-angle muons). In the second

example the signal would appear as an apparent breakdown of scaling, and could best be established by comparing data taken with different beam spectra.

3) Sign-selected beam. The present dichromatic system operated in the high-yield, low-resolution mode gives a spectrum similar to that of the quad triplet, but produces a nearly pure neutrino or pure antineutrino beam. The pion and kaon neutrinos are resolved as two rather broad peaks in energy, and the total yield is approximately half that of the quad triplet. A priori knowledge of the neutrino "sign" is highly desirable for studying events without muons. The dichromaticity is also useful for checking the calibration of the energy measurement in deep inelastic events.

3a) Dichromatic beam. If a high-resolution dichromatic beam is constructed in the future, it will become possible to study the y-distribution of the muonless events subject to a 2-fold ambiguity due to the two energies of the beam. If in addition the angle of the hadron jet can be measured, the kinematics will be determined completely except for the energy ambiguity. These added constraints will greatly facilitate interpretation of the data.

4) Bare target beam. The virtue of this arrangement is its simplicity. In particular the calculation of neutrino fluxes given reliable hadron production data is very straightforward.

The expected fluxes for these beams are compared in Fig. 1, 2 and 3.

Flux Measurement

The neutrino flux is calculated form the momentum-angle distribution of pion and kaon production in the aluminum target. To imporve the knowledge of these hadron yields we will soon begin a program of measurements using the neutrino target and the upstream portion of the existing N1 (muon) beam. The measurements will be carried out parasitically with neutrino data taking.

When the quadrupole triplet or sign selected neutrino beam is in use, direct measurements of the hadrons accepted by the focussing system are obtained; when the pulsed horns are in use for neutrinos, bare-target production data are accumulated during the long spill while the horns are off. Our objective is to achieve eventually one-percent accuracy for hadron production in the angular region relevant to the neutrino beams.

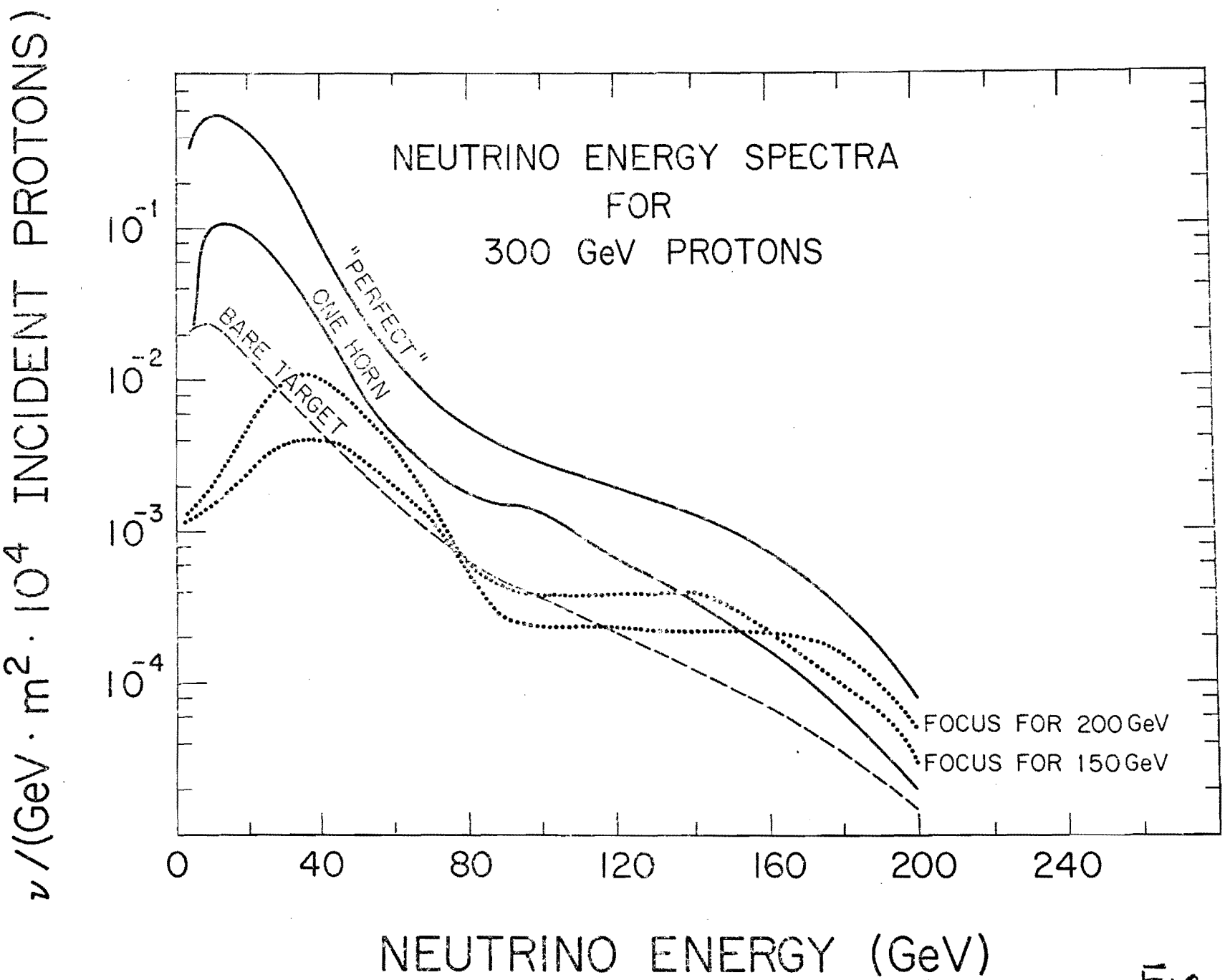
NEUTRINO ENERGY SPECTRA
FOR
300 GeV PROTONS
"PERFECT"
ONE HORN
BARE TARGET
FOCUS FOR 200 GeV
FOCUS FOR 150 GeV
10^{-1}
10^{-2}
10^{-3}
10^{-4}
0
40
80
120
160
200
240
$\nu/(\text{GeV}\cdot m^2\cdot 10^4$ INCIDENT PROTONS)
NEUTRINO ENERGY (GeV)

Fig I

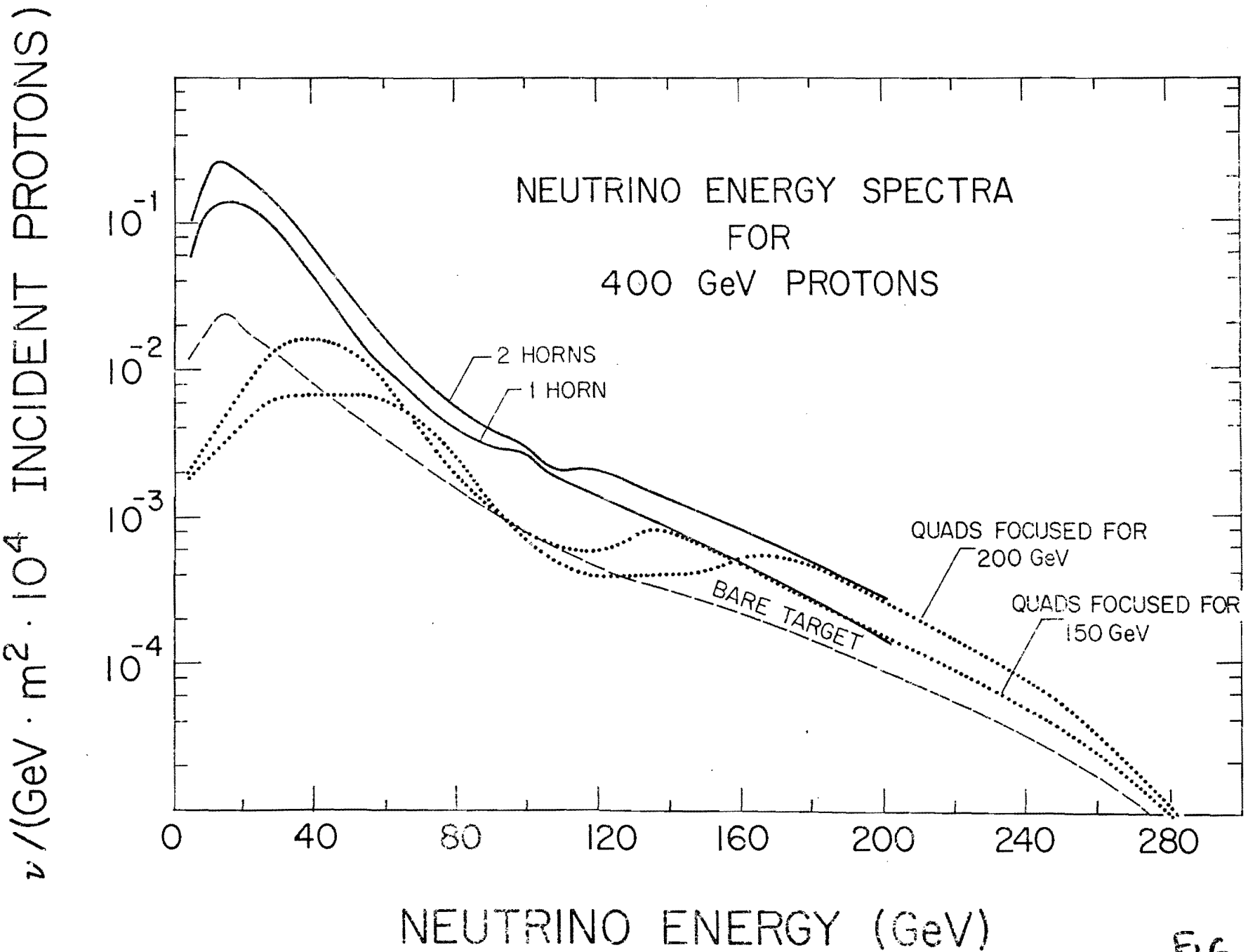
NEUTRINO ENERGY SPECTRA
FOR
400 GeV PROTONS
2 HORNS
1 HORN
QUADS FOCUSED FOR
200 GeV
QUADS FOCUSED FOR
150 GeV
BARE TARGET
ν/(GeV · m^2 · 10^4 INCIDENT PROTONS)
10^{-1}
10^{-2}
10^{-3}
10^{-4}
0
40
80
120
160
200
240
280
NEUTRINO ENERGY (GeV)

FIG 2.

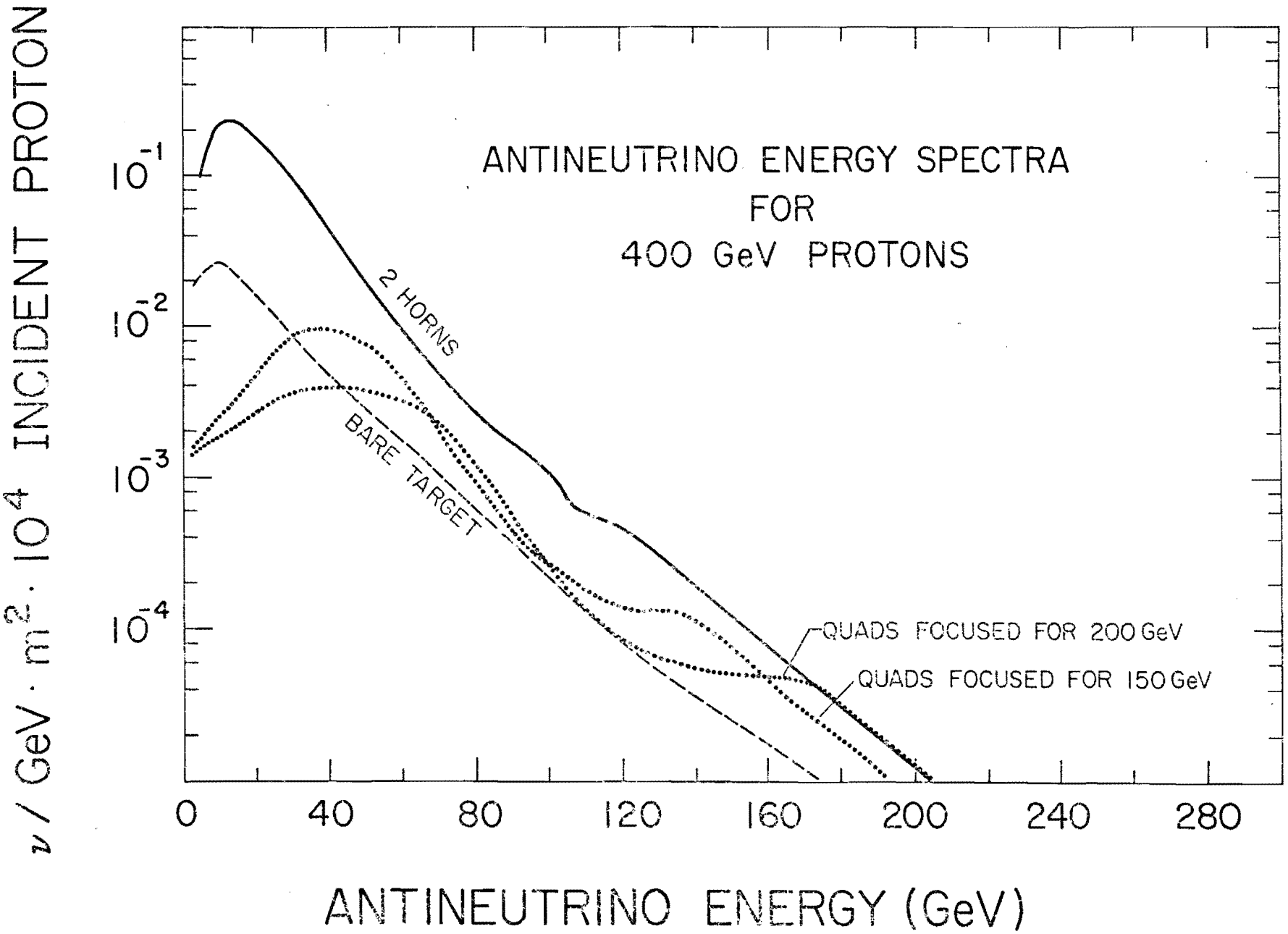
ANTINEUTRINO ENERGY SPECTRA
FOR
400 GeV PROTONS
2 HORNS
BARE TARGET
QUADS FOCUSED FOR 200 GeV
QUADS FOCUSED FOR 150 GeV
ν / GeV · m^2 · 10^4 INCIDENT PROTON
10^{-1}
10^{-2}
10^{-3}
10^{-4}
0
40
80
120
160
200
240
280
ANTINEUTRINO ENERGY (GeV)

FIG 3

Appendix 4

An Enriched Electron Neutrino Beam

In the event that the revised detector proves capable of separating ν_e interactions from ν_μ interactions it will be important to proceed with μ-e universality tests using an enriched beam. In this section we describe a simple initial step in this direction.

The decay of neutral particles (K_1°, Λ°, etc.) gives a relatively enriched yield of electron neutrinos. A simple neutral beam could be constructed in the neutrino area on a one bedplate train; the entire beam would consist of a target and a sweeping magnet (an EPB dipole): Charged particles are sweeped out of the beam, while the neutral particles drift through the decay pipe and decay into ν_μ and ν_e. A calculation of a spectrum from such a beam is given in Fig. 1. Although the flux from this beam is low, it is sufficient to measure the ν_e/ν_μ yield from neutral decay. Furthermore, the ratio of ν_e/ν_μ can be varied in a controlled way with the sweeping magnet to help verify the ν_e identification. We believe that a simple beam of this type would be the first step toward the development of precision ν_e experiments at NAL. It would allow for the development and debugging of ν_e identification techniques with a relatively simple beam while some preliminary ν_e physics could be studied. Also, it would allow a measurement of the ν_e yields before more sophisticated beams are built.

A further source of electron neutrinos is from the decay of muons and the one-bedplate beam can also be used to measure the

ν_e spectrum from this source. These yields are important to understand, since they constitute the background in a ν_μ beam. Furthermore, a source of sign-selected electro-neutrinos comes from the decay of muons in a sign-selected beam.

All of these methods will yield low flux ν_e^* beams, but have the virtue of not causing any large changes in the present structure of the neutrino area. Ultimately, high flux ν_e experiments will be in demand, however, and special beams will be required for that purpose. The most promising possibility is the development of short-high intensity K_1^o, γ^o and $Y^\pm$ beams for the 15' bubble chamber area. The ν_e flux one such beam configuration is shown in Fig. 2. It is our hope to be actively involved in the design of these beams and the experiments that will be done in them.

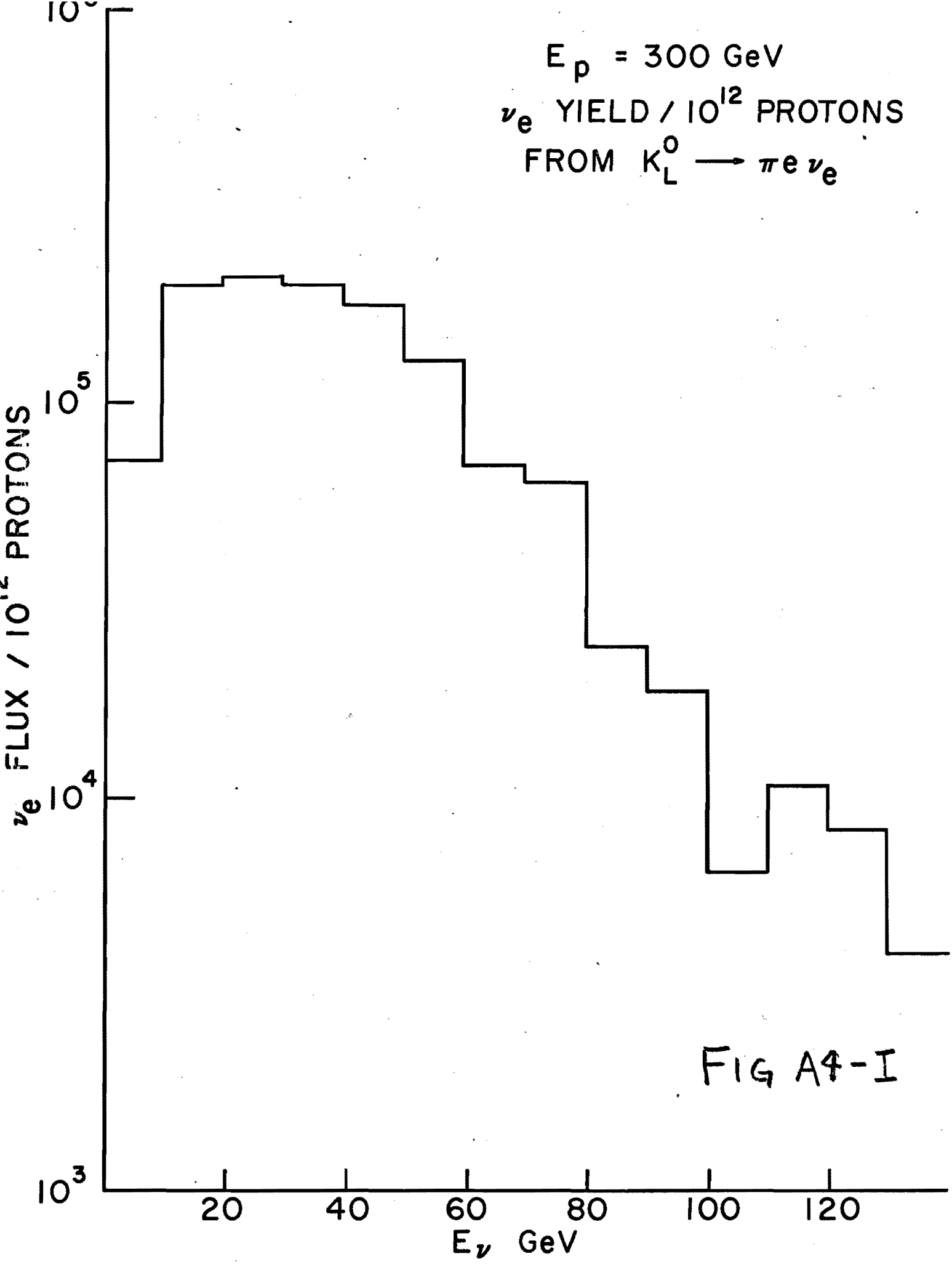
E_p = 300 GeV
ν_e YIELD / 10^{12} PROTONS
FROM $K_L^0 \longrightarrow \pi e \nu_e$
ν_e FLUX / 10^{12} PROTONS
10^5
10^4
10^3
20
40
60
80
100
120
E_ν GeV

FIG A4-I

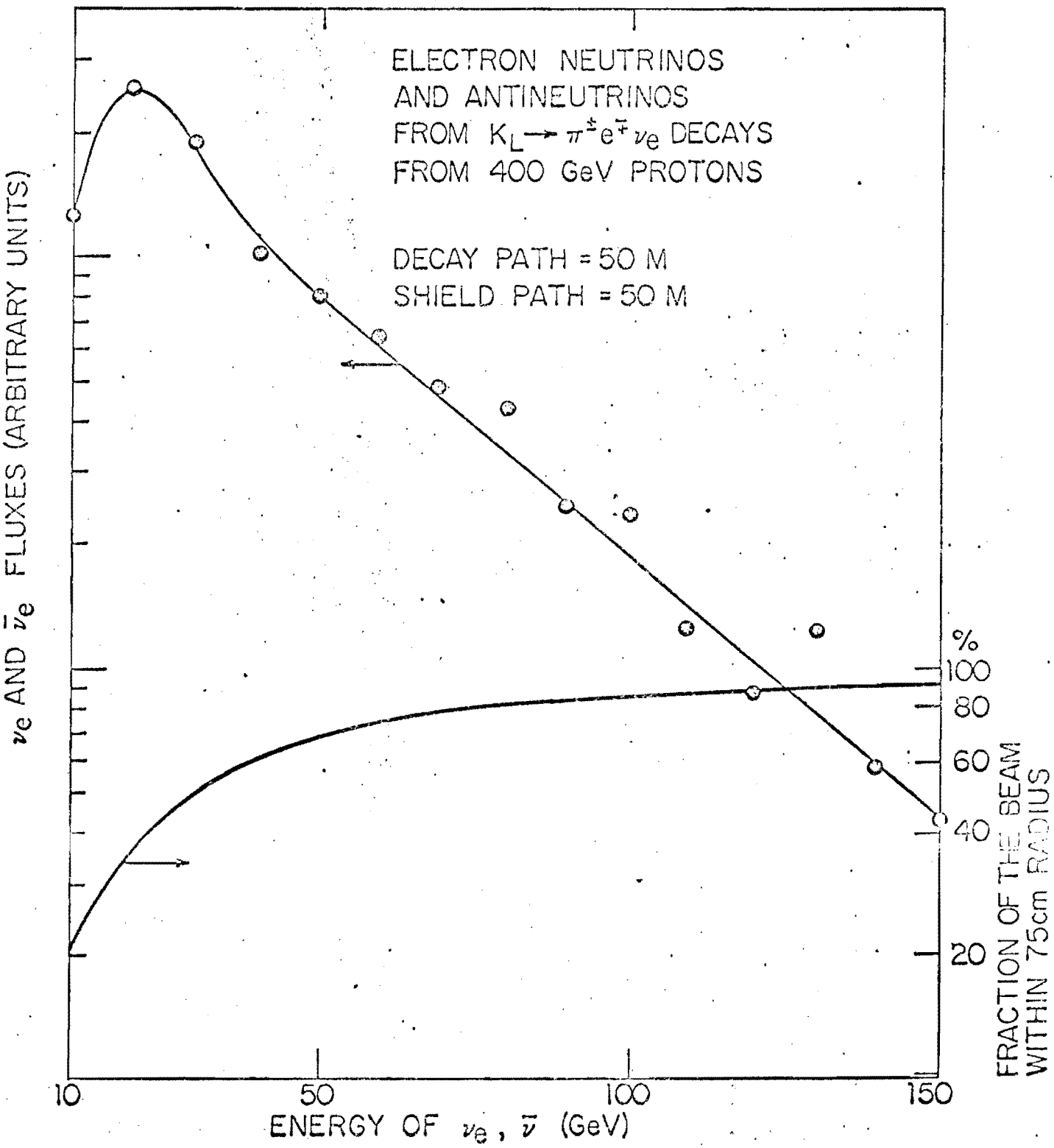
ELECTRON NEUTRINOS
AND ANTINEUTRINOS
FROM $K_L \rightarrow \pi^{\pm} e^{\mp} \nu_e$ DECAYS
FROM 400 GeV PROTONS
DECAY PATH = 50 M
SHIELD PATH = 50 M
ν_e AND $\bar{\nu}_e$ FLUXES (ARBITRARY UNITS)
%
100
80
60
40
20
FRACTION OF THE BEAM
WITHIN 75cm RADIUS
10
50
100
150
ENERGY OF ν_e, $\bar{\nu}$ (GeV)

FIG A4-2